Title
Tests of WIMP Dark Matter Candidates with Direct Dark Matter Detection Experiments

Author
Georgescu, Andreea

Publication Date
2015

Peer reviewed|Thesis/dissertation

UNIVERSITY OF CALIFORNIA

Los Angeles

Tests of WIMP Dark Matter Candidates with Direct Dark Matter Detection Experiments

A dissertation submitted in partial satisfaction

of the requirements for the degree

Doctor of Philosophy in Physics

by

Andreea Irina Georgescu

2015

Abstract of the Dissertation

Tests of WIMP Dark Matter Candidates with Direct Dark Matter Detection Experiments

by

Andreea Irina Georgescu

Doctor of Philosophy in Physics

University of California, Los Angeles, 2015

Professor Graciela B. Gelmini, Chair

We reexamine the current direct dark matter (DM) detection data for several types of DM candidates, both assuming the Standard Halo Model (SHM) and in a halo-independent manner. We consider the potential signals for light WIMPs that have appeared in three direct detection searches: DAMA, CDMS-II-Si, and CoGeNT, and we analyze their compatibility with the null results of other direct detection experiments.

We first consider light WIMPs with exothermic scattering with nuclei (exoDM). Exothermic interactions favor light targets, thus reducing the importance of upper limits derived from Xe targets, the most restrictive of which is at present the LUX limit. In our SHM analysis the CDMS-II-Si and CoGeNT regions become allowed by these bounds, however the SuperCDMS limit rejects both regions for exoDM with isospin-conserving couplings. An isospin-violating coupling of the exoDM, in particular one with a neutron to proton coupling ratio of -0.8 (which we call "Ge-phobic"), maximally reduces the DM coupling to Ge and allows the CDMS-II-Si region to become compatible with all upper bounds. This is also clearly shown in our halo-independent analysis.

Next, we extend and correct a recently proposed maximum-likelihood halo-independent method to analyze unbinned direct DM detection data. Instead of the recoil energy as an independent variable, we use the minimum speed a DM particle must have to impart a given recoil energy to a nucleus. This has the advantage of allowing us to apply the

method to any type of target composition and interaction, e.g. with general momentum and velocity dependence, and with elastic or inelastic scattering. We prove the method and provide a rigorous statistical interpretation of the results. As first applications, we find that for dark matter particles with elastic spin-independent interactions and neutron to proton coupling ratio $f_n/f_p = -0.7$ ("Xe-phobic", which reduces maximally the coupling to Xe), the WIMP interpretation of the signal observed by CDMS-II-Si is compatible with the constraints imposed by all other experiments with null results. We also find a similar compatibility for exothermic inelastic spin-independent interactions with $f_n/f_p = -0.8$.

Finally, we reexamine the interpretation of the annual modulation signal observed by the DAMA experiment as due to WIMPs with a spin-dependent coupling mostly to protons. We consider both axial-vector and pseudo-scalar couplings, and elastic as well as endothermic and exothermic inelastic scattering. We conclude that the DAMA signal is in strong tension with null results of other direct detection experiments, particularly PICASSO and KIMS.

The dissertation of Andreea Irina Georgescu is approved.

Alexander Kusenko

Terrence Tao

Graciela B. Gelmini, Committee Chair

University of California, Los Angeles

2015

To my family and friends

Table of Contents

List of Figures

Acknowledgements

First, I would like to thank my advisor, Graciela Gelmini. Needless to say, this dissertation would not exist if it were not for her invaluable advice, guidance, support and collaboration. I would also like to thank Alexander Kusenko, Roberto Peccei and Terrence Tao for being part of my dissertation committee, and for their time and interest required to review my work.

Second, I would also like to thank all my collaborators. I would like to thank Ji-Haeng Huh for many useful discussions and for his collaboration on all of my papers during the Ph.D. program. I am also grateful to have worked with Eugenio del Nobile for my second publication, "Reevaluation of spin-dependent WIMP-proton interactions as an explanation of the DAMA data", JCAP 1508, no. 08, 046 (2015), which comprises the research in Chapter 4. I would finally also like to thank Paolo Gondolo, for being my collaborator for my third paper "Extended Maximum Likelihood Halo-independent Analysis of Dark Matter Direct Detection Data", JCAP 1511, no. 11, 038 (2015), which contains research presented in Chapter 3.

The last four years of my life would not have been the same if I had not had the support of my wonderful family and friends. I would like to thank my parents, Aristida and Vasile Georgescu, and my grandmother, Aurelia Colan, for their love and support in all areas of my life. Finally, I would like to thank Alexey, Daria, Ekaterina, Garrett, Hector, Josh, Louis, Natalie and my other friends for making my time in graduate school very memorable.

The work in this dissertation was supported in part by the Department of Energy under Award Number DE-SC0009937. I was also supported by the Physics Division Fellowship during the Ph.D. program.

Vita

Education

University of California, Los Angeles – Ph.D. candidate, Physics 2011 – 2015

- *GPA: 3.97*

University of Cambridge, UK – MASt, Physics (Master of Advanced Studies)
(Part III, Department of Physics) 2010 – 2011

- *Master's research thesis:* "Creation of Particles in Electrostatic Backgrounds"
- *First Class Honors*

Jacobs University Bremen, Germany – B.Sc., Physics 2007 – 2010

- *B.Sc. research thesis:* "Equation of state for semilocal strings"
- *GPA: 4.00*

Journal Publications

1. G. B. Gelmini, A. Georgescu, P. Gondolo and J. H. Huh, *Extended Maximum Likelihood Halo-independent Analysis of Dark Matter Direct Detection Data,* JCAP **1511**, no. 11, 038 (2015) [arXiv:1507.03902 [hep-ph]]

2. E. Del Nobile, G. B. Gelmini, A. Georgescu and J. H. Huh, *Reevaluation of spin-dependent WIMP-proton interactions as an explanation of the DAMA data,* JCAP **1508**, no. 08, 046 (2015) [arXiv:1502.07682 [hep-ph]].

3. G. B. Gelmini, A. Georgescu J. H. Huh, *Direct detection of light "Ge-phobic" exothermic dark matter,* JCAP **1407**, 028 (2014) [arXiv:1404.7484 [hep-ph]].

4. A. Georgescu *et. al.*, *Locally Disrupted Synchronization in Langevin Molecular Dynamics*, Phys. Rev. E 86, 026703 (2012)

Research Projects

Los Alamos National Laboratory, NM – Research Assistant June – Sept 2010

Institute for Pure and Applied Mathematics at UCLA – Intern June – Aug 2009

Max Planck Institute for Informatics, Saarbrucken, Germany – Intern Jan 2009

Open Source Projects

1. A. Georgescu, *CoddsDM: Comparing data from direct searches for Dark Matter*, Python implementation of the data analysis for direct detection experiments, https://github.com/Andreea-G/Codds_DarkMatter

2. A. Georgescu, *TeX2HTML-Converter*, software that converts entire TeX and LyX documents directly into interactive HTML pages, with added and improved features (including videos, toggles, alerts etc), https://github.com/Andreea-G/TeX2HTML-Converter

3. S. Mur, A. Georgescu, *LaTeX Bibitem Styler*, software to automatically sort bibitems by citation order of alphabetically, https://github.com/LaTeX-Bibitem-Styler/latex-bibitemstyler

Awards

UCLA

- Physics Division Fellowship 2011 – 2015

University of Cambridge

- Cavendish Laboratory MASt Prize July 2011
- Hugh Humphrey Prize, Fitzwilliam College July 2011
- 1912 Senior Scholarship, Fitzwilliam College July 2011

Teaching

UCLA - Teaching Assistant, Physics 2011 – 2015

Jacobs University Bremen - Teaching Assistant, Electrical Engineering 2008 – 2010

CHAPTER 1

Introduction

Astrophysical and cosmological observations indicate that dark matter (DM) is the most abundant form of matter in the universe, and accounts for about 25% of the energy content of the Universe. Ordinary matter, which makes up stars, planets and ourselves, constitutes only about 5%, while the remaining 70% of the total energy density consists of dark energy. Determining the nature of DM is one of the most fundamental open questions in physics and cosmology. Many different particle candidates have been proposed as possible explanations for the DM. Weakly interacting massive particles (WIMPs) are the most extensively studied DM particle candidates, not only because of their theoretical appeal but also because they could be detected in the near future. WIMPs are non-baryonic particles, with weak strength interactions with visible matter, with masses typically of a few GeV to tens of TeV. They are actively searched for in direct and indirect DM detection experiments, and at colliders. At the Large Hadron Collider (LHC), WIMPs are searched for as missing transverse energy. LHC is searching for indications of physics beyond the Standard Model (SM), which is expected to appear at the electroweak scale. Indirect searches look for WIMP annihilation or decay products (such as high-energy neutrinos produced by WIMPs captured inside the center of the Sun or the Earth), or photons and anomalous cosmic rays from the galactic halo or the galactic center (such as protons or antiprotons), which do not come from astrophysical sources. Direct detection searches (which will be the focus of this dissertation) look for energy deposited within a detector by the collisions between nuclei in a target material and WIMPs belonging to the dark halo of our galaxy.

Most direct searches have produced only upper bounds on scattering rates and their annual modulation [1–11]. The most stringent limits on the DM mass and cross section parameter space are currently set by LUX [10] and SuperCDMS [11] for WIMPs with spin-independent interactions and spin-dependent interactions with neutrons, and by PICASSO [6], SIMPLE [5], COUPP [7], and KIMS [12] for those with protons. While none of these experiments have detected a DM signal so far, several potential signals for "light WIMPs", i.e. WIMPs with mass around a few to tens of GeV, have appeared in three direct detection searches: DAMA [13–16] (here DAMA stands for both DAMA and DAMA/LIBRA), CoGeNT [17–21], and CDMS-II-Si [22], either as an unexplained excess of events (in CoGeNT, and CDMS-II-Si) or as an annual modulation of the rate as expected for a DM signal due to the revolution of Earth around the Sun (DAMA and CoGeNT). CRESST-II [23] has not confirmed a previous DM hint found by the same collaboration [24]. Among the potential DM signals, DAMA's observation of an annually modulated rate has the highest statistical significance. However, these potential signals are challenged by the null results of other direct detection experiments which exclude the possibility of WIMP scattering in a large number of particle models. In particular, the scattering cross section fitting the DAMA data for WIMPs with isospin-conserving spin-independent interactions is several orders of magnitude above the 90% CL LUX limit [25].

In certain particle models [26–32], a DM particle may collide inelastically with a target nucleus producing a different particle state, either heavier (endothermic scattering) or lighter (exothermic scattering, see e.g. [33, 34]), when colliding with a nucleus. Endothermic scattering favors heavier targets, thus enhancing scattering off I in DAMA while reducing scattering off lighter targets such as Ge. Inelastic exothermic scattering [33, 35] instead favors lighter targets, so it favors Na in DAMA over heavier nuclei (Ge and Xe). As pointed out recently in previous direct DM detection data analysis [36–39], of particular interest for the compatibility of the potential CDMS-II-Si and CoGeNT signals with all present limits is the possibility of having DM with inelastic exothermic collisions with nuclei, originally called "exciting DM" [40] in the context of indirect DM detection and later "exothermic DM" (exoDM) [33, 35] in the context of direct dark matter detection. Having a complicated "dark sector" [33, 35, 41, 42] with neutral particles of slightly different masses leads naturally to the idea of having two different states constituting the DM at present, the lightest being stable and the heaviest metastable. It can then happen that the heaviest may down-scatter off nuclei, but the scattering of each state to itself is suppressed or impossible because of the DM couplings to the mediator of the interaction, and the up-scattering of the lightest state is kinematically forbidden (as we will see below, the required speeds for the models we consider would be above 1000 km/s and these high WIMP speeds are not available in the halo of our galaxy). This type of DM favors lighter targets (such as Si in CDMS-II-Si) with respect to heavier ones, thus it suppresses the limits derived from experiments using Xe, which provide otherwise some of the most restrictive limits at present.

The conventional analysis of direct search data relies on a specific model of the DM halo of our galaxy, often chosen to be the standard halo model (SHM). However, there are large uncertainties in our knowledge of the local characteristics of the dark halo of our galaxy, and the compatibility between signal regions and upper bounds from different detectors depends heavily on the local DM velocity distribution. In order to compare data from all the experiments while circumventing these uncertainties, a halo-independent data comparison method was proposed and later used in different forms in [43–52]. The method was generalized in [50] to be applied to WIMP-nucleus scattering cross sections with any type of speed dependency [52]. The basic idea behind this method is that all the dependence of the scattering rate on the halo model, in any detector, resides in the same function which we call $\tilde{\eta}(v_{\min}, t)$ of the speed $v_{\min}$ and the time t. $v_{\min}$ is the minimum speed necessary for the incoming interacting DM particle to impart a recoil energy E_R to a nucleus in each detector. Conversely, given an incoming WIMP speed $v = v_{\min}$, E_R is the extremum recoil energy (maximum energy for elastic collisions, or either maximum or minimum for inelastic collisions) that the DM particle can impart to a nucleus. This method consists in mapping the rate measurements and bounds onto $v_{\min}$ space, which allows to factor out a common function $\tilde{\eta}(v_{\min}, t)$ containing the dependency of the rate on the DM velocity distribution, and use this as a detector-independent variable. Since $\tilde{\eta}(v_{\min}, t)$ is common to all direct search experiments, this function can be measured by all experiments, and the compatibility of the different measurements can be studied. Notice that E_R and $v_{\min}$ are exchangeable variables only for a single nuclide. When a target consists of multiple nuclides, a choice must be made between the two, E_R and $v_{\min}$. Taking E_R as independent variable (as is done in [36, 43, 44]), $v_{\min}$ depends on each target nuclide. In our approach, $v_{\min}$ and the observed energy E' are the independent variables. This allows us to incorporate any isotopic composition of the target by summing over target nuclide – dependent $E_R(v_{\min})$ for fixed observed E'.

In this dissertation, we explore the compatibility between the potential signals of CDMS-II-Si and DAMA with the null results from the other direct DM detection experiments, for different types of DM candidates. We analyze the data both assuming the SHM and in a halo model – independent manner, and present new or extended halo-independent data analysis methods. The data analysis described in this dissertation was implemented in the CoddsDM software [53], an open-source Python program for comparing the data from various direct detection experiments.

In Chapter 1, we review the direct detection rate and the formulation of the generalized halo-independent analysis, which forms the basis for all subsequent chapters.

In Chapter 2 [34], we present comparisons of direct DM detection data for light WIMPs with exothermic scattering with nuclei (exoDM), both assuming the SHM and in a halo-independent manner. We find that the CDMS-II-Si region escapes all upper bounds, the most relevant being LUX and SuperCDMS, for exothermic scattering and spin-independent isospin-violating interactions. Exothermic scattering weakens the Xe-based limits, the strongest of which is the LUX limit. An isospin-violating coupling, in particular a neutron to proton coupling ratio of -0.8 (Ge-phobic), weakens the Ge-based limit from SuperCDMS.

In Chapter 3 [54], we expand and correct a recently proposed [55] extended maximum-likelihood halo-independent (EHI) method to analyze unbinned direct DM detection data. Due to the exponential prefactor in the extended likelihood, it is possible to show that the likelihood is maximized by a non-increasing piecewise constant $\tilde{\eta}$ function, with the number of discontinuities at most equal to the number of observed events. We give a rigorous proof of the method, using the formulation for the generalized halo-independent method presented in Sec.1.3. Instead of the recoil energy E_R as independent variable (as done in [55]), we use the minimum speed $v_{\min}$, which has the advantage of allowing us to extend the method to any type of target composition and interaction, e.g. with general momentum and velocity dependence, and with elastic or inelastic scattering. Furthermore, we provide a rigorous statistical interpretation of the results by defining a two-sided pointwise confidence band, as a collection of confidence intervals in $\tilde{\eta}$ for every value of $v_{\min}$. The pointwise confidence band can be computed for given confidence levels, and thus we can quantitatively assess the compatibility of the unbinned data with upper bounds from other experiments. We apply the method to the three candidate events of CDMS-II-Si, and we find that the observed signal is compatible with the upper limits for elastic spin-independent scattering with isospin-violating interactions for a neutron to proton coupling ratio $f_n/f_p = -0.7$ (Xe-phobic, which maximally reduces the Xe-based LUX limit). Similarly, we also find compatibility for exothermic inelastic spin-independent interactions with $f_n/f_p = -0.8$ (Ge-phobic).

In Chapter 4 [56], we consider WIMPs with a spin-dependent (SD) coupling mostly to protons, as a potential interpretation of the annual modulation signal observed by DAMA. These have the advantage that they weaken the bounds from experiments using target elements whose spin is mostly due to neutrons, such as LUX and SuperCDMS. We study both axial-vector (AV) and pseudo-scalar (PS) interactions. The latter was proposed in [57], who employed a Bayesian analysis and claimed that the DAMA regions can be reconciled at the 99% credible level with the null results of other experiments. We consider both elastic as well as endothermic and exothermic inelastic scattering, and both contact and long-range interactions. We find that the DAMA signal is rejected for elastic and exothermic interactions by a combination of SIMPLE, PICASSO and KIMS limits, and it remains in strong tension with the KIMS bound for endothermic scattering. We analyze the data both assuming the SHM and in a halo-independent manner, and in both cases our conclusions are consistent. For our halo-independent analysis, we present an extended analysis method of the DAMA data when both target elements, Na and I, are involved in the scattering.

1.1 Direct detection rate

The differential recoil rate per unit detector mass, typically given in units of counts/day/kg/keV, for the scattering of WIMPs of mass m off a target nuclide T with mass m_T is

$$\frac{\mathrm{d}R_T}{\mathrm{d}E_R} = \frac{\rho}{m}\frac{C_T}{m_T}\int_{v\geq v_{\min}(E_R)} \mathrm{d}^3v\ f(\boldsymbol{v},t)v\frac{\mathrm{d}\sigma_T}{\mathrm{d}E_R}(E_R,\boldsymbol{v}), \tag{1.1.1}$$

where C_T is the mass fraction of nuclide T in the detector, E_R is the nuclear recoil energy, ρ is the WIMP local energy density, $f(\boldsymbol{v},t)$ is the WIMP velocity distribution in Earth's frame, $\mathrm{d}\sigma_T/\mathrm{d}E_R$ is the WIMP-nucleus differential scattering cross section, and $v_{\min}(E_R)$ is the minimum WIMP speed needed to impart to the target nucleus a recoil energy E_R, as we will present in the next section. The revolution of Earth around the Sun introduces an annual modulation of $f(\boldsymbol{v}, t)$. In detectors with more than one nuclide in their target, the total differential recoil rate is

$$\frac{\mathrm{d}R}{\mathrm{d}E_R} = \sum_T \frac{\mathrm{d}R_T}{\mathrm{d}E_R}. \tag{1.1.2}$$

Most experiments do not measure the recoil energy E_R directly. They measure instead a proxy E' for it, such as the ionization or scintillation signals, subject to experimental uncertainties and fluctuations. These are represented by a target-dependent resolution function of the detector $G_T(E_R, E')$, which is the probability distribution for an event with recoil energy E_R to be measured with energy E', and incorporates the mean value $\langle E' \rangle = Q_T(E_R)E_R$, with Q_T the target's quenching factor, and the detector energy resolution. Including the experimental acceptance $\epsilon(E_R, E')$ from various experimental cuts and efficiencies, which, in general, is a function of both the recoil energy E_R and the detected energy E', the differential event rate in the detected energy E' can be written as

$$\frac{\mathrm{d}R}{\mathrm{d}E'} = \sum_T \int_0^\infty \mathrm{d}E_R \; \epsilon(E_R, E') G_T(E_R, E') \frac{\mathrm{d}R_T}{\mathrm{d}E_R}. \tag{1.1.3}$$

With respect to the WIMP-nucleus cross section and values of m and δ, we proceed in a phenomenological manner, without referring to particular DM particle models (although models with the required WIMP masses and mass splittings have been proposed in [39] - see also references therein). We use the usual contact spin-independent (SI) interaction cross section, which applies also to exoDM [33]

$$\frac{\mathrm{d}\sigma_T^{SI}}{\mathrm{d}E_R}(E_R, v) = \sigma_p \frac{\mu_T^2}{\mu_p^2} [Z_T + (A_T - Z_T)(f_n/f_p)]^2 \; \frac{m_T}{2\mu_T^2 v^2} F_T^2(E_R), \tag{1.1.4}$$

where σ_p is the WIMP-proton cross section, f_n and f_p are the effective DM couplings to neutrons and protons, μ_p is the WIMP-proton reduced mass, A_T and Z_T are the atomic and charge numbers of the nuclide T, respectively, and $F_T^2(E_R)$ is a nuclear form factor, for which we take the Helm form factor [58] normalized to $F_T^2(0) = 1$.

With $\mathrm{d}R/\mathrm{d}E'$ given in (1.1.1), the energy-integrated rate over an energy interval $[E_1', E_2']$

is

$$R_{[E'_1,E'_2]}(t) \equiv \int_{E'_1}^{E'_2} \mathrm{d}E' \, \frac{\mathrm{d}R}{\mathrm{d}E'}. \tag{1.1.5}$$

Given a WIMP velocity distribution $f(\boldsymbol{v}, t)$, the rate $R_{[E'_1,E'_2]}$ measured by an experiment in an energy interval $[E'_1, E'_2]$ can be used to infer best-fit regions and upper bounds on the WIMP-proton cross section σ_p in an $m - \sigma_p$ plane.

1.2 Elastic and inelastic scattering

The minimum speed the DM particle must have in the rest frame of the target nuclide in order to impart a nuclear recoil energy E_R to a nucleus of mass m_T for $\mu_T|\delta|/m^2 \ll 1$ is

$$v_{\min} = \frac{1}{\sqrt{2m_T E_R}} \left| \frac{m_T E_R}{\mu_T} + \delta \right|, \tag{1.2.1}$$

where μ_T is the DM-nucleus reduced mass. The mass splitting $\delta = m' - m$ can be either positive for endothermic scattering [26], negative for exothermic scattering [33, 35, 40], or zero for elastic scattering. The same equation relates the speed of a DM particle v with the maximum, and in this case also minimum, recoil energy the particle can impart to a nucleus. Inverting this equation one finds the maximum and minimum recoil energies for a fixed DM particle speed v: $E_R^{T,-}(v) < E_R < E_R^{T,+}(v)$, with

$$E_R^{T,\pm}(v) = \frac{\mu_T^2 v^2}{2m_T} \left(1 \pm \sqrt{1 - \frac{2\delta}{\mu_T v^2}} \right)^2 . \tag{1.2.2}$$

Fig. 1.1 shows these two functions for a Si target (used in CDMS-II-Si) for several WIMP masses m and negative values of δ: -50, -200 and -300 keV. The left panel in Fig. 1.2 shows the two $E_R^{T,\pm}(v)$ branches for the Na component of DAMA, for $\delta = -30$ and -50 keV, for WIMP masses that correspond to the best fit regions we will present in later chapters. The right panel shows the $E_R^{T,\pm}(v)$ branches for the I component of DAMA, for $\delta = 50$ and 100 keV. For a particular recoil energy E_R only the speeds to the right of the $v_{\min}(E_R)$ line are allowed, while for a fixed speed v only the recoil energies in between the two lines $E_R^{T,-}(v)$ and $E_R^{T,+}(v)$ are allowed. The minimum possible value of v for the interaction to be kinematically allowed is $v_\delta^T = \sqrt{2\delta/\mu_T}$ for endothermic scattering, and $v_\delta^T = 0$ for exothermic. This speed

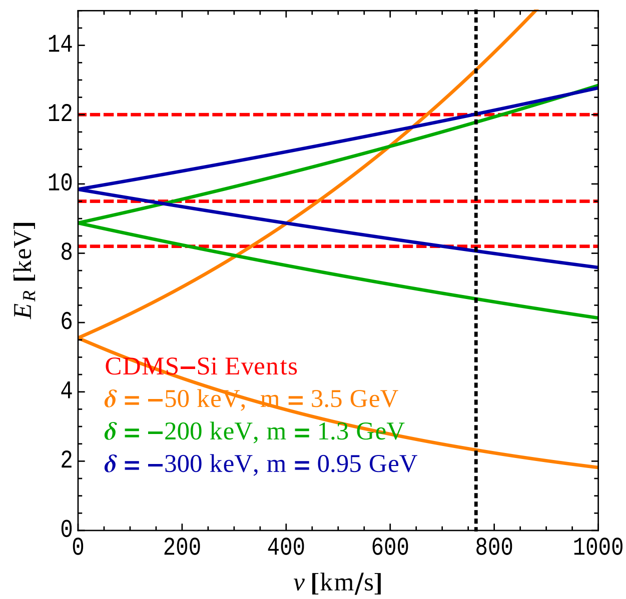

Figure 1.1. Recoil energy range in Si as a function of the WIMP speed v with respect to the Earth for different values of the WIMP mass m and mass splitting δ, compared with the energies of the three events observed by CDMS-II-Si (horizontal lines), assuming that the observed and recoil energies coincide. We see that for negative δ values with $|\delta| > 300$ keV not all three events can be contained within the possible DM recoil energy range in the SHM (the halo model determines the maximum possible value of v, which here is 765 km/s).

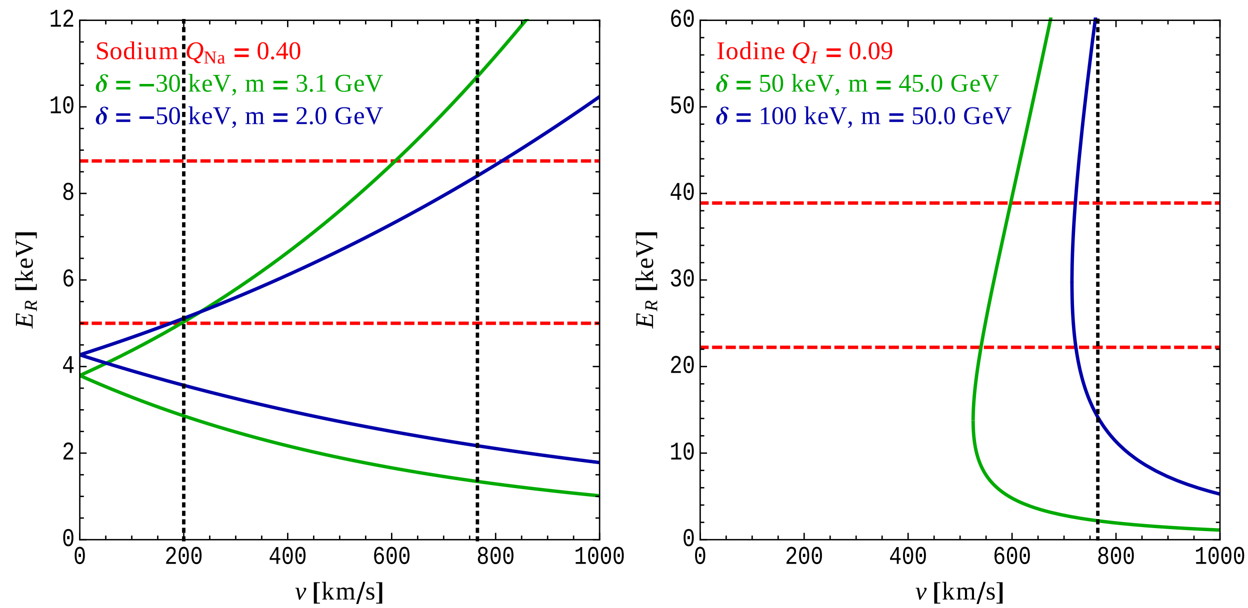

Figure 1.2. Recoil energy range for exothermic scattering off Na (left) and endothermic scattering off I (right), as a function of the WIMP speed v, for the indicated values of WIMP mass m and mass splitting δ. The two red horizontal lines enclose the 2.0–3.5 keVee energy interval, in which most of the DAMA signal is observed. Here $Q_{\mathrm{Na}} = 0.40$ and $Q_{\mathrm{I}} = 0.09$. The DAMA events can only be between the two vertical lines at $v_{\min} = 200$ km/s and $v_{\min} = v_{\max} = 765$ km/s (see the text).

value corresponds to the point of intersection of the two $E_R^{T,\pm}$ branches, which occurs at $E_\delta^T = E_R^{T,+}(v_\delta^T) = E_R^{T,-}(v_\delta^T) = \mu_T|\delta|/m_T$. We define v_δ to be the smallest of the v_δ^T values among all nuclides T in the detector.

Except for our halo-independent analysis, in this dissertation we assume the Standard Halo Model (SHM) for the dark halo of our galaxy, where the DM local density is $\rho = 0.3$ GeV/cm^3 and the velocity distribution of WIMPs in the galactic frame is a truncated Maxwell-Boltzmann distribution

$$f_{\rm G}(\vec{u}) = \frac{1}{N_{\rm esc}(v_0\sqrt{\pi})^3} \exp(-u^2/v_0^2)\,\theta(v_{\rm esc} - u). \tag{1.2.3}$$

Here v_0 is the velocity dispersion and $v_{\rm esc}$ is the escape speed from our galaxy. The normalization factor

$$N_{\rm esc} \equiv {\rm erf}(v_{\rm esc}/v_0) - 2(v_{\rm esc}/v_0)\exp(-v_{\rm esc}^2/v_0^2)/\sqrt{\pi} \tag{1.2.4}$$

ensures that $\int d^3u\, f_{\rm G}(\vec{u}) = 1$. We consider v_0 to be the same as the velocity of the Local Standard of Rest $v_0 = 220$ km/s, and we take $v_{\rm esc} = 533$ km/s, according to recent Radial Velocity Experiment (RAVE) 2013 results [59]. The velocity distribution in Earth's frame, $f(\boldsymbol{v}, t)$ in (1.1.1), can be obtained with the Galilean transformation

$$f(\boldsymbol{v}, t) = f_{\rm G}(\boldsymbol{v}_\odot + \boldsymbol{v}_\oplus(t) + \boldsymbol{v}) , \tag{1.2.5}$$

where $\boldsymbol{v}_\odot$ and $\boldsymbol{v}_\oplus(t)$ are the velocity of the Sun with respect to the galaxy and the time dependent velocity of Earth with respect to the Sun, respectively. We take $v_\odot = 232$ km/s, and $v_\oplus = 30$ km/s in an orbit inclined at 60° with respect to the galactic plane [60]. The maximum value of the DM speed allowed for a given halo model is the sum of the escape speed $v_{\rm esc}$ and the modulus of Earth's velocity in the galactic rest frame, which is equal on average to the Sun's velocity $\vec{v}_\odot$; therefore, for our choice of parameter values, $v_{\rm max} = 765$ km/s. This is indicated with a vertical line in Figs. 1.1 and 1.2.

As a result, endothermic scattering with a target nucleus will be kinematically forbidden for δ larger than $\simeq 3.3$ keV(μ_T/GeV). In the ranges for m and δ corresponding to the best fit regions presented in later chapters, endothermic scattering with Si in CDMS-II-Si and Na in DAMA is kinematically forbidden a $|\delta|$ of 50 keV or larger. On the other hand, scattering off I in DAMA is allowed for endothermic scattering, as can be seen in the right panel of Fig. 1.2 for $\delta = 50$ and 100 keV. In an exothermic scattering, the energy of the recoiling nucleus is peaked around E_δ^T, which is proportional to the splitting between the dark matter states and is inversely proportional to the nuclear mass. Consequently, the nuclear recoils caused by exothermic DM are more visible in experiments with light nuclei and low thresholds [33].

In Fig. 1.1 we also compare the allowed recoil energy values in Si with the energies of the three events observed by CDMS-II-Si (horizontal lines). We took the recoil energies to coincide with the observed energies (i.e. perfect energy resolution), which is not a bad approximation for CDMS-II-Si. The values of m and δ are those corresponding to some of the best fit points allowed by all upper limits (and coincide with the values of the halo-independent analysis we show later). We see that for negative δ values such that $|\delta| > 300$ keV not all three events can be contained within the possible recoil energy range for the SHM, i.e. either the largest energy event (or events) or the lowest energy event (or events) must be due to background. However, even for smaller negative δ values, such as $\delta = -200$ keV, we find that, in the SHM, best fit regions are obtained when the highest-energy of the three CDMS-II-Si observed events is considered background.

Earth's revolution around the Sun causes the velocity distribution given in (1.2.5), and therefore the scattering rate in (1.1.1), to modulate in time. Both the time-average rate and the modulation amplitude of the rate can be measured. In the SHM, the velocity of Earth with respect to the Galaxy is maximum at the end of May or the beginning of June. The rate has a maximum at this moment if $v_{\rm min} > 200$ km/s and it has instead a minimum at this moment if $v_{\rm min} < 200$ km/s. Thus, choosing the modulation phase so that the modulation amplitude is positive for $v_{\rm min} > 200$ km/s, the amplitude is negative for $v_{\rm min} < 200$ km/s. Only $v_{\rm min} > 200$ km/s are compatible with the phase of the DAMA modulation data such that the rate has the maximum on the 2nd of June [16]. The value of $v_{\rm min} = 200$ km/s is shown as a vertical line in Fig. 1.2.

1.3 Generalized halo-independent analysis method

In this section we will present a generalized halo-independent method, developed in [50], for which the cross section has any general dependence on the DM velocity and nuclear recoil energy.

By inserting (1.1.1) into (1.1.3) we can express the differential event rate in the detected energy E' as a double integral

$$\frac{\mathrm{d}R}{\mathrm{d}E'} = \frac{\rho}{m} \sum_T \frac{C_T}{m_T} \int_0^\infty \mathrm{d}E_R \, \epsilon(E_R, E') G_T(E_R, E') \times \int_{v \geq v_{\min}(E_R)} \mathrm{d}^3 v \, f(\boldsymbol{v}, t) v \frac{\mathrm{d}\sigma_T}{\mathrm{d}E_R}(E_R, \boldsymbol{v}), \tag{1.3.1}$$

from where changing the integration order and extracting a reference parameter σ_{ref} from the cross section we get

$$\frac{\mathrm{d}R}{\mathrm{d}E'} = \frac{\sigma_{\text{ref}} \rho}{m} \int_{v \geq v_\delta} \mathrm{d}^3 v \, \frac{f(\boldsymbol{v}, t)}{v} \frac{\mathrm{d}\mathcal{H}}{\mathrm{d}E'}(E', \boldsymbol{v}). \tag{1.3.2}$$

Here the function $\mathrm{d}\mathcal{H}/\mathrm{d}E'$ is

$$\frac{\mathrm{d}\mathcal{H}}{\mathrm{d}E'}(E', \boldsymbol{v}) \equiv \sum_T \frac{\mathrm{d}\mathcal{H}_T}{\mathrm{d}E'}(E', \boldsymbol{v}), \tag{1.3.3}$$

where $\mathrm{d}\mathcal{H}_T/\mathrm{d}E'$ is defined as

$$\frac{\mathrm{d}\mathcal{H}_T}{\mathrm{d}E'}(E', \boldsymbol{v}) \equiv \begin{cases} \dfrac{C_T}{m_T} \displaystyle\int_{E_R^{T,-}(v)}^{E_R^{T,+}(v)} \mathrm{d}E_R \, \epsilon(E_R, E') G_T(E_R, E') \frac{v^2}{\sigma_{\text{ref}}} \frac{\mathrm{d}\sigma_T}{\mathrm{d}E_R}(E_R, \boldsymbol{v}) & \text{if } v \geq v_\delta^T, \\ 0 \quad \text{if } v < v_\delta^T. \end{cases} \tag{1.3.4}$$

In (1.3.2) and (1.3.4) we have written explicitly a parameter σ_{ref} extracted from the differential cross section to represent the strength of the interaction. This is preferably, but not necessarily, the WIMP-proton scattering cross section σ_p.

Here we consider only differential cross sections (and thus also $\mathrm{d}\mathcal{H}/\mathrm{d}E'$ functions) which depend only on the speed $v = |\boldsymbol{v}|$, and not on the direction of the initial WIMP velocity $\boldsymbol{v}$. The cross section depends only on v if the incoming WIMPs and the target nuclei are unpolarized and the detector response is isotropic, as is most common. In this case, one can write the differential event rate in a simpler form as

$$\frac{\mathrm{d}R}{\mathrm{d}E'} = \frac{\sigma_{\text{ref}} \rho}{m} \int_{v_\delta}^\infty \mathrm{d}v \, \frac{F(v, t)}{v} \frac{\mathrm{d}\mathcal{H}}{\mathrm{d}E'}(E', v), \tag{1.3.5}$$

where $F(v,t) \equiv v^2 \int \mathrm{d}\Omega_v \; f(\boldsymbol{v},t)$. We now define the function $\tilde{\eta}(v_{\rm min},t)$ as

$$\tilde{\eta}(v_{\rm min},t) \equiv \frac{\rho\sigma_{\rm ref}}{m} \int_{v_{\rm min}}^{\infty} \mathrm{d}v \; \frac{F(v,t)}{v}, \tag{1.3.6}$$

which contains all the dependence of the scattering rate on the halo model. Thus

$$\frac{\sigma_{\rm ref}\rho}{m} \frac{F(v,t)}{v} = -\frac{\partial\tilde{\eta}(v,t)}{\partial v}, \tag{1.3.7}$$

and (1.3.5) becomes

$$\frac{\mathrm{d}R}{\mathrm{d}E'} = -\int_{v_\delta}^{\infty} \mathrm{d}v \; \frac{\partial\tilde{\eta}(v,t)}{\partial v} \frac{\mathrm{d}\mathcal{H}}{\mathrm{d}E'}(E',v). \tag{1.3.8}$$

Using that $\tilde{\eta}(\infty,t) = 0$ (see (1.3.6)) and $\mathrm{d}\mathcal{H}/\mathrm{d}E'(E',v_\delta) = 0$ (since $E_R^{T,-}(v_\delta) = E_R^{T,+}(v_\delta)$ and the integrand in (1.3.3) is a regular function), the integration by parts of (1.3.8) leads to

$$\frac{\mathrm{d}R}{\mathrm{d}E'} = \int_{v_\delta}^{\infty} \mathrm{d}v_{\rm min} \; \tilde{\eta}(v_{\rm min},t) \frac{\mathrm{d}\mathcal{R}}{\mathrm{d}E'}(E',v_{\rm min}), \tag{1.3.9}$$

where we choose to call $v_{\rm min}$ the integration variable because it makes obvious the physical meaning of $\tilde{\eta}$ as a function of $v_{\rm min}$, and where we define the "differential response function" $\mathrm{d}\mathcal{R}/\mathrm{d}E'$ of the detector as

$$\frac{\mathrm{d}\mathcal{R}}{\mathrm{d}E'}(E',v_{\rm min}) \equiv \frac{\partial}{\partial v_{\rm min}} \left[\frac{\mathrm{d}\mathcal{H}}{\mathrm{d}E'}(E',v_{\rm min}) \right]. \tag{1.3.10}$$

Notice that $\mathrm{d}\mathcal{R}/\mathrm{d}E'$ is a function of the target dependent recoil energies, $E_R^{T,\pm}(v_{\rm min})$, which are functions of the independent variable $v_{\rm min}$. It is clear that, in (1.3.9), all the dependence on the halo model is in the $\tilde{\eta}$ function which is independent of the experimental apparatus, and thus is common to all direct detection experiments. Therefore, by mapping the rate data into $\tilde{\eta}$, it is possible to compare the different experimental results without any assumption on the dark halo of our galaxy.

Due to Earth's rotation around the Sun, the velocity integral (1.3.6) is modulated in time with a 1 year period:

$$\tilde{\eta}(v_{\min}, t) \simeq \tilde{\eta}^0(v_{\min}) + \tilde{\eta}^1(v_{\min}) \cos\left(\frac{2\pi}{\text{yr}}(t - t_0)\right), \tag{1.3.11}$$

where t_0 is the time when the rate reaches its maximum value. The energy-integrated rate $R_{[E_1',E_2']}(t)$ over an energy interval $[E_1', E_2']$ is given in (1.1.5). Since all the time dependence of the rate is contained in $\tilde{\eta}$, we also have that

$$R_{[E_1',E_2']}(t) \simeq R^0_{[E_1',E_2']} + R^1_{[E_1',E_2']} \cos\left(\frac{2\pi}{\text{yr}}(t - t_0)\right), \tag{1.3.12}$$

with

$$\begin{aligned} R^\alpha_{[E_1',E_2']} &\equiv \int_{v_\delta}^{\infty} \mathrm{d}v_{\min}\ \tilde{\eta}^\alpha(v_{\min}) \int_{E_1'}^{E_2'} \mathrm{d}E'\ \frac{\mathrm{d}\mathcal{R}}{\mathrm{d}E'} \\ &= \int_{v_\delta}^{\infty} \mathrm{d}v_{\min}\ \tilde{\eta}^\alpha(v_{\min}) \mathcal{R}_{[E_1',E_2']}(v_{\min}) \end{aligned} \tag{1.3.13}$$

where $\alpha = 0$ or 1. Direct detection experiments can measure the time-average $R^0_{[E_1',E_2']}$ and the annual modulation amplitude $R^1_{[E_1',E_2']}$ of the rate. If the energy-integrated response function $\mathcal{R}_{[E_1',E_2']}(v_{\min})$ for a given energy interval $[E_1', E_2']$,

$$\mathcal{R}_{[E_1',E_2']}(v_{\min}) = \int_{E_1'}^{E_2'} \mathrm{d}E' \frac{\mathrm{d}\mathcal{R}}{\mathrm{d}E'}(E', v_{\min}), \tag{1.3.14}$$

is a well-localized function in a $v_{\min}$ range, the measurements of $R^0_{[E_1',E_2']}$ and $R^1_{[E_1',E_2']}$ can be used to infer the values of $\tilde{\eta}^0$ and $\tilde{\eta}^1$ over the $v_{\min}$ range in which the response function is non-zero. This is true for WIMPs whose differential cross section is inversely proportional to v^2, such as for the usual spin-independent (SI) and spin-dependent interactions. Otherwise $\mathcal{R}_{[E_1',E_2']}$ may need to be regularized (see [50] for the details).

In general $\tilde{\eta}$ can be expanded in a Fourier series, and here we assume that higher modes are not important. The DAMA collaboration did not find any hints of higher modes in their data [16, 61], thus when considering the DAMA data we adopt (1.3.11) with the measured phase t_0 = June 2$^{\text{nd}}$. All other experiments considered here give an upper bound on a time-averaged signal, thus on $\tilde{\eta}^0$. Given that the annual modulation amplitude cannot be larger than the average rate, $|\tilde{\eta}^1(v_{\min})| \leqslant \tilde{\eta}^0(v_{\min})$, we can interpret upper bounds on $\tilde{\eta}^0$ from experiments with null results as (conservative) limits on the $\tilde{\eta}^1$ signal measured by DAMA. We do not consider the direct CDMS-II bound on $\tilde{\eta}^1$ [8], since LUX and SuperCDMS set more stringent constraints, see [25, 51, 52] (notice also that SuperCDMS employs the same target material).

Using the contact SI cross-section from (1.1.4) in (1.3.3)-(1.3.4), we obtain

$$\frac{\mathrm{d}\mathcal{H}^{\mathrm{SI}}}{\mathrm{d}E'}(v, E') \equiv \sum_T \frac{C_T}{2\mu_p^2} \int_{E_R^{T,-}(v)}^{E_R^{T,+}(v)} \mathrm{d}E_R \; \epsilon(E_R, E') G_T(E_R, E') \\ \times [Z_T + (A_T - Z_T)(f_n/f_p)]^2 F_T^2(E_R), \tag{1.3.15}$$

and from (1.3.10), we get the following differential response function:

$$\frac{\mathrm{d}\mathcal{R}^{\mathrm{SI}}}{\mathrm{d}E'}(v_{\min}, E') \equiv \sum_T \frac{C_T}{2\mu_p^2}[Z_T + (A_T - Z_T)(f_n/f_p)]^2 \\ \times \left[\left. \frac{\mathrm{d}E_R^{T,+}}{\mathrm{d}v} \right|_{v=v_{\min}} \epsilon(E_R^{T,+}(v_{\min}), E') G_T(E_R^{T,+}(v_{\min}), E') F_T^2(E_R^{T,+}(v_{\min})) \right. \\ \left. - \left. \frac{\mathrm{d}E_R^{T,-}}{\mathrm{d}v} \right|_{v=v_{\min}} \epsilon(E_R^{T,-}(v_{\min}), E') G_T(E_R^{T,-}(v_{\min}), E') F_T^2(E_R^{T,-}(v_{\min})) \right]. \tag{1.3.16}$$

For elastic scattering this reduces to

$$\frac{\mathrm{d}\mathcal{R}^{\mathrm{SI}}}{\mathrm{d}E'}(v_{\min}, E') \equiv \sum_T 2 v_{\min} \frac{C_T}{m_T} \epsilon(E_R, E') G_T(E_R(v_{\min}), E') \\ \times \frac{\mu_T^2}{\mu_p^2}[Z_T + (A_T - Z_T)(f_n/f_p)]^2 F_T^2(E_R(v_{\min})). \tag{1.3.17}$$

CHAPTER 2

Direct Detection of Light "Ge-phobic" Exothermic Dark Matter

It was first shown in 2004 [62] that light WIMPs with spin-independent isospin-conserving interactions with nuclei could simultaneously provide a viable DM interpretation of the DAMA annual modulation [13] and be compatible with all negative searches at the time, assuming the SHM for the dark halo of our galaxy. The interest in these candidates intensified as new hints of light WIMPs appeared, first in the DAMA 2008 data [14] (see e.g. [63]) and then in the data of CoGeNT, CRESST-II and CDMS-II-Si. In the following, we include all the regions obtained from the DAMA, CDMS-II-Si and CoGeNT data, and the most relevant limits derived from direct DM searches with null results by the LUX [10], XENON10 [1], CDMSlite [64], SuperCDMS [11] and SIMPLE [5] collaborations (with SIMPLE relevant only for isospin-violating [65, 66] interactions).

In this chapter we consider exoDM as a potential explanation of the signals found by CDMS-II-Si. As already explained in the introduction, exothermic scattering favors lighter targets with respect to heavier ones, and thus suppresses the limits due to Xe. We present our results for WIMPs with elastic isospin-conserving and isospin-violating SI interactions, and exothermic inelastic isospin-violating SI interactions. The isospin-conserving choice $f_n = f_p$ is usually assumed by the experimental collaborations. However, the value of f_n/f_p that minimizes the coupling $\sum_T [1 + (f_n/f_p)(A_T - Z_T)/Z_T]^2 (C_T/m_T)$ for a particular target element, where the sum runs over its isotopes, is also possible (see (1.1.4) for the spin-independent scattering cross section). The isospin-violating choice $f_n/f_p = -0.7$ [65, 66]

produces the maximum cancellation of the WIMP coupling to Xe, suppressing very effectively the interaction cross section for this target. In our case, the exothermic character of the DM interactions weakens the Xe-based limits for large enough mass splitting. Thus we consider the value $f_n/f_p = -0.8$, which suppresses most efficiently the WIMP coupling with a Ge target. This ad-hoc choice, which we call "Ge-phobic", weakens the SuperCDMS limits maximally and it is equally motivated (or not motivated) as the "Xe-phobic" -0.7 choice.

In Sec. 2.1 we describe the data analysis we perform, and in Secs. 2.2 and 2.3 we present our results assuming the SHM and in a halo-independent manner, respectively. We give our conclusions in Sec. 2.4.

2.1 Data analysis

We describe here the data analysis we perform assuming the SHM, which follows the procedure already presented in [51, 52]. The Python implementation can be found in [53]. We compute the 68% and 90% CL allowed regions from the DAMA (Na only) and CoGeNT 2011-2012 modulation data [19] and from the CDMS-II-Si unmodulated signal using the Extended Maximum Likelihood method [67]. For CDMS-II-Si we use the three events observed in their signal region with recoil energies 8.2, 9.5, and 12.3 keV. We use the Maximum Gap Method [68] to produce 90% CL bounds on the m–σ_p parameter space from the LUX, CDMS-II-Si, CDMSlite, SuperCDMS, and XENON10 experiments. The CoGeNT 2011-2012 unmodulated rate bound is the 90% CL limit (in a raster scan).

To compute the LUX bound, following [51], we apply the Maximum Gap method [68] to the variable S_1 in the range 2–30 photoelectrons. We choose several numbers of observed events, i.e. 0, 1, 3, 5 and 24 as described in [51]. In our SHM model the maximum WIMP speed is $v_{\max} = 765$ km/s, thus the maximum recoil energy for a WIMP lighter than 11.5 GeV in an elastic scattering with Xe is ~ 12 keV. Using the approximated recoil energy contours in Fig. 4 of [10], and dropping all observed events in and above the electron-recoil band (plotted at 1.28σ) in the same figure, only five observed events remain below ~ 12 keV. This means that for elastic scattering, choosing 5 events provides a safe upper limit for WIMP masses $m < 11.5$ GeV. However, if $m > 11.5$ GeV, only using all the 24 events lying outside the electron-recoil band provides a reliable upper limit. For inelastic scattering with

$\delta = -50$, -30, 50 and 100 keV, the maximum WIMP masses for which using the 5 events bound is reliable are 8.2, 9.3, 19.2 and 56.2 GeV, respectively. Since our procedure does not depend on the WIMP distribution in the S_1–$\log_{10}(S_2/S_1)$ plane [10], our Maximum Gap upper limits are conservative and safe to be applied to any WIMP-nucleus interactions.

For the SuperCDMS bounds, we use the data set collected by the seven Ge detectors between October 2012 and June 2013, corresponding to an effective exposure of 577 kg-days. We use the Maximum Gap method with the eleven observed events listed in Table 1 of [11], which passed the selection criteria introduced by the collaboration to discriminate signal from background events. We do not incorporate the uncertainty in recoil energy in our analysis. For the detector acceptance we take the red curve in Fig. 1 of [11].

To compute the SIMPLE limits, we consider only the Stage 2 [5], a C_2ClF_5 detector with an exposure of 6.71 kg-day, with one observed event above 8 keV compatible with the expected background of 2.2 events. We use the Feldman-Cousins method [69] to place a 90% CL upper limit of 2.39 signal events for 2.2 expected background events and 1 observed event.

For our halo-independent analysis, we follow the procedure developed and described in [25, 48, 50, 51]. The data analysis for CoGeNT is the same as in [52], except for the binning of the CoGeNT data for our halo-independent analysis (here we took two bins, 0.5–2.0 KeVee and 2.0–4.5 keVee, the same as in [20]).

2.2 Data comparison assuming the SHM

Figs. 2.1 and 2.2 show the 90% confidence level (CL) bounds and 68% and 90% CL allowed regions for DAMA, CoGeNT 2014 and CDMS-II-Si in the WIMP-proton cross section σ_p vs WIMP mass m plane, assuming the SHM, for spin-independent isospin-conserving interactions, and for elastic and inelastic scattering with $\delta = -50, -200$ and -500 keV (in Figs. 2.1.a, 2.1.b, 2.2.a and 2.2.b respectively). As the mass difference δ between the DM mass eigenstates increases, it becomes progressively more difficult to insure that the lifetime of the metastable DM state is larger than the lifetime of the Universe. Looking at Eq. 9 of [39] (see also [35]) it seems that the values we consider are still safe in this respect.

The irregular shape of the limits, more noticeable for larger negative δ values, is due to

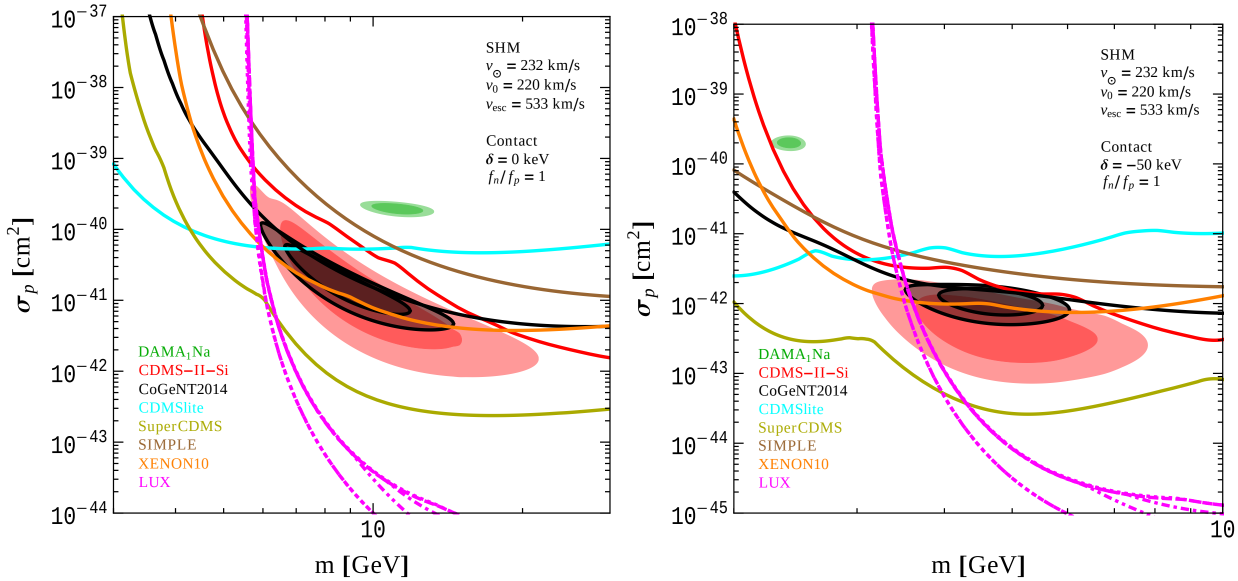

Figure 2.1. 90% CL bounds and 68% and 90% CL allowed regions in the WIMP-proton cross section σ_p vs WIMP mass plane, assuming the SHM, for spin-independent isospin-conserving interactions for a) (left) elastic scattering ($\delta = 0$) and b) (right) inelastic exothermic scattering with $\delta = -50$ keV. The DAMA region is due to scattering off sodium (with $Q_{\rm Na} = 0.30$).

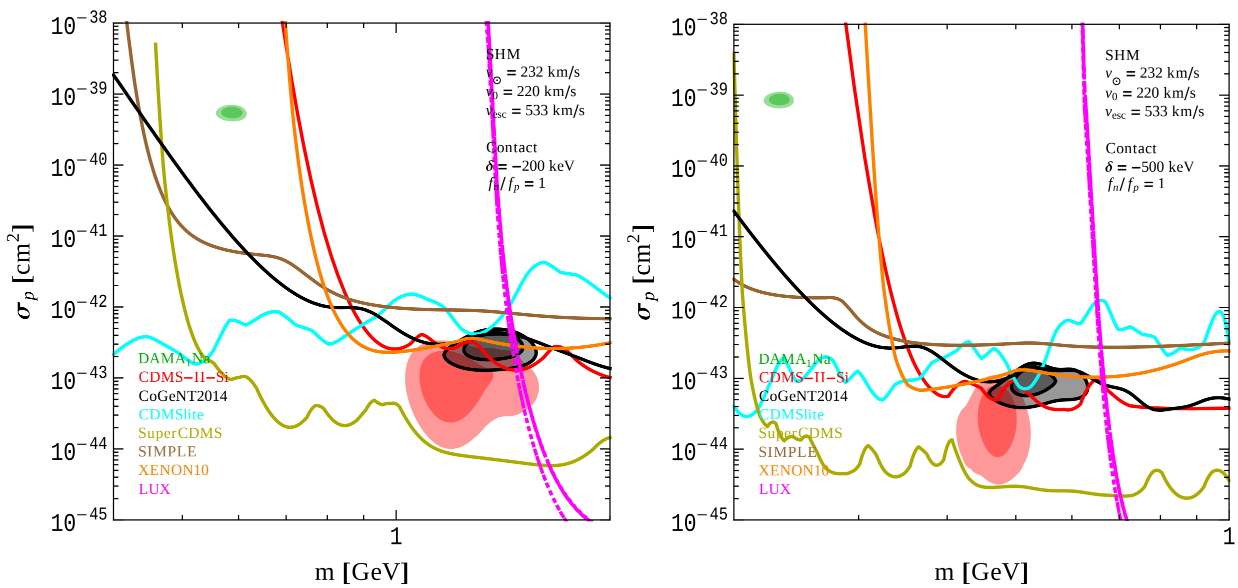

Figure 2.2. Same as Fig. 2.1 but for a) (left) $\delta = -200$ keV and b) (right) $\delta = -500$ keV.

the rapid change of the interval chosen as the maximum gap since the narrow allowed energy range changes rapidly with m (see Fig. 1.1).

For CDMS-II-Si we found that, already for $\delta = -200$ keV, in the lower mass part of the best fit region the highest-energy event of the three observed events must be background (since a DM interaction would be kinematically forbidden; see Fig. 1). For $\delta = -500$ keV, in the lower mass part of the allowed CDMS-II-Si region only the lowest-energy event is due to DM, while in the higher mass part only the two lowest-energy events are due to DM. This is not a problem in our statistical analysis because we have included both the signal and background contributions in the Extended Likelihood function [52].

Notice how the DAMA region moves progressively to lower WIMP mass values with respect to the CoGeNT and CDMS-II-Si regions, as the negative δ value increases. This is because the signal in DAMA is the annual modulation of the rate, and the observed phase of the modulation require WIMP speeds larger than approximately 200 km/s in the SHM (for lower speeds the modulation amplitude changes sign, i.e. the times of maximum and minimum rate are reversed). With exothermic interactions even WIMPs with very low speeds could have energies above the experimental threshold of DAMA, unless the WIMP mass is sufficiently small. The CoGeNT and CDMS-II-Si regions are derived from unmodulated rate measurements instead.

Figs. 2.1 and 2.2 show that, when assuming the SHM, considering exoDM per se does not bring about compatibility between the potential signal regions and the upper limits in the m-σ_p plane. The exothermic scattering is effective in weakening the xenon-based limits (the most important of which is LUX), but does little to suppress the germanium-based SuperCDMS limit which remains very restrictive because of the very low energy threshold of the experiment (1.6 keVnr).

On the other hand, as can be seen in Fig. 2.3, for WIMPs with isospin-violating "Ge-phobic" $f_n/f_p = -0.8$ coupling and elastic scattering, the 90% CL LUX limit rejects all 90% CL regions of interest (although the "Xe-phobic" coupling $f_n/f_p = -0.7$ allows a very small sliver of the CDMS-II-Si). It is the combination of exothermic scattering (which weakens the LUX limits) and the isospin-violating couplings that could allow the CDMS-II-Si to be compatible with all present limits. This is shown in Figs. 2.4, 2.5 and 2.6 for $\delta = -50, -200$ and -500 keV respectively. Notice that the isospin-violating couplings separate the CoGeNT and CDMS-II-Si regions, which instead overlap when isospin-conserving couplings are considered (see Figs. 2.1 and 2.2). Thus the CoGeNT region is rejected even when the CDMS-II-Si is allowed.

Figs. 2.4, 2.5 and 2.6 show clearly the different effects of the "Xe-phobic" and "Ge-phobic"

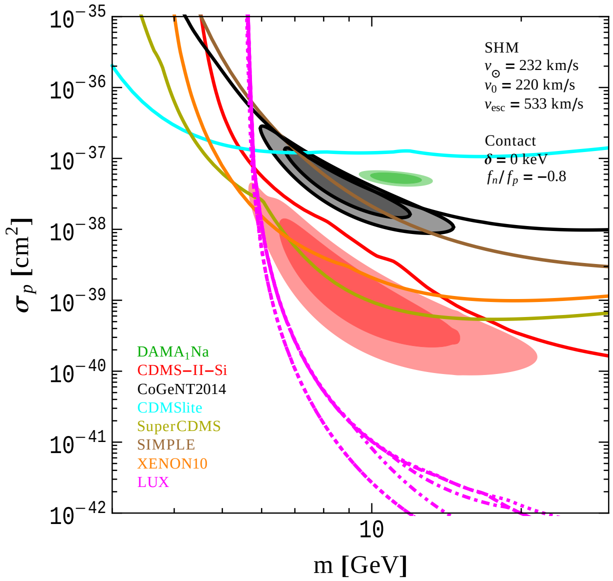

Figure 2.3. Same as Fig. 2.1 but for the spin-independent isospin-violating interactions with $f_n/f_p = -0.8$ and elastic scattering ($\delta = 0$).

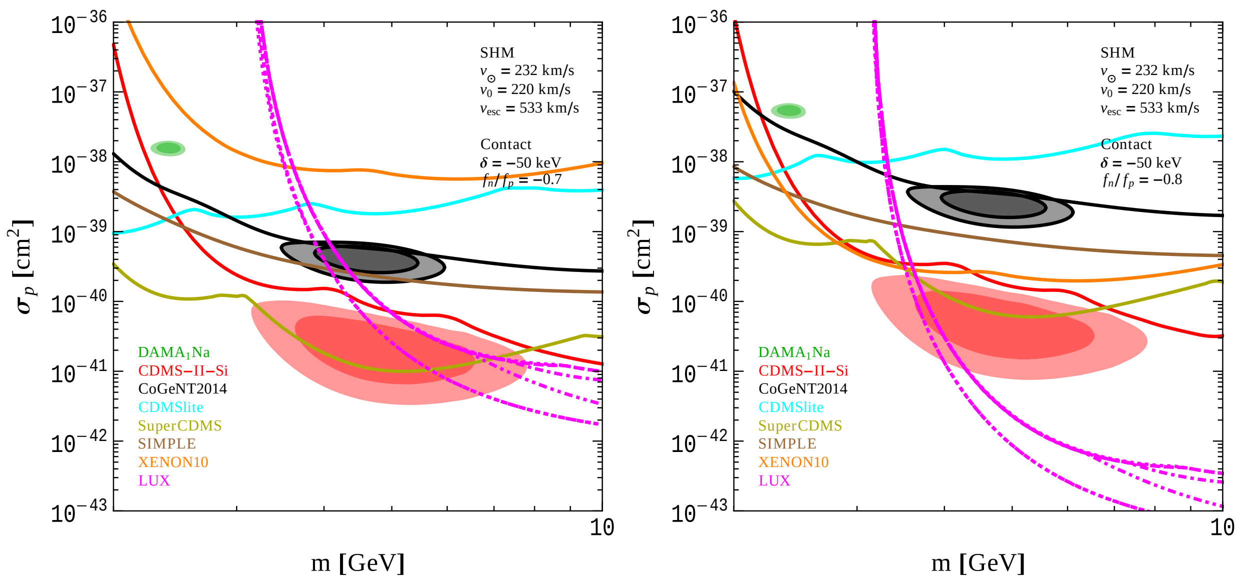

Figure 2.4. Same as Fig. 2.3 but for the spin-independent isospin-violating interactions with a) (left) $f_n/f_p = -0.7$ ("Xe-phobic") and b) (right) $f_n/f_p = -0.8$ ("Ge-phobic"), for inelastic exothermic scattering with $\delta = -50$ keV.

choices in weakening maximally the LUX and the SuperCDMS limits respectively.

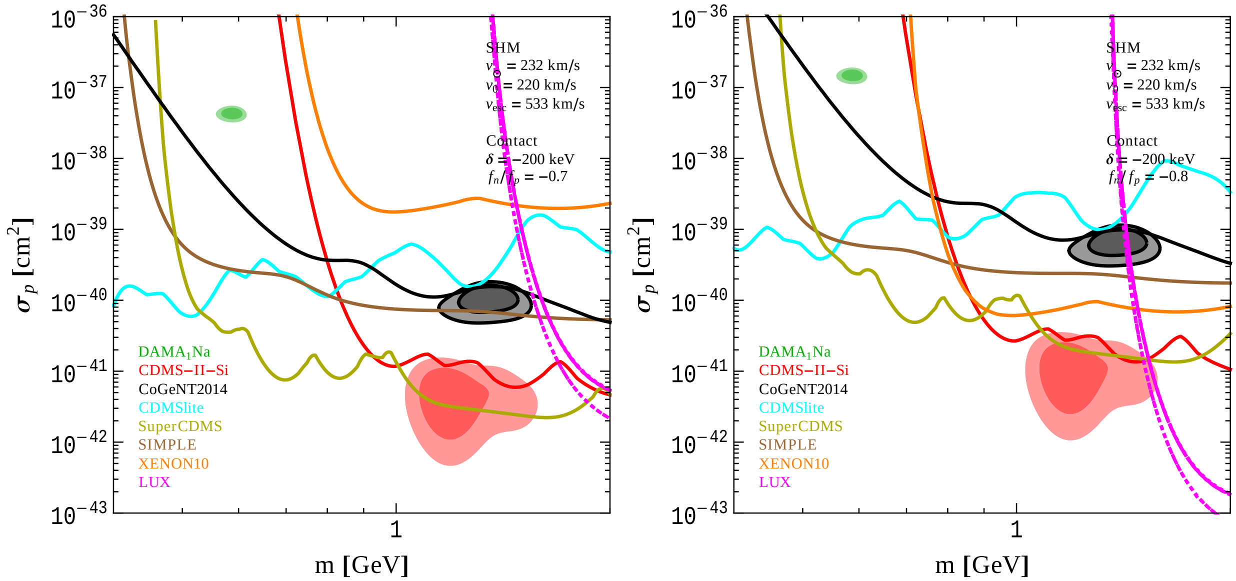

Figure 2.5. Same as Fig. 2.4 but for $\delta = -200$ keV.

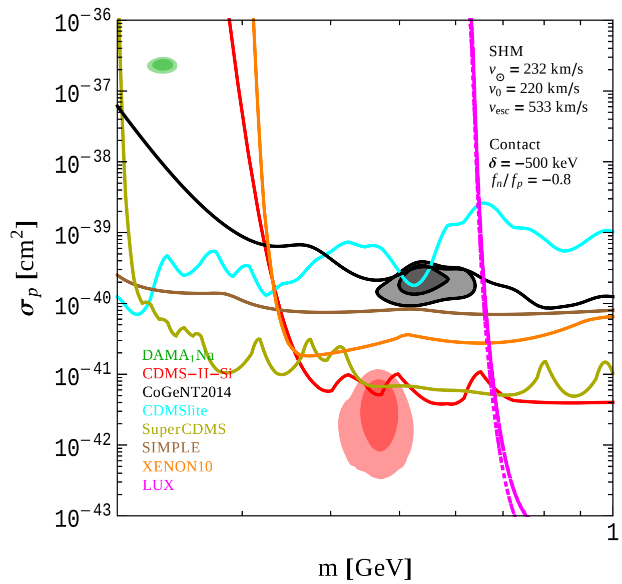

Figure 2.6. Same as Fig. 2.5.a but for $\delta = -500$ keV. In this case only the lowest-energy or the two lowest-energy events of the three events observed by CDMS-II-Si are due to DM.

2.3 Halo-independent data comparison

Here we present the averages of $\tilde{\eta}^0(v_{\rm min})$ (for CDMS-II-Si and CoGeNT) and $\tilde{\eta}^1(v_{\rm min})$ (for DAMA) compared with the most relevant upper limits, as functions of $v_{\rm min}$. For exothermic scattering the relation between energy and $v_{\rm min}$ intervals is more complicated than for elastic scattering. Notice in Fig. 1.1 that if the boundaries of an energy bin cross the upper E_R branch, $E_R^{+,T}$ (with the target $T = \text{Si}$ for CDMS-II-Si), higher recoil energies correspond to higher values of $v_{\min}$ (the same happens for elastic scattering, for which only the upper E_R branch exists). This is the case in Figs. 2.7 and 2.8 for the three CDMS-II-Si energy bins we adopted, 7 to 9 keV, 9 to 11 keV and 11 to 13 keV (each containing one observed event). However, if the δ and m values are such that the boundaries of an energy bin cross the lower E_R branch, $E_R^{-,T}$, the $v_{\min}$ intervals are inverted: the largest $v_{\min}$ boundary corresponds to the smallest energy boundary and vice versa. If instead E_δ^T is included in the energy interval, $v_{\min}$ extends all the way to $v_{\min} = 0$. This is the case in Fig. 2.9 for the three CDMS-II-Si energy bins we adopted.

Figs. 2.7 and 2.8 show the measurements of and upper bounds on $\tilde{\eta}^0(v_{\min})$ (for CDMS-II-Si and CoGeNT) and $\tilde{\eta}^1(v_{\min})$ (for DAMA) for inelastic exothermic scattering with $\delta = -50$ keV for a WIMP with mass $m = 3.5$ GeV. The two $E_R^{\pm}$ branches for this δ and m combination for scattering off Si are shown as the orange lines in Fig. 1.1. The CDMS-II-Si intervals in $v_{\min}$, shown as the horizontal bars of the three $\tilde{\eta}^0(v_{\min})$ crosses, are ordered in the same way as the three energy intervals. In Fig. 2.7 the interaction assumed is spin-independent isospin-conserving and the tension between the CDMS-II-Si crosses and the SuperCDMS and LUX limits is apparent. This tension is clearly alleviated in Fig. 2.8.a and b when the "Xe-phobic" choice $f_n/f_p = -0.7$ or the "Ge-phobic" choice $f_n/f_p = -0.8$ are respectively made. This is largely the same conclusion we reached in our SHM analysis.

Our last figure, Fig. 2.9, is more difficult to interpret than the previous ones. It corresponds to $\delta = -200$ keV and mass $m = 1.3$ GeV, a combination for which the two $E_R^{\pm,T}$ branches are shown in green in Fig. 1.1. Because our halo-independent analysis extends to larger speeds than in the SHM, up to 1000 km/s (accounting for potential extreme values of the escape velocities encountered in some halo models), the three CDMS-II-Si events are contained in the allowed recoil energy interval, as we can see in Fig. 1.1. The difficulty comes in the relation between the energy and the $v_{\min}$ intervals for CDMS-II-Si. It is clear from Fig. 1.1 that the first CDMS-II-Si energy bin, 7 to 9 keV, crosses the lower E_R branch, and thus its corresponding $v_{\min}$ interval is inverted. It is also located at higher $v_{\min}$ values than the interval corresponding to the second energy bin, 9 to 11 keV, which contains E_δ^T and thus extends to $v_{\min} = 0$. Only the largest energy bin crosses the upper E_R branch, and is

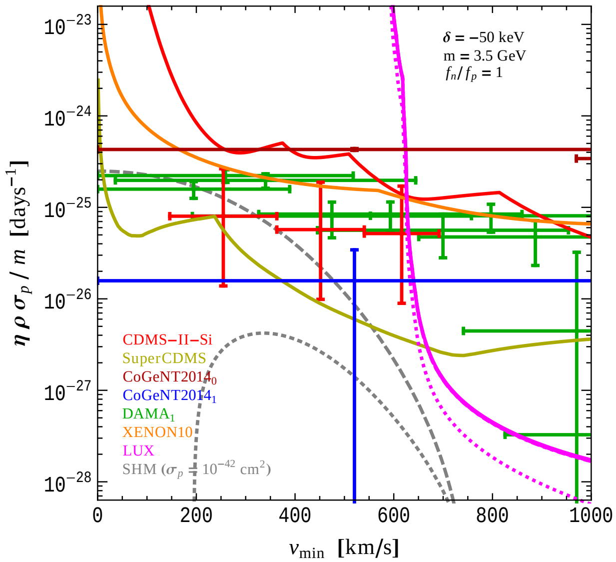

Figure 2.7. Measurements of and upper bounds on $\tilde{\eta}^0(v_{\rm min})$ (for CDMS-II-Si and CoGeNT) and $\tilde{\eta}^1(v_{\rm min})$ (for DAMA) for inelastic exothermic scattering with $\delta = -50$ keV for a WIMP with mass $m = 3.5$ GeV and spin-independent isospin-conserving interactions. Only the scattering in Na is considered in DAMA($Q_{\rm Na} = 0.30$). The dashed gray lines show the SHM $\tilde{\eta}^0$ (upper line) and $\tilde{\eta}^1$ (lower line) for $\sigma_p = 1 \times 10^{-42}$ cm^2, which in Fig. 2.1.b is within the CDMS-II-Si region.

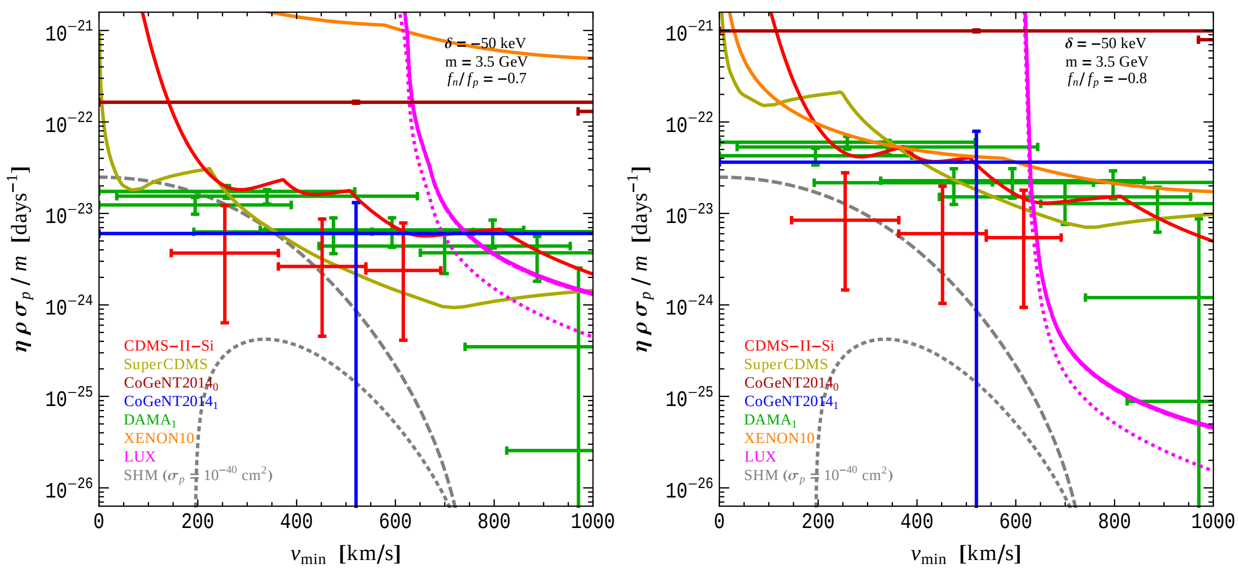

Figure 2.8. Same as in Fig. 2.7 but for isospin-violating couplings with a) (left) $f_n/f_p = -0.7$ and b) (right) $f_n/f_p = -0.8$. The dashed gray lines show the SHM $\tilde{\eta}^0$ (upper line) and $\tilde{\eta}^1$ (lower line) for $\sigma_p = 1 \times 10^{-40}$ cm^2, which in Fig. 2.4.b is within the CDMS-II-Si region allowed by all upper bounds.

as expected in elastic collisions. It is clearly seen in Fig. 2.9 that the SuperCDMS limit is below the CDMS-II-Si crosses in Fig. 2.9.a, where $f_n/f_p = 1$, and it is instead above the CDMS-II-Si crosses in Fig. 2.9.b, where $f_n/f_p = -0.8$. Notice that the LUX bound in this case only affects $v_{\rm min}$ values above 800 km/s, i.e. above the maximum speed values in the

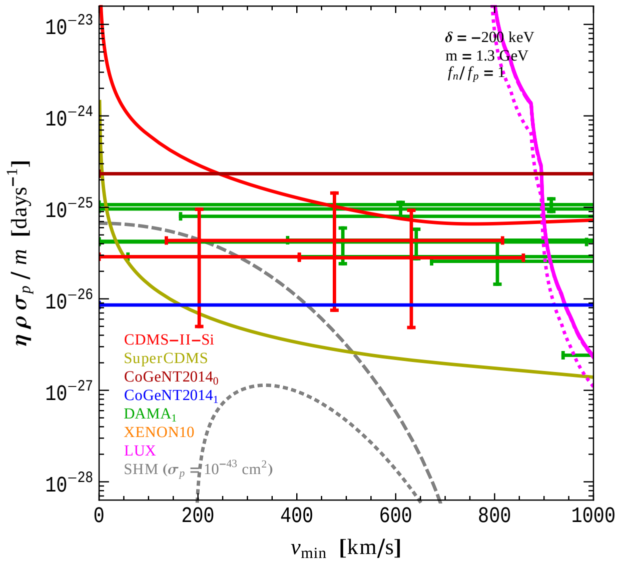

Figure 2.9. Measurements of and upper bounds on $\tilde{\eta}^0(v_{\rm min})$ (for CDMS-II-Si and CoGeNT) and $\tilde{\eta}^1(v_{\rm min})$ (for DAMA) for inelastic exothermic scattering with $\delta = -200$ keV for a WIMP with mass $m = 1.3$ GeV and a) (left) spin-independent isospin-conserving interactions or b) (right) spin-independent isospin-violating coupling with $f_n/f_p = -0.8$. The dashed gray lines show the SHM $\tilde{\eta}^0$ (upper line) and $\tilde{\eta}^1$ (lower line) for a) $\sigma_p = 1 \times 10^{-43}$ cm^2 and b) $\sigma_p = 1 \times 10^{-41}$ cm^2 which in Fig. 2.2.a and Fig. 2.5.b respectively are within the CDMS-II-Si region allowed by all upper bounds.

SHM.

In all our halo-independent plots there is only one cross in blue and only one in brown, corresponding to the CoGeNT 2014 annual modulation and total rate respectively [20], in the first of the two energy bins we adopted, extending from $v_{\rm min} = 0$ to very large values of $v_{\rm min}$. These are almost entirely rejected by the SuperCDMS limit.

2.4 Conclusions for Chapter 2

We have considered light WIMPs with inelastic exothermic scattering, in which a heavier DM state becomes de-excited to a lighter DM state. In our SHM analysis the CoGeNT and DAMA regions are rejected by present bounds. In our halo-independent analysis, the situation seems of strong tension, since only the lowest $v_{\rm min}$ portion of the data points remain outside the upper limits.

In both our SHM and halo-independent analyses the conclusion we reach is similar, namely that the CDMS-II-Si signal region can still be compatible with all present upper limits, in particular the LUX and the SuperCDMS limits, with a combination of two assumptions: exothermic scattering and spin-independent isospin-violating interactions. The reason is that the exothermic character of the scattering weakens the Xe-based limits, the LUX bound in particular, but does not weaken significantly the SuperCDMS bound because of the low energy threshold of this experiment. This limit can be further relaxed by an isospin-violating coupling which suppresses the WIMP-Ge coupling. In particular, the choice of $f_n/f_p = -0.8$ for the neutron to proton coupling ratio reduces this coupling maximally. We call this choice "Ge-phobic".

That nature would choose for the dark matter the particular combination of characteristics which weakens the best experimental upper limits at a particular moment seems too much of a coincidence but, like always, more data will confirm or disprove this scenario.

CHAPTER 3

Extended Maximum Likelihood Halo-independent Analysis of Dark Matter Direct Detection Data

In earlier implementations of the halo-independent method, only weighted averages over $v_{\min}$ intervals of the time average, $\tilde{\eta}^0(v_{\min})$, and annual modulation amplitudes, $\tilde{\eta}^1(v_{\min})$, of $\tilde{\eta}(v_{\min}, t)$ have been obtained from putative DM signals in direct detection. These averages over $v_{\min}$ intervals are represented in plots by a set of crosses in the $v_{\min} - \tilde{\eta}$ plane, whose vertical and horizontal bars show the uncertainty in $\tilde{\eta}^0(v_{\min})$ or $\tilde{\eta}^1(v_{\min})$ and the $v_{\min}$ range where they are measured, respectively. Combined with upper limits, these crosses can be used to assess the compatibility of data sets from various experiments. However, making a statistically meaningful evaluation of the compatibility of the data in this manner is not possible.

The compatibility of different data has been studied in [70] using the "parameter goodness-of-fit" test statistic [71]. The analysis is based on the likelihoods maximized with $\tilde{\eta}^0$ written as a sum of a very large number of step functions, following a method presented in [72]. In this case, the level of compatibility is given by the p-value of the test statistic, which was calculated by Monte Carlo simulations in [70]. Another test statistic for comparing one data set with a positive result and another with a negative result has been defined in [73].

An alternative method to study the compatibility of a positive result with upper limits uses a band in $v_{\min} - \tilde{\eta}^0$ space at a given confidence level [55], derived from unbinned data, with an extended likelihood [67]. In this case, as shown in [55] for single-nuclide detectors, the likelihood is maximized by a non-increasing piecewise constant $\tilde{\eta}^0$ function, because of the exponential prefactor in the extended likelihood.

The proof presented in [55] relies on the assumption that the target is made of a single component. The main limitation of the approach of [55] relies on their use of the recoil energy E_R as independent variable. Here we provide a derivation of the extended maximum likelihood halo-independent (EHI) analysis method using $v_{\rm min}$ as a variable, which applies to any type of WIMP interaction, including inelastic scattering, and any target composition. We correct and extend the original proof of [55] using the formulation developed for the generalized halo-independent analysis in [50]. The proof for the realistic case of finite experimental energy resolution presented in [55] relies on the application to the likelihood functional maximization of the Karush-Kuhn-Tucker (KKT) conditions in [74, 75]. The KKT conditions in [74, 75], however, apply only to the minimization of functions with a finite number of variables subject to a finite number of inequalities, and they do not apply to functionals. Eqs. (A.3) to (A.6) of [55] are given without proof and without a reference. Moreover, Eq. (A.4) seems problematic for a $\tilde{g}$ function (which in our paper we call $\tilde{\eta}$) that has discontinuities, as in the solutions found in [55]. In this case, Eq. (A.4) requires a Dirac δ function to be smaller than or equal to zero, which is mathematically problematic. As we explain in Sec. 3, although the KKT conditions have been extended to functionals defined on specific kinds of function spaces and constraints, we did not find in the literature a proof that clearly applies to our problem. Thus, in Sec. 3 we present our own proof of the KKT conditions we use, Eqs. (3.1.22)-(3.1.25), which are clearly valid for discontinuous functions.

As in [55], here we find that the best fit $\tilde{\eta}$ function is piecewise constant with a number of discontinuities at most equal to the number of observed events. In [55], this is a result found for $\tilde{g}$ given as a function of the recoil energy, which can be easily translated to $v_{\rm min}$ space only for a single target nuclide. Besides, the proof in [55] applies only to resolution functions with certain properties. We instead prove the result for $\tilde{\eta}$ as a function of $v_{\rm min}$ for any target composition and general resolution functions.

Besides these extensions, we make a correction to the method of [55] by providing a clear definition of the uncertainty band. In [55], the uncertainty band is defined in Eq. (2.16) through a numerical Monte Carlo simulation. In Sec. 4, we explain our objections to this procedure. We define instead a pointwise confidence band with a new method (see Sec. 4.2) and provide a clear statistical interpretation for this band using Wilks' theorem. The different definitions of the band, here and in [55], yield very different values of the parameter ΔL defined in both papers for the same confidence level.

In an earlier chapter, in Sec. 1.3, we reviewed the formulation of the generalized halo-independent analysis, on which the following sections are based. In Sec. 3.1, we prove crucial properties of the extended likelihood for unbinned direct DM detection data. In Sec. 3.2, we develop the EHI analysis method, and discuss the statistical interpretation of the confidence band computed with this method. In Sec. 3.3, we apply the method to the CDMS-II-Si [22] data for WIMPs with elastic isospin-conserving and isospin-violating SI interactions [65, 66, 76], and exothermic inelastic isospin-violating SI interactions [34, 77], and compare the results with the upper limits imposed by other experiments. Finally, we give our conclusions in Sec. 3.4.

3.1 Piecewise constant $\tilde{\eta}(v_{\min})$ resulting from the EHI method

Most direct detection experiments measure energy-integrated rates and/or their annual modulation amplitudes in given energy intervals. CDMS-II-Si gives instead the recoil energies of three candidate DM events. Most halo-independent analyses of the CDMS-II-Si candidate events have chosen a binning scheme, which is arbitrary and may lose some of the information in the data [25, 34, 36, 48, 50, 52, 77].

Reference [55] has introduced a halo-independent analysis method without binning. The method relies on the fact that the extended likelihood [67] yields piecewise constant functions as solutions of the likelihood maximization. The extended likelihood for unbinned data can be written as

$$\mathcal{L}[\tilde{\eta}(v_{\min})] \equiv e^{-N_E[\tilde{\eta}]} \prod_{a=1}^{N_O} MT \, \frac{\mathrm{d}R_{tot}}{\mathrm{d}E'}\bigg|_{E'=E'_a} . \tag{3.1.1}$$

For simplicity we use $\tilde{\eta}$ here for the time-average component of the $\tilde{\eta}$ function (we call it $\tilde{\eta}^0$ in previous sections). Here N_O is the total number of observed events, each with energy E'_a, with $a = 1, \ldots, N_O$. $N_E[\tilde{\eta}]$ is the total number of expected events within the energy range

$[E'_{\rm min}, E'_{\rm max}]$ detectable in the experiment, which we write as a functional of the function $\tilde{\eta}(v_{\rm min})$:

$$N_E[\tilde{\eta}] = N_{BG} + MT \int_{v_\delta}^{\infty} \mathrm{d}v_{\rm min} \tilde{\eta}(v_{\rm min}) \mathcal{R}_{[E'_{\rm min}, E'_{\rm max}]}(v_{\rm min}), \tag{3.1.2}$$

where N_{BG} is the expected number of background events

$$N_{\rm BG} \equiv MT \int_{E'_{\rm min}}^{E'_{\rm max}} dE' \frac{dR_{\rm BG}}{dE'}. \tag{3.1.3}$$

Here MT is the detector exposure, $\mathrm{d}R_{tot}/\mathrm{d}E'$ is the total predicted differential event rate

$$\begin{aligned} \frac{\mathrm{d}R_{tot}}{\mathrm{d}E'} &= \frac{\mathrm{d}R_{\rm BG}}{\mathrm{d}E'} + \frac{\mathrm{d}R}{\mathrm{d}E'} \\ &= \frac{\mathrm{d}R_{\rm BG}}{\mathrm{d}E'} + \int_{v_\delta}^{\infty} \mathrm{d}v_{\rm min} \tilde{\eta}(v_{\rm min}) \frac{\mathrm{d}\mathcal{R}}{\mathrm{d}E'}(v_{\rm min}), \end{aligned} \tag{3.1.4}$$

and $\mathrm{d}R_{\rm BG}/\mathrm{d}E'$ is the differential rate of the background events. Writing the rate in this form allows to take into account a non-trivial target composition (not included in [55]), through the differential response function $\mathrm{d}\mathcal{R}/\mathrm{d}E'$, defined in (1.3.3) and (1.3.10), or in (1.3.16) for SI interactions.

Without fixing the halo model, the likelihood function in (3.1.1) is actually a functional of the $\tilde{\eta}$ function. If there is no uncertainty in the measurement of recoil energies, for a single target nuclide it was proven in [55] that the likelihood is maximized by a piecewise constant $\tilde{\eta}$ function with the number of steps equal to or smaller than the number of observed events, N_O. The proof for the realistic case with a finite energy resolution presented in [55] applies only to resolution functions with certain properties such as having a single local maximum, and relies on the application to the likelihood functional maximization of the Karush-Kuhn-Tucker (KKT) conditions in [74, 75]. The KKT conditions in [74, 75] apply to the minimization of functions with a finite number of variables subject to a finite number of inequalities. The proofs in [74, 75] do not apply to functionals. The likelihood $\mathcal{L}[\tilde{\eta}]$ in (3.1.1) is instead a functional of $\tilde{\eta}(v_{\rm min})$ subject to an infinite number of inequalities, one for each value of $v_{\rm min}$. The inequality given in Eq. (A.4) of [55], $\mathrm{d}\tilde{\eta}/\mathrm{d}E_R$ in our notation, is actually an infinite set of inequalities, one for each E_R.

The KKT conditions have been extended to functionals defined on specific kinds of function spaces and constraints. Banach spaces have been considered extensively (see e.g. [78]).

However, the functions we are looking for, i.e. step functions, do not have derivatives everywhere unless interpreted as distributions, and the spaces of distributions defined on non-compact intervals like $[0, \infty)$ are not Banach (under the usual weak-* topology). More general spaces, i.e. locally convex topological vector spaces, have been considered by Dubovitskii and Milyutin [79]. As explained in the book by R. B. Holmes [80] (see pages 51 to 53), the Dubovitskii and Milyutin theory applies to constrained sets of functions that have non-empty interiors. However, the set of non-increasing functions such as $\tilde{\eta}$ has empty interior. A function $\tilde{\eta} \in S$ is in the interior of a set S if there is a neighborhood around it that belongs to the set, but for non-increasing functions there is no such neighborhood. This is because a non-increasing function always has a non-monotonic function arbitrarily close to it.

Since we did not find in the literature any proof that clearly applies to our problems, in the following we present our own proof by first discretizing the variable $v_{\min}$ into a finite set of values $v_{\min}^i$ so that the KKT conditions are applicable, and then taking the continuum limit at the end. Our proof is heuristic only in that it does not address the convergence of the limit.

For convenience, let us define a different functional of $\tilde{\eta}$, (-2 times the log-likelihood),

$$L[\tilde{\eta}] = -2 \ln \mathcal{L}[\tilde{\eta}]. \tag{3.1.5}$$

With this definition, finding the $\tilde{\eta}$ function that maximizes the extended likelihood is equivalent to finding the function that minimizes L. To simplify the problem, we discretize the $v_{\min}$ space into a set of $K + 1$ positive variables $v_{\min}^i = v_\delta + i \times \Delta v$ with $i = 0, 1, \ldots, K$, where $\Delta v \equiv (v^{\text{MAX}} - v_\delta)/K$ with a large enough constant v^{MAX} value. At the end, we will take $K \to \infty$ while keeping v^{MAX} constant.

With a K-dimensional vector $\vec{\tilde{\eta}} = (\tilde{\eta}_0, \tilde{\eta}_1, \ldots, \tilde{\eta}_{K-1})$, we can define a piecewise constant function $\tilde{\eta}(v_{\min}; \vec{\tilde{\eta}})$ given by

$$\tilde{\eta}(v_{\min}; \vec{\tilde{\eta}}) \equiv \tilde{\eta}_i \text{ if } v_{\min}^i \leq v_{\min} < v_{\min}^{i+1}. \tag{3.1.6}$$

Notice that there is no loss of generality of the $\tilde{\eta}(v_{\min})$ considered, since any physically meaningful function is the limit of a sequence of piecewise constant functions as the number of steps tends to infinity. The corresponding L functional becomes a function f_L of the vector

$\vec{\tilde{\eta}}$,

$$f_L(\vec{\tilde{\eta}}) \equiv L[\tilde{\eta}(v_{\min}; \vec{\tilde{\eta}})]. \tag{3.1.7}$$

With this discretization we can formalize the minimization of the functional L as a limit of the function minimization of f_L, and by doing so we can safely apply the KKT conditions.

The KKT conditions for minimizing the function $f_L(\vec{\tilde{\eta}})$ under the constraints $\tilde{\eta}_i \geq \tilde{\eta}_{i+1}$ on its variables (i.e. requiring the piecewise constant function $\tilde{\eta}(v_{\min}; \vec{\tilde{\eta}})$ to be non-increasing) are the minimization conditions for the function

$$f'_L(\vec{\tilde{\eta}}, \vec{q}) \equiv f_L(\vec{\tilde{\eta}}) + \sum_{i=0}^{K-1} q_i(\tilde{\eta}_{i+1} - \tilde{\eta}_i) \tag{3.1.8}$$

with respect to the variables $\vec{\tilde{\eta}}$ and $\vec{q} \equiv (q_0, \ldots, q_{K-1})$ considered as unconstrained, and the supplementary conditions $q_i \geq 0$ and $q_i(\tilde{\eta}_{i+1} - \tilde{\eta}_i) = 0$. Written explicitly, the KKT conditions are:

$$\begin{aligned}
&(\text{KKT I})_{\text{a}} \qquad && \frac{\partial f_L}{\partial \tilde{\eta}_i} + q_{i-1} - q_i = 0, \text{ for } 1 \leq i \leq K-1, && (3.1.9)\\
&(\text{KKT I})_{\text{b}} && \frac{\partial f_L}{\partial \tilde{\eta}_0} - q_0 = 0, && (3.1.10)\\
&(\text{KKT II}) && q_i \geq 0, && (3.1.11)\\
&(\text{KKT III}) && \tilde{\eta}_{i+1} - \tilde{\eta}_i \leq 0, \text{ and} && (3.1.12)\\
&(\text{KKT IV}) && q_i(\tilde{\eta}_{i+1} - \tilde{\eta}_i) = 0, \text{ or equivalently,} && \\
& && q_i(\tilde{\eta}_{i+1} - \tilde{\eta}_i)/\Delta v = 0 \text{ (no summation imposed).} && (3.1.13)
\end{aligned}$$

Choosing $\vec{\tilde{\eta}}$ to be a unit vector $\hat{\tilde{\eta}}_i$ along the ith component $\tilde{\eta}_i$, the first term on the left-hand side of (3.1.9) and (3.1.10) can be written as

$$\frac{\partial}{\partial \tilde{\eta}_i} f_L(\vec{\tilde{\eta}}) = \hat{\tilde{\eta}}_i \cdot \frac{\partial}{\partial \vec{\tilde{\eta}}} f_L(\vec{\tilde{\eta}}) = \lim_{\epsilon \to 0} \frac{f_L(\vec{\tilde{\eta}} + \epsilon \hat{\tilde{\eta}}_i) - f_L(\vec{\tilde{\eta}})}{\epsilon}. \tag{3.1.14}$$

Using (3.1.14), we now have

$$\frac{\partial}{\partial \tilde{\eta}_i} f_L(\vec{\tilde{\eta}}) = \lim_{\epsilon \to 0} \frac{L[\tilde{\eta}(v_{\min}; \vec{\tilde{\eta}} + \epsilon \hat{\tilde{\eta}}_i)] - L[\tilde{\eta}(v_{\min}; \vec{\tilde{\eta}})]}{\epsilon}. \tag{3.1.15}$$

Using $L[\tilde{\eta}(v_{\min}; \vec{\tilde{\eta}} + \epsilon \hat{\tilde{\eta}}_i)] = L[\tilde{\eta}(v_{\min}; \vec{\tilde{\eta}}) + \epsilon \tilde{\eta}(v_{\min}; \hat{\tilde{\eta}}_i)]$, (3.1.15) can be written in terms of the functional derivative of the L functional,

$$\frac{\partial}{\partial\tilde{\eta}_i} f_L(\vec{\tilde{\eta}}) = \lim_{\epsilon\to 0} \frac{L[\tilde{\eta}(v_{\min};\vec{\tilde{\eta}}) + \epsilon\tilde{\eta}(v_{\min};\hat{\tilde{\eta}}_i)] - L[\tilde{\eta}(v_{\min};\vec{\tilde{\eta}})]}{\epsilon} \tag{3.1.16}$$

$$= \int_0^\infty \mathrm{d}v_{\min}\ \tilde{\eta}(v_{\min};\hat{\tilde{\eta}}_i)\frac{\delta L}{\delta\tilde{\eta}(v_{\min})}. \tag{3.1.17}$$

From (3.1.6) one can easily see that the function $\tilde{\eta}(v_{\min};\hat{\tilde{\eta}}_i)$ in (3.1.17) has a rectangular shape with value 1 between $v^i_{\min}$ and $v^{i+1}_{\min}$ and zero everywhere else. The summation over i from $i = 0$ to $j \leq K-1$ of the left-hand side of (3.1.9) and (3.1.10) is thus

$$\frac{\partial f_L}{\partial\tilde{\eta}_0} - q_0 + \sum_{i=1}^{j}\left(\frac{\partial f_L}{\partial\tilde{\eta}_i} + q_{i-1} - q_i\right) = \sum_{i=0}^{j}\frac{\partial f_L}{\partial\tilde{\eta}_i} - q_j \tag{3.1.18}$$

$$= \sum_{i=0}^{j}\int_0^\infty \mathrm{d}v_{\min}\ \tilde{\eta}(v_{\min};\hat{\tilde{\eta}}_i)\frac{\delta L}{\delta\tilde{\eta}(v_{\min})} - q_j. \tag{3.1.19}$$

Note that in the integrand (3.1.19) $\sum_{i=0}^{j}\tilde{\eta}(v_{\min};\hat{\tilde{\eta}}_i) = \theta(v^j_{\min} - v_{\min})\theta(v_{\min} - v_\delta)$, thus

$$\sum_{i=0}^{j}\int_0^\infty \mathrm{d}v_{\min}\ \tilde{\eta}(v_{\min};\hat{\tilde{\eta}}_i)\frac{\delta L}{\delta\tilde{\eta}(v_{\min})} - q_j = \int_{v_\delta}^{v^j_{\min}} \mathrm{d}v_{\min}\ \frac{\delta L}{\delta\tilde{\eta}(v_{\min})} - q_j. \tag{3.1.20}$$

Using an interpolation function $q(v_{\min})$ satisfying $q(v^j_{\min}) = q_j$, we finally conclude, using (3.1.20), that the KKT I conditions (3.1.9) and (3.1.10) imply

$$\int_{v_\delta}^{v^j_{\min}} \mathrm{d}v\ \frac{\delta L}{\delta\tilde{\eta}(v)} - q(v^j_{\min}) = 0. \tag{3.1.21}$$

By taking a large enough K with v^{MAX} fixed, we can find an integer j such that $v^j_{\min}$ is arbitrarily close to a given $v_{\min}$ value, if $v_\delta \leq v_{\min} \leq v^{\mathrm{MAX}}$. Therefore, in the limit $K \to \infty$, and thus $\Delta v \to 0$, we can write the conditions (3.1.21) and (3.1.11) to (3.1.13) for continuous $v_{\min}$ and $\tilde{\eta}$ variables:

$$\text{(I)} \qquad q(v_{\min}) = \int_{v_\delta}^{v_{\min}} \mathrm{d}v\ \frac{\delta L}{\delta\tilde{\eta}(v)}, \tag{3.1.22}$$

$$\text{(II)} \qquad q(v_{\min}) \geq 0, \tag{3.1.23}$$

$$\text{(III)} \qquad \forall\epsilon > 0, \quad \tilde{\eta}(v_{\min}+\epsilon) \leq \tilde{\eta}(v_{\min}), \text{ and} \tag{3.1.24}$$

$$\text{(IV)} \qquad q(v_{\min})\ \lim_{\epsilon->0}\frac{\tilde{\eta}(v_{\min}+\epsilon) - \tilde{\eta}(v_{\min})}{\epsilon} = 0. \tag{3.1.25}$$

Note that although we write the conditions in terms of continuous variables, they should always be understood as a limit of the conditions for discrete variables.

Two direct consequences of (IV) (3.1.25) are: i) $\tilde{\eta}(v_{\rm min})$ can be discontinuous only at the points where $q(v_{\rm min})$ vanishes, and ii) $\tilde{\eta}(v_{\rm min})$ is constant in an open interval where $q(v_{\rm min}) \neq 0$. If there is an open interval where $q(v_{\rm min})$ is zero, within the interval, (IV) is trivially satisfied. Therefore, $\tilde{\eta}(v_{\rm min})$ is a piecewise constant function with discontinuity points where $q(v_{\rm min}) = 0$. Let us examine the possible zeros of the $q(v_{\rm min})$ function.

Using (3.1.1) and (3.1.5) in (I) (3.1.22), we get

$$q(v_{\rm min}) = 2\int_{v_\delta}^{v_{\rm min}} {\rm d}v \, \frac{\delta N_E}{\delta\tilde{\eta}(v)} - 2\int_{v_\delta}^{v_{\rm min}} {\rm d}v \, \sum_{i=a}^{N_O} \frac{\delta}{\delta\tilde{\eta}(v)} \ln\left(\left.\frac{{\rm d}R_{tot}}{{\rm d}E'}\right|_{E'=E'_a} \right). \quad (3.1.26)$$

In (3.1.2) N_E is given in terms of $\mathcal{R}$, given in turn in (1.3.14), where $d\mathcal{R}/dE'$ is in (1.3.10). Using these equations, (3.1.26) becomes

$$\begin{aligned} q(v_{\rm min}) = 2MT \int_{E'_{\rm min}}^{E'_{\rm max}} {\rm d}E' \, \frac{{\rm d}\mathcal{H}}{{\rm d}E'}(E', v_{\rm min}) \\ -2\sum_{a=1}^{N_O} \left[\int_{v_\delta}^{v_{\rm min}} {\rm d}v \, \left(\frac{\delta}{\delta\tilde{\eta}(v)} \frac{{\rm d}R_{tot}}{{\rm d}E'} \right) \right]_{E'=E'_a} \Bigg/ \left[\frac{{\rm d}R_{tot}}{{\rm d}E'} \right]_{E'=E'_a} \end{aligned} \quad (3.1.27)$$

We define:

$$\xi(v_{\rm min}) \equiv MT \int_{E'_{\rm min}}^{E'_{\rm max}} {\rm d}E' \, \frac{{\rm d}\mathcal{H}}{{\rm d}E'}(E', v_{\rm min}). \quad (3.1.28)$$

Using (3.1.4) and (1.3.10), we can write

$$\begin{aligned} \int_{v_\delta}^{v_{\rm min}} {\rm d}v \, \left.\left(\frac{\delta}{\delta\tilde{\eta}(v)} \frac{{\rm d}R_{tot}}{{\rm d}E'} \right)\right|_{E'=E'_a} &= \int_{v_\delta}^{v_{\rm min}} {\rm d}v \, \left.\left(\frac{{\rm d}\mathcal{R}}{{\rm d}E'} \right)\right|_{E'=E'_a} \\ &= \left.\frac{{\rm d}\mathcal{H}}{{\rm d}E'}(E', v_{\rm min})\right|_{E'=E'_a} \equiv H_a(v_{\rm min}) \end{aligned} \quad (3.1.29)$$

and

$$\gamma_a[\tilde{\eta}] \equiv \left.\frac{{\rm d}R_{tot}}{{\rm d}E'}\right|_{E'=E'_a}. \quad (3.1.30)$$

Replacing (3.1.28) to (3.1.30) into (3.1.27), we obtain

$$q(v_{\rm min}) \equiv 2\xi(v_{\rm min}) - 2\sum_{a=1}^{N_O} \frac{H_a(v_{\rm min})}{\gamma_a[\tilde{\eta}]}. \quad (3.1.31)$$

In this equation, the only $\tilde{\eta}$ dependence is in $\gamma_a[\tilde{\eta}]$. The functions $\xi(v_{\min})$ and $H_a(v_{\min})$ do not depend on $\tilde{\eta}$.

Fig. 3.1 shows the functions $H_a(v_{\min})$ and $\xi(v_{\min})$ for the three candidate events of CDMS-II-Si assuming an SI cross section with $f_n/f_p = 1$ and $m = 9$ GeV. In order to explain the form of these functions, let us first consider a simple situation where the target material consists of a single nuclide, or multiple isotopes of the same element, as in CDMS-II-Si. In this case, the integrands of the different terms $\mathrm{d}\mathcal{H}_T/\mathrm{d}E'$ in (1.3.4) contributing to $\mathrm{d}\mathcal{H}/\mathrm{d}E'$ in (1.3.3) are similarly localized in E_R for all nuclides T (for a fixed E'). Notice that these integrands are independent of v if $d\sigma_T/dE_R$ is proportional to v^{-2}. In this case, the v dependence of $\mathrm{d}\mathcal{H}_T/\mathrm{d}E'$ is only in the integration range $[E_R^{T-}(v), E_R^{T+}(v)]$. If so, as v increases, this range covers more of the region in which the integrand is non-zero. Thus, $\mathrm{d}\mathcal{H}/\mathrm{d}E'$ grows with v in a certain range. When v is large enough for the integration in (1.3.4) to cover all the region in which the integrand is non-zero, $\mathrm{d}\mathcal{H}_T/\mathrm{d}E'$ becomes constant, and so does $\mathrm{d}\mathcal{H}/\mathrm{d}E'$. This explains the step-like functional form of $H_a(v_{\min})$ given in (3.1.29), which is $\mathrm{d}\mathcal{H}/\mathrm{d}E'$ with $E' = E_a$, as can be seen in the left panel of Fig. 3.1.

Looking at (1.3.4) which defines $\mathrm{d}\mathcal{H}_T/\mathrm{d}E'$ for each nuclide T, we see that the only dependence on E' of the integrand is in $\epsilon(E_R, E')G_T(E_R, E')$. To compute $\xi(v_{\min})$, we need thus a double integration, first in E_R to obtain $\mathrm{d}\mathcal{H}_T/\mathrm{d}E'$, and then in E', after summing all $\mathrm{d}\mathcal{H}_T/\mathrm{d}E'$ contributing to $\mathrm{d}\mathcal{H}/\mathrm{d}E'$. If we exchange the order of integration, performing the E' integration first, we see that as E_R increases, for E_R very small the integrand ϵG_T will be zero within the E' integration range. Then, the non-zero portion of ϵG_T within the E' integration range will increase, then be entirely contained, and then decrease and become zero again. Thus, the resulting integrand in E_R will be slowly changing in the E_R range in which it is non-zero. As $v_{\min}$ increases, the integration range in E_R encompasses more of the slowly varying integrand, resulting in a smoothly increasing function $\xi(v_{\min})$, as shown in the right panel of Fig. 3.1. Once $v_{\min}$ becomes large enough for the integration range in E_R to cover all the non-zero part of the integrand in $\xi(v_{\min})$, this function becomes constant (see Fig. 3.1).

Let us return to study the discontinuity points of the best-fit $\tilde{\eta}$ function which happen at the zeros of $q(v_{\min})$ given in (3.1.31). For elastic ($\delta = 0$) or endothermic ($\delta > 0$) scattering, there is a region at small $v_{\min}$ values where both H_a and ξ vanish. Looking at (1.3.4), when

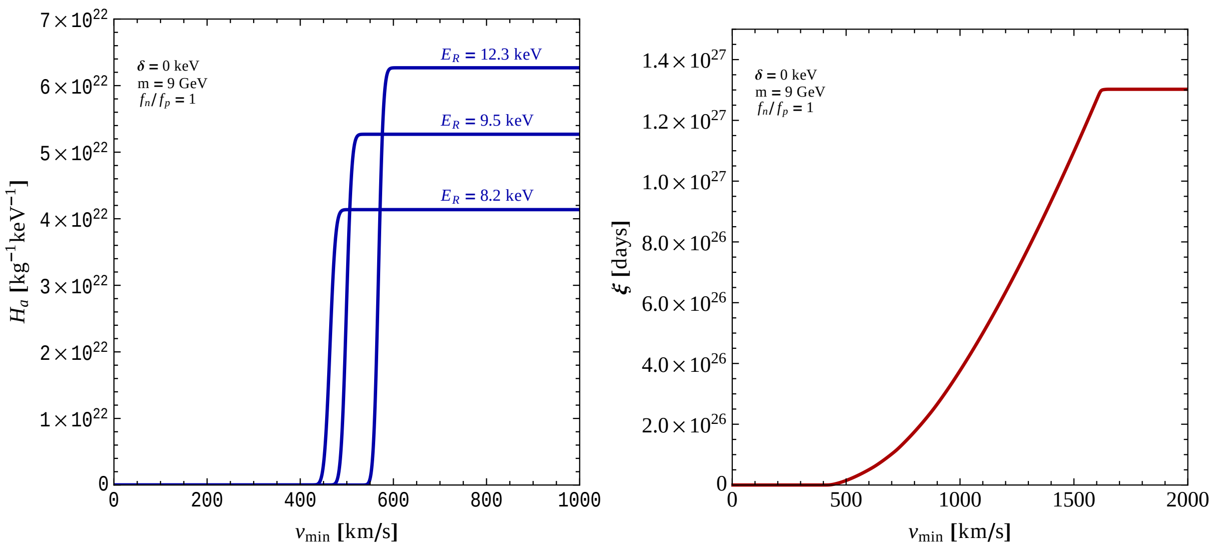

Figure 3.1. $H_a(v_{\min})$ (left panel) and $\xi(v_{\min})$ (right panel) for elastic isospin-conserving SI interactions and $m = 9$ GeV, for the three events of CDMS-II-Si.

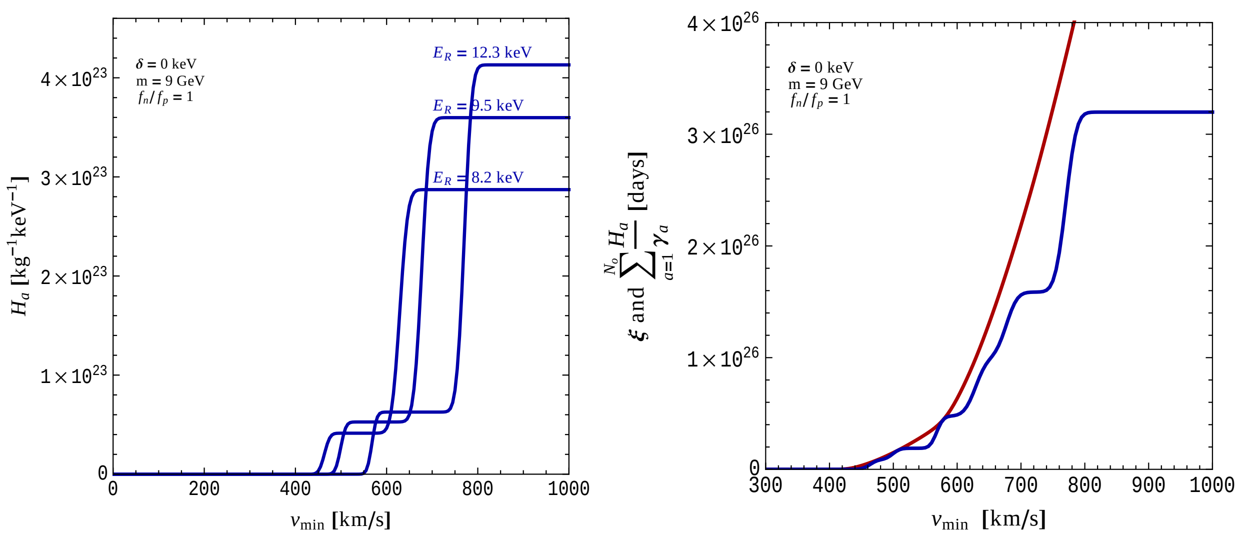

Figure 3.2. Same as Fig. 3.1 but for a fictitious detector with target material composed of equal mass fractions of Si and Ge (see the text), and showing in addition $\sum_a H_a(v_{\min})/\gamma_a$ (blue line, right panel) .

$E_R^{T+}(v)$ is below the experimental threshold, the integrand, in particular the acceptance ϵ, is zero, thus $\mathrm{d}\mathcal{H}/dE' = 0$. In this $v_{\min}$ region the condition $q(v_{\min}) = 0$ is trivially satisfied, and the shape of the best-fit $\tilde{\eta}$ function is undetermined.

Changes in $\tilde{\eta}(v_{\min})$ produce changes in $\gamma_a[\tilde{\eta}]$. For values of γ_a which make the second term of the right hand side of (3.30) large enough to reach the first term $2\xi(v_{\min})$ from below, $q(v_{\min})$ (see (3.1.31)) has non-trivial zeros where ξ and H_a are non-zero. The non-negativity of $q(v) \geq 0$ means that $q(v) = 0$ only when the monotonically increasing function ξ touches the step-like $\sum_a H_a/\gamma_a$ function from above. Since $\sum_a H_a/\gamma_a$ has N_O steps, this can happen only at a number of $v_{\rm min}$ values smaller than or equal to N_O. Examples of these functions ξ, $\sum_a H_a/\gamma_a$, and q will be shown below in Figs. 3.5, 3.7 and 3.8.

To guess the generic shape of the $\xi(v_{\rm min})$ and $H_a(v_{\rm min})$ functions for differential cross sections whose WIMP speed v dependence is different from $\propto v^{-2}$, let us assume the differential cross section for a given E_R behaves as $v^{(n-2)}$ for large values of v. One such example is that of WIMPs interacting with nuclei through a magnetic dipole moment, where $n = 2$ at large v (see (3.9) of [52]). In this case, from (1.3.4) one can easily see that the shapes of the functions $H_a(v)/v^n$ and $\xi(v)/v^n$ should be similar to those of $H_a(v)$ and $\xi(v)$ for a differential cross section proportional to v^{-2}. Therefore, the argument given above can be used for $q(v)/v^n$, whose zeros are the same as those of $q(v)$, leading to the same conclusions.

When the target consists of several elements, each H_a has multiple step-like features, one for each element. This is illustrated in Fig. 3.2 for a fictitious CDMS-II-like detector composed of equal mass fractions of Si and Ge. We see in the left panel of Fig. 3.2 that for each of the three elements there are two step-like features in H_a. One may naively expect that because in this case there are $2N_O$ step-like features in $\sum_a H_a/\gamma_a$, the number of zeros of the function $q(v_{\rm min})$ would equally double. However, this is not the case. Because ξ and H_a are independent of $\tilde{\eta}$, by changing $\tilde{\eta}$ and thus γ_a in general one can make at most one of the two steps per observed event in $\sum_a H_a/\gamma_a$ touch the function $\xi(v_{\rm min})$ from below. Thus the number of zeros of $q(v_{\rm min})$ is still at most N_O. This can be seen in the right panel of Fig. 3.2.

In summary, in this section we proved that the $\tilde{\eta}$ function maximizing the extended likelihood is a piecewise constant function with a number of steps smaller than or equal to the number N_O of observed events.

3.2 EHI analysis in the $v_{\rm min}$-space

In this section we show how to find the solution to the maximization of the extended likelihood in the EHI method, in the $v_{\rm min}$–$\tilde{\eta}$ space. As shown in the previous section, the best-fit function, which we call $\tilde{\eta}_{\rm BF}(v_{\rm min})$ from now on, is a piecewise constant function with at most N_O steps (note that in the statistics literature the subscript "ML" for maximum likelihood is usually used instead of "BF"). We will also find a statistically meaningful confidence band around $\tilde{\eta}_{\rm BF}(v_{\rm min})$, which we will define as a pointwise confidence band.

3.2.1 Finding the best-fit function $\tilde{\eta}_{\rm BF}(v_{\rm min})$

The properties of the $\tilde{\eta}$ function maximizing the extended likelihood we have proven in the previous section can be utilized to find $\tilde{\eta}_{\rm BF}$. We can define a function $f_L^{(N_O)}$ of $2N_O$ variables, $\vec{v} = (v_1, v_2, \ldots, v_{N_O})$ and $\vec{\tilde{\eta}} = (\tilde{\eta}_1, \tilde{\eta}_2, \ldots, \tilde{\eta}_{N_O})$, specifying the positions and heights of the N_O steps, as a restriction of the functional $L[\tilde{\eta}]$:

$$f_L^{(N_O)}(\vec{v}, \vec{\tilde{\eta}}) \equiv L[\tilde{\eta}^{(N_O)}(v_{\rm min}; \vec{v}, \vec{\tilde{\eta}})]. \tag{3.2.1}$$

The piecewise constant function $\tilde{\eta}^{(N_O)}$ is defined as

$$\tilde{\eta}^{(N_O)}(v_{\rm min}; \vec{v}, \vec{\tilde{\eta}}) \equiv \begin{cases} \tilde{\eta}_a & \text{if } v_{a-1} < v_{\rm min} \leq v_a, \\ 0 & \text{if } v_{N_O} < v_{\rm min}, \end{cases} \tag{3.2.2}$$

where $a = 1, \ldots, N_O$. Here we assume $v_{\rm min}$ and v_a's are all larger than v_δ, and the constraints (3.1.24) $\tilde{\eta}_a \leq \tilde{\eta}_b$ for $a > b$ are satisfied. Since the function $\tilde{\eta}$ cannot change after the last step and it must reach zero for large $v_{\rm min}$, it must be zero for $v_{\rm min} > v_{N_O}$. We do not specify the value of $\tilde{\eta}^{(N_O)}$ below the minimum v_δ since the event rate is independent of it. Notice that (3.2.2) requires the definition of v_0. We define $v_0 = v_\delta$ for convenience.

From these definitions and the theorem we have proven, we can easily obtain $\tilde{\eta}_{\rm BF}$ and $L_{\rm min}$, the minimum value of the functional $L[\tilde{\eta}]$, by finding $\vec{v}_{\rm BF}$ and $\vec{\tilde{\eta}}_{\rm BF}$ that minimize $f_L^{(N_O)}$, so that

$$\tilde{\eta}_{\rm BF}(v_{\rm min}) = \tilde{\eta}^{(N_O)}(v_{\rm min}; \vec{v}_{\rm BF}, \vec{\tilde{\eta}}_{\rm BF}) \tag{3.2.3}$$

and

$$L_{\rm min} \equiv L[\tilde{\eta}_{\rm BF}(v_{\rm min})] = L[\tilde{\eta}^{(N_O)}(v_{\rm min}; \vec{v}_{\rm BF}, \vec{\tilde{\eta}}_{\rm BF})]. \tag{3.2.4}$$

From the definition (3.1.1) of the extended likelihood function, we can write $f_L^{(N_O)}$ in a simple form as

$$f_L^{(N_O)} = 2N_{BG} + 2MT \sum_{a=1}^{N_O} \tilde{\eta}_a \int_{v_{a-1}}^{v_a} \mathrm{d}v_{\min} \mathcal{R}_{[E'_{\min}, E'_{\max}]}(v_{\min})$$
$$-2 \sum_{i=1}^{N_O} \ln \left[MT \sum_{a=1}^{N_O} \tilde{\eta}_a \int_{v_{a-1}}^{v_a} \mathrm{d}v_{\min} \frac{\mathrm{d}\mathcal{R}}{\mathrm{d}E'}(v_{\min}) + MT \frac{dR_{\mathrm{BG}}}{\mathrm{d}E'}(v_{\min}) \right]_{E'=E'_i}, \quad (3.2.5)$$

with N_{BG} given in (3.1.3). Defining the $\mathcal{N}_a$ and $\mathcal{M}_{ai}$ functions of v_a as

$$\mathcal{N}_a(\vec{v}) \equiv MT \int_{v_{a-1}}^{v_a} \mathrm{d}v_{\min} \mathcal{R}_{[E'_{\min}, E'_{\max}]}(v_{\min}), \quad (3.2.6)$$
$$\mathcal{M}_{ai}(\vec{v}) \equiv MT \int_{v_{a-1}}^{v_a} \mathrm{d}v_{\min} \left. \frac{\mathrm{d}\mathcal{R}}{\mathrm{d}E'} \right|_{E'=E'_i} (v_{\min}), \quad (3.2.7)$$

and the fixed constants b_i

$$b_i \equiv MT \left. \frac{\mathrm{d}R_{\mathrm{BG}}}{\mathrm{d}E'} \right|_{E'=E'_i}, \quad (3.2.8)$$

we can write (3.2.5) as

$$f_L^{(N_O)} = 2N_{\mathrm{BG}} + 2 \sum_{a=1}^{N_O} \tilde{\eta}_a \mathcal{N}_a - 2 \sum_{i=1}^{N_O} \ln \left[\sum_{a=1}^{N_O} \tilde{\eta}_a \mathcal{M}_{ai} + b_i \right]. \quad (3.2.9)$$

The minimization of the function $f_L^{(N_O)}$ of $2N_O$ parameters $v_1, \ldots, v_{N_O}$, $\tilde{\eta}_1, \ldots, \tilde{\eta}_{N_O}$, subject to the constraints

$$v_1 > v_\delta, \quad (3.2.10)$$
$$v_b - v_a \geq 0 \text{ and } \tilde{\eta}_a - \tilde{\eta}_b \geq 0 \text{ for } a < b, \quad (3.2.11)$$

can be done numerically using a global minimization algorithm. In the implementation, we express $f_L^{(N_O)}$ in terms of $\ln \tilde{\eta}_a$ and use $\ln \tilde{\eta}_a$ instead of $\tilde{\eta}_a$ as variables, since $\tilde{\eta}_a$ span many orders of magnitude. This also accounts for the $\tilde{\eta}_a > 0$ constraints, leaving only the constraints in (3.2.10) and (3.2.11) to be enforced in the minimization. Note that in general minimization algorithms may attempt to evaluate the function in regions where the constraints are not satisfied, and in these regions the function $f_L^{(N_O)}$ is not well defined, thus a fictitious function must be used that grows smoothly with the absolute value of the unsatisfied constraints in (3.2.10) and (3.2.11).

3.2.2 Finding the confidence band

In order to compare the $\tilde{\eta}_{\rm BF}$ we obtained with the upper limits imposed by other experiments, we need a way to represent the uncertainty in our determination of $\tilde{\eta}_{\rm BF}$. This can be achieved by finding a region in the $v_{\rm min}$–$\tilde{\eta}$ space satisfying a certain statistical criterion, analogous to the confidence interval in the usual analysis with a fixed halo model. The region in the $v_{\rm min}$–$\tilde{\eta}$ space which is densely filled by the family of all possible $\tilde{\eta}(v_{\rm min})$ curves satisfying

$$\Delta L[\tilde{\eta}] \equiv L[\tilde{\eta}] - L_{\rm min} \leq \Delta L^*, \tag{3.2.12}$$

with given ΔL^*, is a natural candidate to examine. The condition in (3.2.12) defines a two-sided interval around $\tilde{\eta}_{\rm BF}$ for each $v_{\rm min}$ value, and the collection of those intervals forms a pointwise confidence band in $v_{\rm min}$–$\tilde{\eta}$ space. From now on we will call it simply "the confidence band".

Conceptually, computing the confidence band is a straightforward procedure, but in practice, finding all the $\tilde{\eta}$ functions satisfying (3.2.12) and constructing the band from them is not possible. If the same band can be formed by a much smaller subset of them, and this subset is much easier to find than the whole set, the construction of the band would be practical.

As a possible subset, let us consider the set of $\tilde{\eta}$ functions which minimize $L[\tilde{\eta}]$ subject to the constraint

$$\tilde{\eta}(v^*) = \tilde{\eta}^*. \tag{3.2.13}$$

Let us define $L^c_{\rm min}(v^*, \tilde{\eta}^*)$ to be the minimum of the $L[\tilde{\eta}]$ subject to the constraint (3.2.13), and

$$\Delta L^c_{\rm min}(v^*, \tilde{\eta}^*) = L^c_{\rm min}(v^*, \tilde{\eta}^*) - L_{\rm min}. \tag{3.2.14}$$

If $\Delta L^c_{\rm min}(v^*, \tilde{\eta}^*)$ is larger than a chosen ΔL^*, it simply means that the point $(v^*, \tilde{\eta}^*)$ lies outside of the confidence band. If it were inside the band, there should be at least one $\tilde{\eta}$ function passing through the $(v^*, \tilde{\eta}^*)$ point, for which $\Delta L[\tilde{\eta}] \leq \Delta L^*$, in contradiction with the fact that $\Delta L^c_{\rm min}(v^*, \tilde{\eta}^*) > \Delta L^*$. On the other hand, if $\Delta L^c_{\rm min}(v^*, \tilde{\eta}^*) \leq \Delta L^*$, the confidence band should cover the point $(v^*, \tilde{\eta}^*)$ by definition. Therefore, by finding the range of $\tilde{\eta}^*$

values which satisfy $\Delta L^c_{\rm min}(v^*, \tilde{\eta}^*) \leq \Delta L^*$ for each v^* value, we can construct the band.

The remaining problem is how to find an easy way of computing $L^c_{\rm min}(v^*, \tilde{\eta}^*)$ (and therefore $\Delta L^c_{\rm min}(v^*, \tilde{\eta}^*)$). We will now prove that the $\tilde{\eta}$ function minimizing $L[\tilde{\eta}]$ subject to the constraint (3.2.13) should be a piecewise constant function with at most $N_O + 1$ discontinuities.

Let us rewrite the KKT conditions in (3.1.9)-(3.1.13) but now with an additional equality constraint

$$\tilde{\eta}_k = \tilde{\eta}^*, \tag{3.2.15}$$

where the index k is chosen to satisfy $v^k_{\rm min} \leq v^* < v^{k+1}_{\rm min}$, so that $v^k_{\rm min}$ can be arbitrarily close to v^* for large enough K values. The additional constraint leads to the necessity of adding the term $p^*(\tilde{\eta}_k - \tilde{\eta}^*)$ to the function f'_L in (3.1.8) introducing a Lagrange multiplier p^*, so we define another function $f''_L(\vec{\tilde{\eta}}, \vec{q}, p^*)$ as

$$\begin{aligned} f''_L(\vec{\tilde{\eta}}, \vec{q}, p^*) &\equiv f'_L(\vec{\tilde{\eta}}, \vec{q}) + p^*(\tilde{\eta}_k - \tilde{\eta}^*) && (3.2.16)\\ &= L[\tilde{\eta}(v_{\rm min}; \vec{\tilde{\eta}})] + \sum_{i=0}^{K-1} q_i(\tilde{\eta}_{i+1} - \tilde{\eta}_i) + p^*(\tilde{\eta}_k - \tilde{\eta}^*), && (3.2.17) \end{aligned}$$

and use it to derive new KKT conditions.

The new KKT conditions consist of the unconstrained minimization conditions of the function $f''_L(\vec{\tilde{\eta}}, \vec{q}, p^*)$ with respect to the parameters $\vec{\tilde{\eta}}$, $\vec{q}$ and p^*, plus the complementary conditions, which are the same as before. Therefore, besides the constraint (3.2.15), the changes only appear in the (KKT I)$_{\rm a}$ and (KKT I)$_{\rm b}$ conditions, where the function f'_L was present. The new conditions are

$$\text{(KKT I)}'_{\rm a} \qquad \frac{\partial f_L}{\partial \tilde{\eta}_i} + q_{i-1} - q_i + p^* \delta_{ki} = 0, \text{ for } 1 \leq i \leq K-1, \text{ and} \tag{3.2.18}$$

$$\text{(KKT I)}'_{\rm b} \qquad \frac{\partial f_L}{\partial \tilde{\eta}_0} - q_0 + p^* \delta_{k0} = 0 \tag{3.2.19}$$

with additional terms $p^* \delta_{ki}$ and $p^* \delta_{k0}$, respectively, and the constraint (3.2.15). Following similar steps as those in Sec. 3.1 from (3.1.14) to (3.1.21), the summation of (3.2.18) and

(3.2.19) over i from 0 to j now becomes

$$\int_{v_\delta}^{v^j_{\rm min}} {\rm d}v \ \frac{\delta L}{\delta\tilde{\eta}(v)} - q(v^j_{\rm min}) + p^*\theta(v^j_{\rm min} - v^k) = 0. \tag{3.2.20}$$

In the limit of $K \to \infty$, the first condition for the $\tilde{\eta}$ functions minimizing $L[\tilde{\eta}]$ subject to the constraint (3.2.13) becomes

$$({\rm I})' \qquad q(v_{\rm min}) = \int_{v_\delta}^{v_{\rm min}} {\rm d}v \ \frac{\delta L}{\delta\tilde{\eta}(v)} + p^*\theta(v_{\rm min} - v^*), \tag{3.2.21}$$

while the conditions (II), (III) and (IV) are the same as in (3.1.23)-(3.1.25).

Using the definition of $L[\tilde{\eta}]$ in (3.1.5) and (3.1.1) in the condition (3.2.21), we can write the function $q(v_{\rm min})$ as

$$q(v_{\rm min}) = 2\xi(v_{\rm min}) - 2\sum_{a=1}^{N_O} \frac{H_a(v_{\rm min})}{\gamma_a[\tilde{\eta}]} + p^*\theta(v_{\rm min} - v^*), \tag{3.2.22}$$

with $\xi(v_{\rm min})$, $H_a(v_{\rm min})$ and $\gamma_a[\tilde{\eta}]$ defined in (3.1.28), (3.1.29) and (3.1.30), respectively.

Again, the conditions in (3.2.21) and (3.1.25) tell that the $\tilde{\eta}$ function we find is piecewise constant with discontinuities only at the isolated zeros of $q(v_{\rm min})$. We already argued that $\xi(v_{\rm min})$ can touch the function $\sum_{a=1}^{N_O} H_a/\gamma_a$ from above at a number of points equal to or less than the number of observed events N_O. Since $p^*\theta(v_{\rm min} - v^*)$ introduces another step on the right hand side of (3.2.22), with the right p^* value $q(v_{\rm min})$ could have an additional zero. Thus the $\tilde{\eta}(v_{\rm min})$ function minimizing $L[\tilde{\eta}]$ subject to the constraint (3.2.13) is piecewise constant with at most $N_O + 1$ discontinuities.

Using a function $\tilde{\eta}$ of this type in (3.2.12) for each (v^*, η^*), we minimize $L[\tilde{\eta}]$ in (3.1.5) as in Sec. 3.2.1 to compute $\Delta L^c_{\rm min}(v^*, \tilde{\eta}^*)$ in (3.2.14). We define a function $f_L^{(N_O+1)}(\vec{v}, \vec{\tilde{\eta}})$ as in (3.2.1), parametrized by $\vec{v} = (v_1, v_2, \dots, v_i = v^*, \dots, v_{N_O+1})$ and $\vec{\tilde{\eta}} = (\tilde{\eta}_1, \tilde{\eta}_2, \dots, \tilde{\eta}_i = \tilde{\eta}^*, \dots, \tilde{\eta}_{N_O+1})$. The minimization of $f_L^{(N_O+1)}$ can again be done numerically using a global minimization algorithm, subject to the same constraints as in (3.2.10)-(3.2.11), where in addition we keep $(v_i, \tilde{\eta}_i)$ fixed at $(v^*, \tilde{\eta}^*)$. As before, in our implementation of the algorithm we write $f_L^{(N_O+1)}$ in terms of $\ln\tilde{\eta}_a$ instead of $\tilde{\eta}_a$. We repeat the minimization procedure for all indices $i = 1 \dots (N_O+1)$ corresponding to the position of the $(v^*, \tilde{\eta}^*)$ step in $\tilde{\eta}$, and select the solution that gives the overall minimum of $f_L^{(N_O+1)}$.

3.2.3 Statistical interpretation of the confidence band

From the procedure described above we can get both the best-fit $\tilde{\eta}$ function, $\tilde{\eta}_{\rm BF}(v_{\rm min})$, and the confidence band. For a quantitative assessment of the compatibility with other experimental data, we need to know the statistical meaning of a particular choice for ΔL^*. One may be tempted to interpret ΔL as -2 times the logarithm of the likelihood ratio with $2N_O$ parameters, since we parametrized the $\tilde{\eta}$ function with $2N_O$ parameters (plus v^* and $\tilde{\eta}^*$ which are fixed each time) to obtain the confidence band. However, this is not the proper interpretation. Note that the defining properties of the best-fit $\tilde{\eta}_{\rm BF}$ and the band do not rely on how we compute them.

Let us return to the definition of $\Delta L^c_{\rm min}(v^*, \tilde{\eta})$ and use again the discretization procedure introduced to derive the KKT conditions in Sec. 3.1. With a discretization of $v_{\rm min}$ we can define a likelihood function

$$\mathcal{L}(\tilde{\eta}_0, \ldots, \tilde{\eta}_{K-1}) = \mathcal{L}[\tilde{\eta}(v_{\rm min}; \vec{\tilde{\eta}})] \tag{3.2.23}$$

with $\tilde{\eta}(v_{\rm min}; \vec{\tilde{\eta}})$ defined in (3.1.6). With this discretization, $\Delta L^c_{\rm min}(v^*, \tilde{\eta})$ defined in (3.2.14) is replaced by a collection of functions $\Delta L^{c,k}_{\rm min}(\tilde{\eta}^*)$ each having v^* in the k-interval $v^k_{\rm min} \leq v^* < v^{k+1}_{\rm min}$, so that $\tilde{\eta}_k = \eta^*$,

$$\Delta L^{c,k}_{\rm min}(\tilde{\eta}^*) = -2 \ln \left[\frac{\mathcal{L}(\hat{\hat{\tilde{\eta}}}_0, \ldots, \hat{\hat{\tilde{\eta}}}_{k-1}, \tilde{\eta}_k = \tilde{\eta}^*, \hat{\hat{\tilde{\eta}}}_{k+1}, \ldots, \hat{\hat{\tilde{\eta}}}_{K-1})}{\mathcal{L}(\hat{\tilde{\eta}}_0, \ldots, \hat{\tilde{\eta}}_k, \ldots, \hat{\tilde{\eta}}_{K-1})} \right] . \tag{3.2.24}$$

Here the $\hat{\hat{\tilde{\eta}}}_i$ values maximize the function $\mathcal{L}$ subject to the constraint $\tilde{\eta}_k = \tilde{\eta}^*$, while $\hat{\tilde{\eta}}_i$ maximize the function $\mathcal{L}$ without the constraint. Thus $\Delta L^{c,k}_{\rm min}$ is $-2 \ln$ of the profile likelihood ratio (see e.g. equation (38.53) of [81]) with only one parameter $\tilde{\eta}_k = \tilde{\eta}^*$. Notice that the continuous parameter v^* becomes the discrete index k, and is no longer an additional parameter. According to Wilks' theorem, the distribution of $\Delta L^{c,k}_{\rm min}$ approaches a chi-square distribution with one degree of freedom, in the limit where the data sample is very large [81, 82] (and this is independent of the value of K). In short, this amounts to profiling the likelihood at fixed v^* over the nuisance parameters $\tilde{\eta}_0, \ldots, \tilde{\eta}_{k-1}, \tilde{\eta}_{k+1}, \ldots, \tilde{\eta}_K$. In this language, the fact that the likelihood ratio in (3.2.24) has one degree of freedom is proven mathematically in corollary 2 of [83] even for the case $K \to \infty$.

By taking large enough K, we can make $v^k_{\rm min}$ and $v^{k+1}_{\rm min}$ arbitrarily close to v^*, and for each v^*, $\Delta L^{c,k}_{\rm min}(\tilde{\eta}^*)$ approaches $\Delta L^c_{\rm min}(v^*, \tilde{\eta}^*)$. Therefore, the natural interpretation of the band is the collection of the confidence intervals in $\tilde{\eta}$ for each $v_{\rm min}$ value, which defines a pointwise confidence band, based on a profile likelihood ratio with one degree of freedom. With this interpretation, we can now compare the confidence band with other limits or measurements in a statistically meaningful way. If any upper limit at some CL crosses the lower boundary of the band, at some other CL, it means that the two data, providing the limit and the band, are incompatible at their respective CLs.

Wilks' theorem ensures the asymptotic behavior of the distribution of $\Delta L^c_{\rm min}$ as the number of events becomes large, and the 3 observed number in CDMS-II-Si may not be a large enough number to ensure that ΔL follows the classical chi-square distribution. Assuming that $\Delta L^c_{\rm min}$ is chi-square distributed, the choices of $\Delta L^* = 1.0$ and $\Delta L^* = 2.7$ correspond to the confidence intervals of $\tilde{\eta}$ at the 68% and 90% CL, respectively, for each $v_{\rm min}$. The question on the convergence to the true confidence interval is also present in the analysis of the CDMS-II-Si data with a fixed halo model, if one uses the confidence interval estimator derived from the same likelihood function [34, 36].

In [55], $\Delta L^* = 9.2$ is used to compute the confidence band at the 90% CL, a value much larger than our choice, corresponding to the 90% CL limit for a chi-squared distribution with five degrees of freedom, resulting from a numerical Monte Carlo simulation. However, in the simulation described in [55], only fake data with three simulated events are selectively generated instead of allowing for any number of simulated events, as would be necessary to avoid generating a biased data set. Yet, allowing the number of simulated events to vary does not seem compatible with the ΔL definition in Eq. (2.16) of [55]. In this equation, $\sqrt{\Delta L}$ is defined as the radius of a hyper-ellipsoid in a 6-dimensional parameter space defined by the positions and heights of the three steps in the best-fit $\tilde{\eta}_{BF}$ for a number of simulated events $N_O = 3$. This leads to a chi-squared distribution for ΔL with $2N_O - 1 = 5$ degrees of freedom (because there is one constraint). Allowing the number of simulated events N_O to change, the dimension of the $\tilde{\eta}_{BF}$ parameter space is not fixed to 6, but would be $2N_O$, leading to a number of degrees of freedom $2N_O - 1$ that would change from simulated set to simulated set.

3.3 Application to the CDMS-II-Si data

In this section, we apply the EHI method to the three events observed by CDMS-II-Si in their signal region with recoil energies 8.2, 9.5, and 12.3 keV. We follow the procedure developed above. We use $\Delta L^* = 1.0$ and 2.7 for the 68% CL and 90% CL confidence bands, and compare the bands with the 90% CL upper limits from CDMSlite [9], SuperCDMS [11], LUX [10], XENON100 [3] data, as well as the CDMS-II-Si data itself. The data analysis to obtain the upper limits is the same as in Sec. 2.1 [34]. Recent analyses of the CDMS-II-Ge data [84, 85] use the same data set of [4], shown in [25] to provide weaker upper limits in the halo-independent analysis than SuperCDMS (and thus not included here). The implementation of the data analysis is found in the CoddsDM software [53].

3.3.1 Elastic SI scattering

In this subsection we present the result of our analysis for elastic scattering with isospin-conserving $f_n/f_p = 1$ and with isospin-violating $f_n/f_p = -0.7$ (Xe-phobic) and $f_n/f_p = -0.8$ (Ge-phobic) SI interactions [65, 66, 76]. They are shown in the left and right panels of Fig. 3.3 and in Fig. 3.4, respectively, for a WIMP of mass $m = 9$ GeV. This value of the mass is within the 68% CL CDMS-II-Si regions obtained assuming the Standard Halo Model (SHM) in [25] and [34]. Figs. 3.3 and 3.4 show the best-fit $\tilde{\eta}_{\rm BF}$ (dark red line) and the 68% and 90% CL confidence bands derived from the CDMS-II-Si data shaded in darker and lighter red, respectively. Despite starting with three observed events, thus three steps in $\tilde{\eta}$, the $\tilde{\eta}_{\rm BF}$ has only two steps, located at the zeros of the $q(v_{\rm min})$ function shown in Fig. 3.5.

Fig. 3.5 shows the $\xi(v_{\rm min})$ (red lines) and $\sum_a H_a(v_{\rm min})/\gamma_a$ (blue lines) functions in the left panel, and the $q(v_{\rm min})$ function given in (3.1.31) (right panel) for the best-fit $\tilde{\eta}_{\rm BF}$ of the CDMS-II-Si data for spin-independent elastic scattering with $f_n/f_p = 1$. The zeros of $q(v_{\rm min})$, located at the points where the functions in the left panel of Fig. 3.5 touch, are at 507 and 580 km/s. These coincide with the locations of the steps of the best-fit $\tilde{\eta}_{\rm BF}$ plotted in the left panel of Fig. 3.3. The location of the steps is practically the same for other f_n/f_p values. The shapes of the $\xi(v_{\rm min})$, $\sum_a H_a(v_{\rm min})/\gamma_a$, and $q(v_{\rm min})$ functions are almost unchanged for a different choice of f_n/f_p values, up to a rigid rescaling along the vertical axis. The only changes expected in the positions of the zeros of $q(v_{\rm min})$ for different f_n/f_p

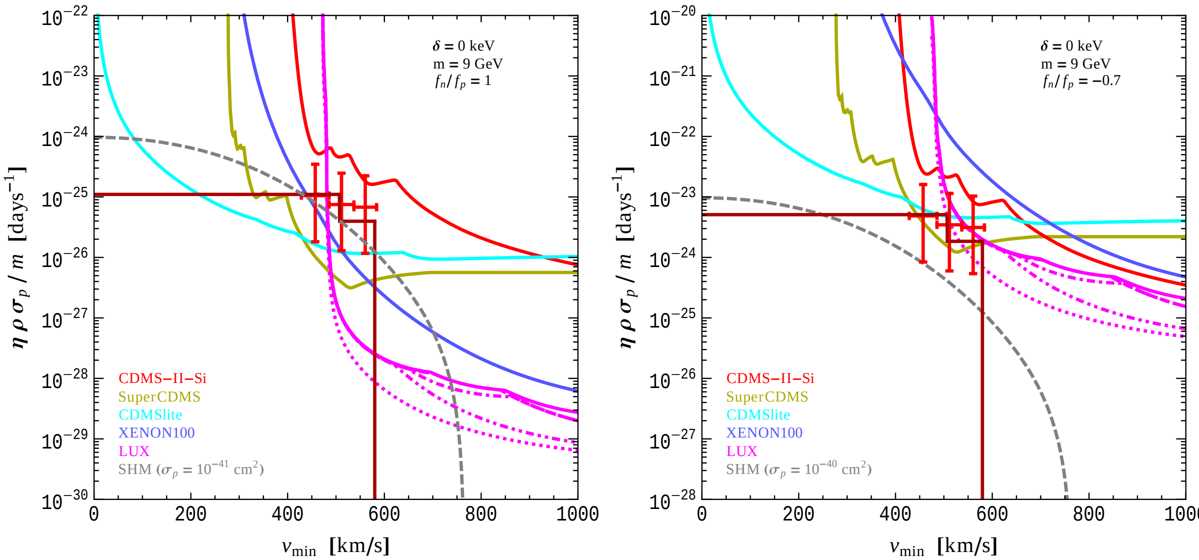

Figure 3.3. 90% CL bounds from CDMSlite, SuperCDMS, LUX, XENON100 and CDMS-II-Si, and the 68% CL and 90% CL confidence bands (see the text) from the three WIMP candidate events observed in CDMS-II-Si, for elastic isospin-conserving SI interaction ($f_n/f_p = 1$, left panel) and for elastic Xe-phobic isospin-violating SI interaction ($f_n/f_p = -0.7$, right panel), for WIMP mass $m = 9$ GeV.

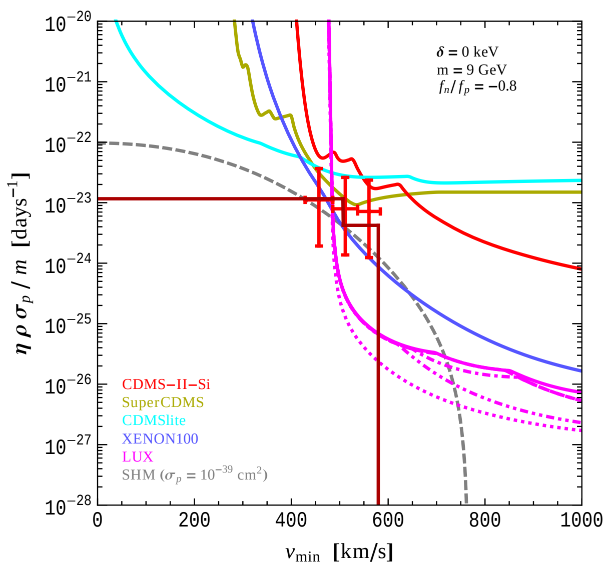

Figure 3.4. Same as Fig. 3.3, but for elastic Ge-phobic ($f_n/f_p = -0.8$) isospin-violating SI interaction.

values are due to the very small change in the relative strength of the WIMP interaction with different isotopes.

Figs. 3.3 and 3.4 show the 90% CL CDMSlite (cyan), SuperCDMS (dark yellow), LUX (magenta), XENON100(blue) and CDMS-II-Si (red) upper limits, and the red crosses derived from the halo-independent analysis using binned data [25]. The crosses represent 68% CL intervals of averaged $\tilde{\eta}$ and the corresponding $v_{\rm min}$ ranges for the CDMS-II-Si data with three

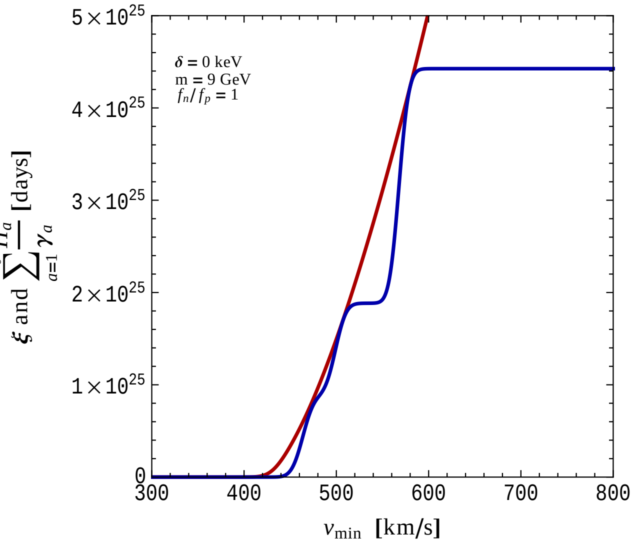

Figure 3.5. $\xi(v_{\min})$ (red) and $\sum_{a=1}^{N_O} H_a(v_{\min})/\gamma_a$ (blue) (left panel), and $q(v_{\min}) = 2\xi(v_{\min}) - 2\sum_{a=1}^{N_O} H_a(v_{\min})/\gamma_a$ (right panel) for SI elastic interaction with $m = 9$ GeV (see the text).

equally spaced bins spanning the recoil energy range from 7 to 13 keV. Notice that the 68% CL crosses are similar in vertical extent to the 68% CL confidence band. Notice also that the 90% CL CDMS-II-Si limit follows closely the upper limit of the 90% CL confidence band.

As one can see in the left panel of Fig. 3.3 for $f_n/f_p = 1$, the 68% CL confidence band is excluded in the $v_{\min}$ range from 370 to 560 km/s, by the combination of the 90% CL CDMSlite, SuperCDMS, and LUX upper limits. The lower boundary of the 90% CL confidence band is also cut at 450 km/s by the SuperCDMS 90% CL limit. Since there is no single continuous curve within the 90% CL confidence band which does not cross any 90% CL upper limit, we conclude that the potential signal and limits are incompatible for any halo model.

On the other hand, in the right panel of Fig. 3.3 a significant portion of the 68% CL confidence band remains below all the 90% CL upper limits. This shows that for SI interactions with $f_n/f_p = -0.7$ the CDMS-II-Si signal is consistent with the null results of all other experiments.

The choice of $f_n/f_p = -0.8$ (Fig. 3.4) disfavors maximally the Ge limits (while $f_n/f_p = -0.7$ disfavors maximally Xe couplings instead). Thus, as expected, in Fig. 3.4 the SuperCDMS limit is weakened with respect to Fig. 3.3, but the LUX upper limits exclude almost completely both confidence bands.

The dashed gray curves in Figs. 3.3 and 3.4 are the $\tilde{\eta}$ functions assuming the SHM for

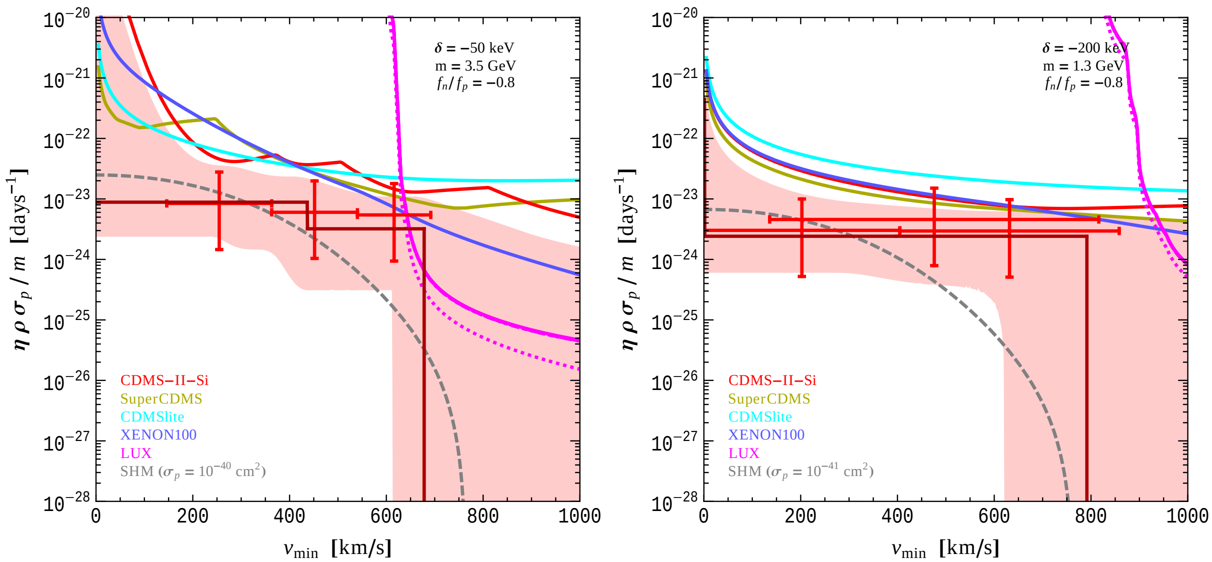

Figure 3.6. Same as Fig. 3.3, but for Ge-phobic isospin-violating SI interaction ($f_n/f_p = -0.8$) with $m = 3.5$ GeV and $\delta = -50$ keV (left panel), and $m = 1.3$ GeV and $\delta = -200$ keV (right panel).

WIMP-proton cross sections $\sigma_p = 10^{-41}$ cm^2 and $\sigma_p = 10^{-40}$ cm^2 in the left and right panels of Fig. 3.3, and $\sigma_p = 10^{-39}$ cm^2 in Fig. 3.4. For $m = 9$ GeV, these σ_p values are within the 68% and 90% CL CDMS-II-Si regions obtained assuming the SHM (in Fig. 1 of [25] and in Fig. 4 of [34], respectively). In the analyses of [25] and [34] assuming the SHM, the m and σ_p choices for $f_n/f_p = 1$ and $f_n/f_p = -0.8$ interactions are shown to be rejected, while the choice for $f_n/f_p = -0.7$ interactions are allowed by all 90% upper limits. The same conclusions are evident in Figs. 3.3 and 3.4, where the dashed gray lines are above the upper limits for $f_n/f_p = 1$ and $f_n/f_p = -0.8$ and below them for $f_n/f_p = -0.7$.

3.3.2 Inelastic SI scattering

In this subsection we present the results of the analysis for the exothermic Ge-phobic WIMP proposed in [34, 77] as an interpretation of the CDMS-II-Si data, shown in Fig. 3.6.This choice of $f_n/f_p = -0.8$ suppresses maximally the coupling to Ge. The limits due to Xe are weakened by the exothermic nature of the scattering, which disfavors heavier targets (such as Xe) with respect to lighter ones (such as Si) [34], leaving in principle Ge limits as the most important.

Fig. 3.6 shows our results for a WIMP mass $m = 3.5$ GeV and mass split $\delta = -50$ keV (left panel), and $m = 1.3$ GeV and $\delta = -200$ keV (right panel). These masses are shown in [34] to be within the CDMS-II-Si 90% and 68% CL regions when assuming the SHM, for

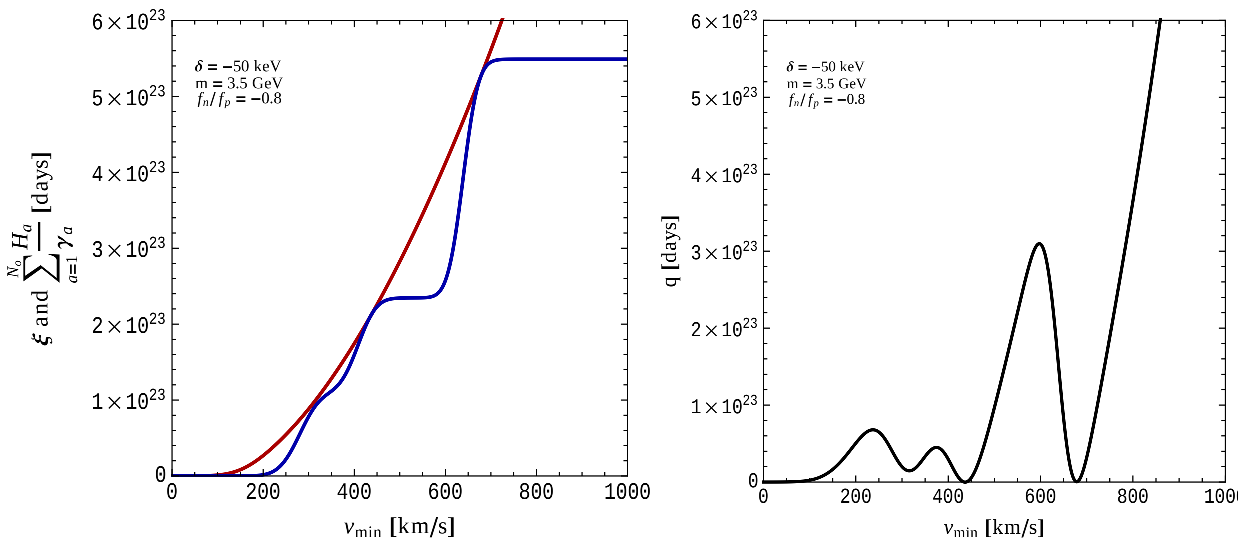

Figure 3.7. Same as Fig. 3.5, but for SI exothermic inelastic interaction with $m = 3.5$ GeV and $\delta = -50$ keV (see the text).

$\sigma_p = 10^{-40}$ cm^2 and 10^{-41} cm^2, respectively (see Figs. 5 and 6 of [34]). This is corroborated by the present halo-independent analysis, since the corresponding $\tilde{\eta}$ functions assuming the SHM shown in Fig. 3.6 (dashed gray lines) escape all upper limits from experiments with null results.

The best-fit $\tilde{\eta}_{\rm BF}$ functions for both Ge-phobic cases are shown in dark red in Fig. 3.6. They have two and one steps respectively in the left and right panels of Fig. 3.6, corresponding to the zeros of the $q(v_{\rm min})$ functions in the right panels of Figs. 3.7 and 3.8 (located at $v_{\rm min}$ values of 437 and 678 km/s in Fig. 3.7 and 792 km/s in Fig. 3.8).

Figs. 3.7 and 3.8 show the functions ξ (red) and $\sum_{a=1}^{N_O} H_a(v_{\rm min})/\gamma_a$ (blue) in the left panels, and twice their difference, $q(v_{\rm min})$, in the right panels, for the two Ge-phobic cases in Fig. 3.6.

In the previous analysis of Ge-phobic exothermic WIMP based on the SHM [34], the m and σ_p parameters chosen in the current analysis are found to be compatible with the null results of all other experiments. Consistently with this result, we find a large portion of the 68% CL confidence band is below all the 90% CL upper limits imposed by all null results. Thus WIMP-nucleus scattering through Ge-phobic interaction can potentially explain the CDMS-II-Si data as a WIMP signal without any conflict with the null results of all other searches.

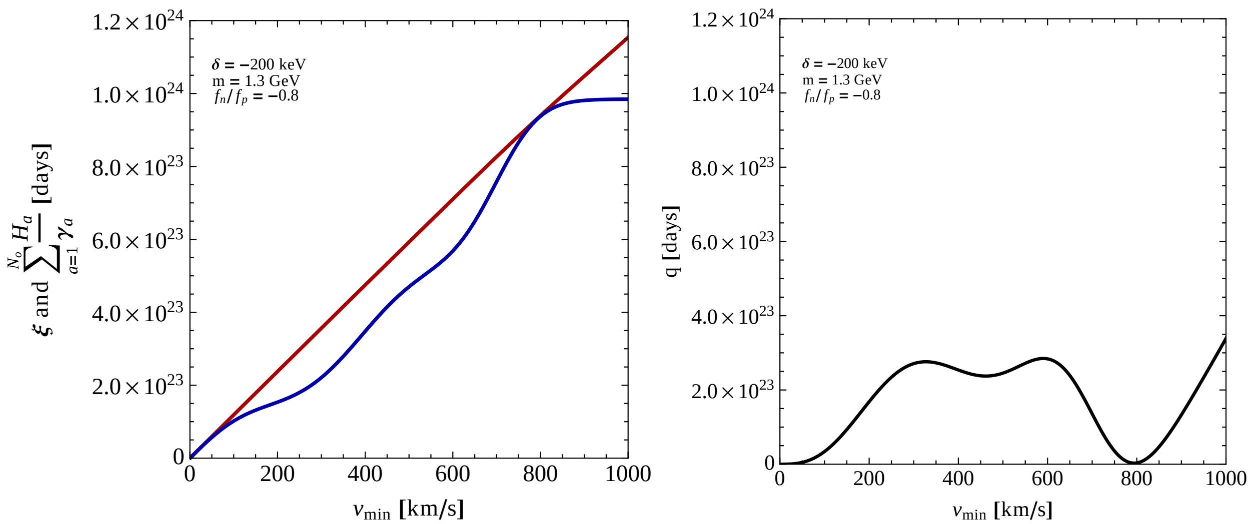

Figure 3.8. Same as Fig. 3.5, but for SI exothermic inelastic interaction with $m = 1.3$ GeV and $\delta = -200$ keV (see the text).

3.4 Conclusions for Chapter 3

We have expanded and corrected a recently proposed extended maximum likelihood halo-independent (EHI) method to analyze unbinned direct dark matter detection data. Instead of the recoil energy E_R as independent variable, we use $v_{\min}$, the minimum speed a dark matter particle must have to impart a given recoil energy to a nucleus. An earlier version of the method, using E_R as variable, was introduced in [55]. The use of $v_{\min}$ as variable allows to incorporate in the analysis any type of target composition and of WIMP-nucleus interaction, including elastic and inelastic collisions. This is not possible using E_R. The advantages of using $v_{\min}$ instead of E_R in a halo-independent analysis was first pointed out in [46] and extensively used later on [25, 34, 48, 50, 52].

The EHI method uses unbinned direct dark matter detection data. The predicted differential rate as a function of the observed energy E' in all direct detection experiments can be written in terms of a common function $\tilde{\eta}(v_{\min})$ (see (1.3.9)). The aim of the method is to find the $\tilde{\eta}$ function that provides the best fit for the unbinned data. We have proven rigorously that the best-fit $\tilde{\eta}$ function, $\tilde{\eta}_{\mathrm{BF}}(v_{\min})$, is a piecewise constant function with a number of discontinuities smaller than or equal to the number of observed events N_O. We have also rigorously defined a two-sided pointwise confidence band with a clear statistical meaning, as a collection of confidence intervals in $\tilde{\eta}$ for every $v_{\min}$ value. We can assign a confidence level to the band and thus compare with upper limits given at particular confidence levels. This allows to quantitatively assess the compatibility of the unbinned data with upper limits due to null results.

Using this method, we analyzed the compatibility of the three candidate events found by CDMS-II-Si with the best available upper bounds, for spin-independent (SI) WIMP-nucleus interactions with different neutron to proton coupling ratio f_n/f_p values and either elastic or exothermic inelastic scattering. We found the best-fit $\tilde{\eta}_{\rm BF}$ function and 68% and 90% CL confidence bands. We chose values of the WIMP mass within the CDMS-II-Si regions in the m–σ_p plane that we had found in previous studies [25, 34] assuming the Standard Halo Model (SHM). Our results for $f_n/f_p = 1$, WIMP mass $m = 9$ GeV and elastic scattering are shown in the left panel of Fig. 3.3. The 90% CL CDMSlite, SuperCDMS and LUX limits derived as in [34] exclude the entire 90% CL band for this candidate. This case was also studied in [55], where the best-fit $\tilde{\eta}_{\rm BF}$ is very similar to ours, but the 90% CL band is much larger. In [55], only 90% CL limits derived from LUX and XENON10 data are presented. The LUX limit in [55] is similar to ours, but it does not exclude their much larger confidence band.

The right panel of Fig. 3.3 shows our results for $f_n/f_p = -0.7$ (Xe-phobic) and $m = 9$ GeV. We found that in this case a significant portion of the 68% and 90% CL confidence bands remains below all the 90% CL upper limits. Thus, a WIMP candidate with these characteristics provides an explanation for the three CDMS-II-Si events compatible with all present null results of other direct searches. This case was also studied in [55], where their best-fit $\tilde{\eta}_{\rm BF}$ function has the same number and position of steps as ours, but is an order of magnitude larger. We think this difference is due to the inclusion of the isotopic composition of Si in our computation, which can not be done with the method used in [55]. The LUX limit presented in [55] for this case is similar to ours, but their 90% CL band is again much larger.

The Ge-phobic $f_n/f_p = -0.8$ case, again for $m = 9$ GeV, is presented in Fig. 3.4. The 90% CL confidence band is almost completely excluded by the 90% CL LUX limit.

Our results for the Ge-phobic coupling and exothermic inelastic scattering are presented in Fig. 3.6, for two different values of the WIMP mass m and mass split δ: $m = 3.5$ GeV, $\delta = -50$ keV and $m = 1.3$ GeV, $\delta = -200$ keV. In these cases the 68% and 90% CL confidence bands are almost entirely below all the 90% CL limits. Thus, again we found compatibility between a dark matter interpretation of the CDMS-II-Si data and all null results.

In all cases studied we included the crosses derived from the CDMS-II-Si data obtained with our previous halo-independent analysis using binned data [25, 34]. The crosses represent 68% CL intervals of averaged $\tilde{\eta}$ and $v_{\rm min}$ ranges corresponding to three equally-spaced bins spanning the recoil energy range from 7 to 13 keV. We found that the crosses are similar in vertical extent to the 68% CL confidence bands in all cases. This shows agreement between both types of halo-independent analyses, but the present method is much more powerful.

We found remarkable that the 90% CL limit derived from the CDMS-II-Si data itself using the Maximum Gap method, as described in [25, 34] (and references therein) is almost identical to the 90% CL upper boundary of the 90% CL confidence band in all cases studied. Again, this indicates agreement between the two different analyses.

SI elastic scattering was also studied in [70] and [73], where two different statistics were used to quantify the compatibility among different direct search data sets. In [70], for isospin-conserving SI interactions and WIMP mass 7 GeV, which is slightly smaller than our choice of 9 GeV, the parameter goodness-of-fit value derived from the global likelihood of the CDMS-II-Si, SuperCDMS and LUX data has a p-value of only 0.44%. This poor compatibility level is consistent with our results. For isospin-violating interactions, [70] used slightly different parameter sets, $f_n/f_p = -0.71$, $m = 6.2$ GeV, and $f_n/f_p = -0.79$, $m = 6.3$ GeV, with corresponding p-values of 18.7% and 18.5%. Thus the compatibility is significantly improved, which is also consistent with our results. In [73], a test statistic "$p_{\rm joint}$" is proposed and calculated, said to be the upper bound on the joint probability of obtaining the outcomes of two potentially conflicting experiments. Only if the value of $p_{\rm joint}$ is small there is a clear interpretation of incompatibility, but a large $p_{\rm joint}$ value does not imply compatibility. For $m = 9$ GeV, [73] finds incompatibility between CDMS-II-Si and SuperCDMS for $f_n/f_p = 1$, but not for $f_n/f_p = -0.7$ or -0.8. In this respect, we agree.

The use of a test statistic such as defined in [70] or [73] is complementary to our method of using a confidence band and upper limits in $v_{\rm min} - \tilde{\eta}$ space to assess the compatibility among different data sets.

CHAPTER 4

Reevaluation of Spin-dependent WIMP-proton Interactions as an Explanation of the DAMA Data

Over the years, several particle candidates have been proposed with properties which enhance a potential signal in DAMA and weaken the main limits imposed by direct DM searches with negative results, among them WIMPs with spin-dependent coupling mostly to protons, which we reevaluate in this chapter.

As already explained in the introduction, inelastic DM [26–32] scatters to another particle state, either heavier (endothermic scattering) or lighter (exothermic scattering, see e.g. [33, 34]), when colliding with a nucleus. Endothermic scattering favors heavier targets, thus enhancing scattering off I in DAMA while reducing scattering off lighter targets such as Ge. Moreover, this type of interaction enhances the annual modulation amplitude, thus pushing the cross section needed to fit the DAMA data to lower values. However, experiments employing Xe as target material, which is heavier than I, rule out endothermic scattering of DM as an explanation to the DAMA data unless there is an additional feature of the interaction that favors a signal in DAMA. Two types of WIMP couplings favor Na and I (DAMA) over Xe (LUX, XENON10) and Ge (CDMS, SuperCDMS): a spin-dependent coupling mostly to protons and a magnetic dipole moment coupling [31, 86]. The reason for the first is that the spin of a nucleus is mostly due to an unpaired nucleon and Na and I have an unpaired proton, while Xe and Ge have an unpaired neutron. The reason for the second is the large magnetic moment of both Na and I. We do not consider here inelastic magnetic DM, which [32] recently found still marginally compatible with all negative results of direct searches, for a small value of the I quenching factor (without the aid of inelasticity, instead, this candidate has been shown to be ruled out [52]).

The possibility that a DM candidate with spin-dependent interactions mostly with protons would explain the DAMA signal was, to the best of our knowledge, first studied in [87]. Compared to spin-independent interactions, spin-dependent couplings reduce the bounds from experiments with heavy targets, most notably LUX, due to the lack of the usual A_T^2 enhancement factor proper to the spin-independent interaction (A_T being the mass number of the target nucleus). This interaction might explain why the DAMA signal is not seen by LUX and SuperCDMS. In this case, bounds from PICASSO, SIMPLE, COUPP, and KIMS become relevant, since they contain F, I and Cs, all nuclei with an unpaired proton. This candidate was further studied in [88], in the context of both elastic and inelastic endothermic scatterings. The inelastic endothermic kinematics reduces the expected rate in experiments employing F (PICASSO, SIMPLE) because it is light, thus making the COUPP (CF_3I) and KIMS (CsI) bounds the most relevant constraints on WIMP scatterings off I in DAMA. [32] found that a small portion of the parameter space favored by DAMA for inelastic spin-dependent couplings with protons can still escape all bounds from null experiments.

Inelastic exothermic scattering [33, 35] favors lighter targets, so it favors Na in DAMA over heavier nuclei (Ge and Xe). In this case the most important limits are set by experiments containing F (PICASSO and SIMPLE).

Recently, [57] studied a Dirac WIMP candidate coupled to standard model (SM) fermions through a light pseudo-scalar mediator, and claimed that with a contact interaction and elastic scattering it reconciles the DAMA data with the null results of other experiments at the 99% credible level. The model produces a non-standard spin-dependent interaction, with the noteworthy feature that, for universal flavor-diagonal quark couplings to the pseudo-scalar mediator, the WIMP couples mainly to protons. The couplings of pseudo-scalar light bosons ($m_\phi < 7$ GeV) with quarks are strongly constrained by rare meson decays [89–91], and unless the pseudo-scalar coupling to the DM (called $g_{\rm DM}$ below) is very large, $g_{\rm DM} \gtrsim 10^3$, the one-particle exchange scattering cross section required in [57] is rejected [91]. The flavor physics bounds on pseudo-scalar couplings to quarks proportional to the quark mass are less stringent [91], but in this case [57] found that the resulting proton to neutron coupling ratio is not large enough to reconcile a DM signal in DAMA with the results of other direct detection experiments. Leaving aside the limits from other types of experiments we concentrate here on direct detection.

[57] employed a Bayesian analysis, where a number of uncertain parameters like quenching factors and background levels, as well as astrophysical quantities, are marginalized over. While the process of marginalization (i.e. integrating over nuisance parameters with assumed prior probability distributions) is the proper treatment of uncertain and uninteresting parameters in the context of Bayesian statistics, it makes it unclear whether there exists at least one set of values of the uncertain parameters, in particular one halo model, that produces the same result of the analysis.

Here we reconsider the viability of a signal due to WIMPs with spin-dependent coupling mostly to protons as an explanation of the DAMA data. We study both axial-vector and pseudo-scalar couplings, which lead respectively to $\vec{s}_\chi \cdot \vec{s}_p$ and $(\vec{s}_\chi \cdot \vec{q})(\vec{s}_p \cdot \vec{q})$ couplings in the non-relativistic limit ($\vec{s}_\chi$ and $\vec{s}_p$ are the spins of the WIMP χ and the proton respectively, and $\vec{q}$ is the momentum transfer). We assume the mediator to be either heavy enough for the contact interaction limit to be valid, or otherwise much lighter than the typical momentum transfer of the scattering process than the typical momentum transfer of the scattering process (we refer to this last case as "massless"). The possibilities of elastic and inelastic scattering, both endothermic and exothermic, are considered.

In Sec. 4.1 we present the differential cross sections for axial-vector and pseudo-scalar couplings, which can be used in the direct detection rate formula in Sec. 1.3. The analysis methods we adopt for experimental data are described in Sec. 4.2, and our results assuming a standard model of the dark halo of our galaxy are presented in Sec. 4.3. In Sec. 4.4 we describe our halo-independent analysis and present the related results. Our conclusions are given in Sec. 4.6.

4.1 Cross sections

4.1.1 Axial-vector (AV) interaction

An AV coupling leads to the usual spin-dependent interaction. The effective Lagrangian for the elastic scattering of a DM particle χ, either a Dirac or a Majorana fermion, with AV couplings to nucleons, mediated by a vector boson of mass m_ϕ, is

$$\mathscr{L}_{\rm AV} = \frac{g_{\rm DM}}{2(m_\phi^2 - q^\mu q_\mu)} \sum_{N=p,n} a_N \, \bar{\chi}\gamma^\mu\gamma^5\chi \, \bar{N}\gamma_\mu\gamma^5 N \ . \tag{4.1.1}$$

Here we assumed a one-particle exchange process. q^μ is the momentum transfer four-vector, and N is a nucleon, p or n. $g_{\rm DM}$ and a_N are the mediator coupling constants to χ and N, respectively, and they are real. The scattering amplitude is

$$\mathscr{M}_{\rm AV} = \frac{g_{\rm DM}}{2(m_\phi^2 - q^\mu q_\mu)} \sum_{N=p,n} a_N \, \bar{u}_\chi^{s'}\gamma^\mu\gamma^5 u_\chi^s \, \bar{u}_N^{r'}\gamma_\mu\gamma^5 u_N^r \ . \tag{4.1.2}$$

We now follow [92] because we will largely use the nuclear form factors given in this reference. We first take the non-relativistic limit of the Dirac spinors, in the chiral representation, for both χ and N: $u^s(\vec{p}) \simeq \sqrt{1/4m}\big((2m - \vec{p}\cdot\vec{\sigma})\,\xi^s, (2m + \vec{p}\cdot\vec{\sigma})\,\xi^s\big)^{\rm T}$, where $\vec{\sigma}$ are the Pauli matrices. This limit is justified by the fact that the DM initial speed and the exchanged momentum are small. The matrix element for scattering off a single nucleon then reads

$$\mathscr{M}_{\rm AV} = -8 m_N m \frac{g_{\rm DM}}{m_\phi^2 + q^2} \sum_{N=p,n} a_N \, \langle \vec{s}_\chi \rangle \cdot \langle \vec{s}_N \rangle \ , \tag{4.1.3}$$

where $\langle \vec{s}_\chi \rangle = \xi_\chi^{s'\dagger} \frac{\vec{\sigma}}{2} \xi_\chi^s$ and $\langle \vec{s}_N \rangle = \xi_N^{r'\dagger} \frac{\vec{\sigma}}{2} \xi_N^r$ (see e.g. (44), (47d), and (49) of [93]). Notice that this matrix element assumes the usual form for the Dirac spinors with normalization $\bar{u}^{s'}(\vec{p})\, u^s(\vec{p}) = 2m\delta^{ss'}$; Quantum Mechanical amplitudes usually assume a different state normalization, which differs by a factor of $2\sqrt{m^2 + \vec{p}^2}$. With this normalization (4.1.3) would be replaced by $\mathscr{M}_{\rm AV}^{\rm QM} = -2 g_{\rm DM}(q^2 + m_\phi^2)^{-1} \sum_{N=p,n} a_N \, \langle \vec{s}_\chi \rangle \cdot \langle \vec{s}_N \rangle$.

For a model of inelastic DM, one could introduce two Dirac fields, χ_1 and χ_2, with slightly different masses and the DM-nucleon effective Lagrangian

$$\mathscr{L}_{\rm AV} = \frac{g_{\rm DM}}{2(m_\phi^2 + q^2)} \sum_{N=p,n} a_N \, \bar{\chi}_2 \gamma^\mu \gamma^5 \chi_1 \, \bar{N} \gamma_\mu \gamma^5 N + \text{h.c.} \; . \tag{4.1.4}$$

The $g_{\rm DM}$ coupling can now be complex. We use the same symbol, $g_{\rm DM}$, for the couplings in (4.1.1) and (4.1.4), because then the expression of $\sigma_p^{\rm AV}$ in (4.1.6) is valid both for elastic and inelastic scattering. χ_1 is the DM particle entering the scattering process, with mass m, while χ_2 is the DM particle in the final state, with mass $m' = m + \delta$. The sign of the mass splitting δ determines the different kinematic regimes: $\delta > 0$ implies endothermic scattering, $\delta < 0$ implies exothermic scattering, while $\delta = 0$ implies elastic scattering.

One may attempt to build an inelastic DM model without introducing additional degrees of freedom by assuming the interaction in (4.1.1) and adding a small Majorana mass term which produces two almost degenerate Majorana fermions, χ_1 and χ_2, in which case $\chi = \chi_1 + i\chi_2$ becomes a quasi-Dirac fermion. However, as noted in [88], this interaction produces diagonal terms which result in elastic scattering rather than inelastic. In this case, one can instead write an effective tensor interaction $\bar{\chi}\sigma^{\mu\nu}\chi \, \bar{N}\sigma_{\mu\nu}N$, which produces inelastic scattering since the diagonal interaction terms vanish identically. The non-relativistic limit of this operator is also $\vec{s}_\chi \cdot \vec{s}_N$.

The differential cross section for DM-nucleus scattering, for both the elastic and inelastic interactions introduced above in (4.1.1) and (4.1.4), is

$$\frac{{\rm d}\sigma_T^{\rm AV}}{{\rm d}E_R} = \sigma_p^{\rm AV} \, \frac{m_T}{2\mu_p^2} \left(\frac{m_\phi^2}{m_\phi^2 + 2m_T E_R} \right)^2 \frac{1}{v^2} F_{\rm AV}^2(q^2) \; , \tag{4.1.5}$$

where $E_R = q^2/2m_T$ is the nuclear recoil energy, v is the incoming WIMP speed, and μ_p is the DM-proton reduced mass. $F_{\rm AV}^2(q^2)$ is a nuclear form factor including spin dependence, and will be defined in Section 4.1.3. $\sigma_p^{\rm AV}$ is the total DM-proton cross section in the limit of contact interaction $m_\phi \gg q = \sqrt{2m_T E_R}$,

$$\sigma_p^{\rm AV} = \frac{3|g_{\rm DM}|^2 a_p^2}{4\pi} \frac{\mu_p^2}{m_\phi^4} \; . \tag{4.1.6}$$

The term in parenthesis in (4.1.5) accounts for long-range interactions, when m_ϕ is smaller than or comparable to $q = \sqrt{2m_{\rm T} E_R}$. For typical target masses of a few tens of GeV and recoil energies around few to tens of keV, the interaction becomes effectively long-range if the mediator mass is smaller than several MeV: $m_\phi \ll q \simeq 20 \text{ MeV}\sqrt{(E_R/10 \text{ keV})(m_T/20 \text{ GeV})}$.

In order to plot our results for long-range interactions, we express the differential cross section in terms of a reference total cross section $\sigma_p^{\text{AV, ref}} = \sigma_p^{\text{AV}}(m_\phi = m_\phi^{\text{ref}})$ corresponding to a reference mediator mass m_ϕ^{ref}, which we set equal to 1 GeV:

$$\frac{\mathrm{d}\sigma_T^{\text{AV}}}{\mathrm{d}E_R} = \sigma_p^{\text{AV, ref}} \frac{m_T}{2\mu_p^2} \left(\frac{(m_\phi^{\text{ref}})^2}{m_\phi^2 + 2m_T E_R} \right)^2 \frac{1}{v^2} F_{\text{AV}}^2(q^2) \ . \tag{4.1.7}$$

The massless mediator limit thus corresponds to setting $m_\phi = 0$ in the equation above. In the following we will refer to any scenario with $m_\phi^2 \ll q^2$ as massless mediator limit or long-range limit.

Given that a large value of a_p/a_n is needed to suppress the strong LUX and SuperCDMS constraints, we will assume the maximally isospin-violating coupling $a_n = 0$ for the AV interaction.

4.1.2 Pseudo-scalar (PS) interaction

Here the DM particle is a Dirac fermion χ, coupled to a real PS boson ϕ with mass m_ϕ,

$$\mathscr{L}_{\text{DM}} = -i\frac{g_{\text{DM}}}{\sqrt{2}} \phi\, \bar{\chi}\gamma^5\chi \tag{4.1.8}$$

(as in [57, 94]), with a real coupling constant g_{DM}. The PS field couples also to the SM quarks with real coupling g_q,

$$\mathscr{L}_q = -i\frac{1}{\sqrt{2}} \sum_q g_q\, \phi\, \bar{q}\gamma^5 q \ . \tag{4.1.9}$$

While PS couplings to quarks are usually taken to be proportional to the fermion mass (see e.g. [94]), we will assume instead a flavor-universal coupling $g_q = g$, which introduces a larger $|a_p/a_n|$ ratio, $a_p/a_n \simeq -16.4$ [57] (see below).

To model inelastic scattering we assume a non-diagonal coupling of two Dirac DM fields χ_1 and χ_2 with ϕ,

$$\mathscr{L}_{\text{DM}} = -i\frac{g_{\text{DM}}}{\sqrt{2}} \phi\, \bar{\chi}_2\gamma^5\chi_1 + \text{h.c.} \ . \tag{4.1.10}$$

Again, the g_{DM} coupling can now be complex. With this definition of g_{DM}, (4.1.8) and

(4.1.10) yield the same expression for $\sigma_p^{\rm PS}$ in (4.1.16). Diagonal interaction terms as well as non-diagonal mass terms can be forbidden by assuming a $\mathbb{Z}_2$ symmetry under which both ϕ, χ_1 (or χ_2), and all the SM electroweak doublets have charge -1.

The DM-nucleon effective Lagrangian, for elastic scattering (for inelastic scattering we should have $\bar\chi_2\gamma^5\chi_1$ instead of $\bar\chi\gamma^5\chi$), and assuming one-particle exchange, is

$$\mathscr{L}_{\rm PS} = \frac{g_{\rm DM}}{2(m_\phi^2 - q^\mu q_\mu)} \sum_{N=p,n} a_N\, \bar\chi\gamma^5\chi\, \bar N\gamma^5 N \ , \tag{4.1.11}$$

and yields in the non-relativistic limit

$$\mathscr{M}_{\rm PS} = 2\frac{g_{\rm DM}}{m_\phi^2 + q^2} \sum_{N=p,n} a_N\, (\langle\vec s_\chi\rangle\cdot\vec q)(\langle\vec s_N\rangle\cdot\vec q) \ , \tag{4.1.12}$$

where $\langle\vec s_\chi\rangle$ and $\langle\vec s_N\rangle$ were defined after (4.1.3). This is a different type of spin-dependent interaction than in (4.1.3). Due to the extra factors of $\vec q$, the PS cross section receives a large $q^4/m_N^2 m^2$ suppression with respect to the AV cross section. Therefore, the normalization of the signal and its spectrum, and also the nuclear form factors are different in the two cases [92] (see Section 4.1.3). Given the large momentum suppression, one needs to check the existence of unsuppressed radiative corrections to this tree-level cross section, that would spoil the setup. The PS interaction in (4.1.11) with a Dirac fermion χ has been proven not to produce such corrections [95], while this would not be the case if χ were a Majorana fermion.

The proton and neutron couplings appearing in (4.1.11) are given by

$$a_N = g \sum_{f=u,d,s} \frac{m_N}{m_f}\left[1 - \sum_{f'=u,\dots,t}\frac{\bar m}{m_{f'}}\right]\Delta_f^{(N)} = g \sum_{f=u,d,s} \frac{m_N}{m_f}\left[\sum_{f'=c,b,t}\frac{\bar m}{m_{f'}}\right]\Delta_f^{(N)} \ , \tag{4.1.13}$$

with $\bar m \equiv (1/m_u + 1/m_d + 1/m_s)^{-1}$. The subscripts f in (4.1.13) indicate quark flavors. The $\Delta_f^{(N)}$ factors parametrize the quark spin content of the nucleon, and are usually determined experimentally or computed with lattice calculations. As in [57], we adopt the following values from [96]:

$$\Delta_u^{(p)} = \Delta_d^{(n)} = +0.84 \ , \qquad \Delta_d^{(p)} = \Delta_u^{(n)} = -0.44 \ , \qquad \Delta_s^{(p)} = \Delta_s^{(n)} = -0.03 \ , \tag{4.1.14}$$

with which $a_p \simeq -0.4g$. As a natural feature of this model, the proton coupling a_p is larger (in modulus) than the neutron coupling a_n, by an amount that depends on the choice of the $\Delta_f^{(N)}$'s. As noted in [57], the values in (4.1.14) are conservative in the sense that they minimize the ratio a_p/a_n with respect to other values encountered in the literature (see e.g. Table 4 in [93]). In this case $a_p/a_n = -16.4$.

The differential cross section for the PS interaction, for both elastic and inelastic scattering, is

$$\frac{\mathrm{d}\sigma_T^{\mathrm{PS}}}{\mathrm{d}E_R} = \sigma_p^{\mathrm{PS}} \frac{3m_T^3 E_R^2}{8\mu_p^6} \frac{1}{v^{\mathrm{ref}4}} \left(\frac{m_\phi^2}{m_\phi^2 + 2m_T E_R} \right)^2 \frac{1}{v^2} F_{\mathrm{PS}}^2(q^2) \ . \tag{4.1.15}$$

$F_{\mathrm{PS}}^2(q^2)$, to be defined in Section 4.1.3, is the nuclear form factor including spin dependence. σ_p^{PS} is the total DM-proton cross section in the limit of contact interaction,

$$\sigma_p^{\mathrm{PS}} = \frac{|g_{\mathrm{DM}}|^2 a_p^2}{12\pi} \frac{\mu_p^6}{m_\phi^4} \frac{v^{\mathrm{ref}4}}{m^2 m_p^2} \ . \tag{4.1.16}$$

In this case, the total DM-proton cross section has a v^4 dependence, and, for the purpose of plotting our results in terms of the reference cross section, in (4.1.16) we evaluate σ_p^{PS} at a reference speed v^{ref}. We set v^{ref} equal to the rotational speed of our Local Standard of Rest, 220 km/s, which is representative of the WIMP speeds with respect to Earth.

For long-range PS interactions we proceed in the same manner as for the long-range AV interactions, by writing the differential cross section in terms of a reference total cross section $\sigma_p^{\mathrm{PS,\,ref}} = \sigma_p^{\mathrm{PS}}(m_\phi = m_\phi^{\mathrm{ref}})$, with $m_\phi^{\mathrm{ref}} = 1$ GeV:

$$\frac{\mathrm{d}\sigma_T^{\mathrm{PS}}}{\mathrm{d}E_R} = \sigma_p^{\mathrm{PS,\,ref}} \frac{3m_T^3 E_R^2}{8\mu_p^6} \frac{1}{v^{\mathrm{ref}4}} \left(\frac{(m_\phi^{\mathrm{ref}})^2}{m_\phi^2 + 2m_T E_R} \right)^2 \frac{1}{v^2} F_{\mathrm{PS}}^2(q^2) \ . \tag{4.1.17}$$

4.1.3 Nuclear form factors

We adopt the form factors computed in [92] using standard shell model techniques, for the nuclides for which they are available, namely the main stable isotopes of Ge, Xe, Na, I, and F. In these cases, we define

$$F_{\mathrm{AV}}^2(q^2) = \frac{1}{3a_p^2} \sum_{N,N'=p,n} a_N a_{N'} \left(F_{\Sigma''}^{(N,N')}(q^2) + F_{\Sigma'}^{(N,N')}(q^2) \right) \tag{4.1.18}$$

for the AV interaction, and

$$F^2_{\rm PS}(q^2) = \frac{1}{a_p^2} \sum_{N,N'=p,n} a_N a_{N'} F^{(N,N')}_{\Sigma''}(q^2) \tag{4.1.19}$$

for the PS interaction. The (squared) nuclear form factors $F_{\Sigma'}$ and $F_{\Sigma''}$ are tabulated in [92] for the nuclides mentioned above. These form factors can be employed unmodified also for inelastic scattering [32]. We include a factor of 1/3 in the definition of $F^2_{\rm AV}$ in order to normalize $F^2_{\rm AV}$ and $F^2_{\rm PS}$ to be 1 in the limit of zero momentum transfer when the target is an isolated proton. This factor traces back to $F_{\Sigma'}$ being twice as large as $F_{\Sigma''}$ at $q = 0$, which is consistent with the fact that $F_{\Sigma''}$ corresponds to the component of the nucleon spin along the direction of the momentum transfer, while $F_{\Sigma'}$ corresponds to the transverse component.

$F^2_{\rm AV}(q^2)$ can be expressed (see (59), (60) and (77c) in [92]) in terms of the usual nuclear spin structure function $S(q^2) = a_0^2 S_{00}(q^2) + a_0 a_1 S_{01}(q^2) + a_1^2 S_{11}(q^2)$ [97] (with $a_0 = a_p + a_n$ and $a_1 = a_p - a_n$ the isoscalar and isovector parameters):

$$F^2_{\rm AV}(q^2) = \frac{4\pi}{3(2J_T + 1)} \frac{1}{a_p^2} S(q^2) \ , \tag{4.1.20}$$

with J_T the spin of the target nucleus. At zero momentum transfer

$$S(0) = \frac{1}{\pi} \frac{(2J_T + 1)(J_T + 1)}{J_T} \left(a_p \langle S_p \rangle + a_n \langle S_n \rangle\right)^2 \ , \tag{4.1.21}$$

where $\langle S_p \rangle \equiv \langle J_T, M_T = J_T | S^z_p | J_T, M_T = J_T \rangle$, and where S^z_p is the component of $\vec{S}_p \equiv \sum_{\rm protons} \vec{s}_p$ along the z-axis [98] ($\langle S_n \rangle$ is defined analogously). Notice that $\langle S_p \rangle$ and $\langle S_n \rangle$ are often denoted with boldface style in the literature, although they are not vector quantities. $F^2_{\rm AV}$ can then be expressed in terms of the usually called spin-dependent form factor $F^2_{\rm SD}(q^2) = S(q^2)/S(0)$ as

$$F^2_{\rm AV}(q^2) = \frac{4(J_T + 1)}{3J_T} \left(\langle S_p \rangle + \frac{a_n}{a_p} \langle S_n \rangle \right)^2 F^2_{\rm SD}(q^2) \ . \tag{4.1.22}$$

For the nuclides for which no form factors have been computed in [92] (Cl, C and Cs), we define $F^2_{\rm AV}(q^2)$ by means of (4.1.22), with the spin-dependent form factor in Gaussian form

$$F^2_{\rm SD}(q^2) = e^{-q^2 R^2/4} \ ; \tag{4.1.23}$$

here we take $R = \left(0.92A_T^{1/3} + 2.68 - 0.78\sqrt{(A_T^{1/3} - 3.8)^2 + 0.2}\right)$ fm, with A_T the mass number of the target nucleus [99]. In this case we also assume $F^2_{\rm PS} = F^2_{\rm AV}$, which we expect to be approximately valid at low q^2. For Cs, a component of KIMS's target material, we take $\langle S_p \rangle = -0.370$, $\langle S_n \rangle = 0.003$ [100, 101]. For SIMPLE, we use $\langle S_p \rangle = -0.051$, $\langle S_n \rangle = -0.0088$ for both ^{35}Cl and ^{37}Cl [98], and $\langle S_p \rangle = -0.026$, $\langle S_n \rangle = -0.155$ for ^{13}C [102]. Notice that there are large uncertainties in the hadronic matrix elements $\langle S_p \rangle$ and $\langle S_n \rangle$ and the nuclear form factors, which differ in different nuclear models (see e.g. Fig. 1 of [103] for the Xe nuclear structure functions). Factors of 2 difference in different calculations are not uncommon [104].

4.2 Analysis assuming the SHM

In the following sections we examine the compatibility of the WIMP interpretation of the DAMA annual modulation signal with various null results for the AV and PS models described above. We consider both elastic, endothermic, and exothermic scattering.

4.2.1 Data analysis

In this section we describe the data analysis we perform assuming the SHM, which follows the procedure already presented in [51, 52]. The implementation of the data analysis can be found in the CoddsDM software [53].

The LUX, SuperCDMS and SIMPLE limits are computed as described in Sec. 2.1.

For the DAMA annual modulation signal, we take the data plotted in Fig. 8 of [16]. We determine the DAMA favored regions in the DM parameter space by performing a Maximum Likelihood analysis, assuming the data are Gaussian distributed. Due to the uncertainties residing in the quenching factors of Na and I, which play an important role in the analysis, we choose two values for each target, namely $Q_{\rm Na} = 0.40$ and 0.30 for Na, and $Q_{\rm I} = 0.09$ and 0.06 [105] for I (see e.g. [106] and references therein). In the analysis we adopt the combinations $Q_{\rm Na} = 0.30$ with $Q_{\rm I} = 0.06$, and $Q_{\rm Na} = 0.40$ with $Q_{\rm I} = 0.09$.

We also compute an upper limit on the WIMP cross section using the total rate measured by DAMA, employing the data points plotted in Fig. 1 of [14]. We restrict our analysis to energies above the experimental threshold of 2 keVee. Given the very large number of observed events in each bin, and the resulting small statistical fluctuations, we compute an upper bound on the cross section by requiring that the predicted rate does not exceed the observed rate in any energy bin. This limit is particularly important for exothermic scattering, which reduces the modulation amplitude with respect to the average rate.

For PICASSO we perform a Maximum Likelihood analysis using the data in Fig. 5 of [6]. The target material in PICASSO is C_4F_{10}, but the collaboration only considers scattering off F in their analysis [6]; we do the same, noting that the contribution of C for DM spin-dependent interactions with protons is anyway negligible. We construct our Gaussian likelihood using the expected rate above each one of the eight energy thresholds adopted by the collaboration (1.7, 2.9, 4.1, 5.8, 6.9, 16.3, 38.8, and 54.8 keV), and the measured rate with its uncertainty, which are already background subtracted.

For KIMS we perform again a Maximum Likelihood analysis using the data points with their 68% CL intervals from Fig. 4 of [12], assuming Gaussian distributed data. Because Cs and I have similar atomic masses, their quenching factors are not measured separately [107]. As for DAMA, we perform our analysis of the KIMS data adopting two values for $Q_{\rm I} = Q_{\rm Cs}$ in CsI: 0.05 and 0.10 (see Fig. 2 of [107], and Fig. 5 of [108] and references therein).

4.3 Results assuming the SHM

The plots in Figs. 4.1–4.3, 4.5–4.7, and 4.9–4.12 show 90% CL upper bounds and 68% CL (inner and darker shaded region), 90% CL (outer and lighter shaded region), 3σ (solid contour) and 5σ (dashed contour) allowed regions in the m–σ_p plane. The green shaded regions and green closed contours labeled 'DAMA$_1$' are the allowed regions compatible with the DAMA annual modulation, for quenching factors $Q_{\rm Na} = 0.40$ and $Q_{\rm I} = 0.09$ in dark green, and $Q_{\rm Na} = 0.30$ and $Q_{\rm I} = 0.06$ in light green. The lower the quenching factor, the higher is the DM mass needed to fit the data. The low and high WIMP mass regions correspond to the interpretation of the DAMA data as the WIMP scattering mostly off Na and I in the detector, respectively. The upper limit due to the DAMA total rate (black, and labeled 'DAMA$_0$ Na') is shown for scattering off Na assuming $Q_{\rm Na} = 0.40$. 90% CL upper limits from LUX data are shown as various magenta curves. As in [51] the different dashing styles of the lines indicate different selections of candidate events used in the Maximum Gap analysis: dotted (0 events), double-dot-dashed (1 event), dot-dashed (3 events), dashed (5 events) and solid (24 events) curves. Two purple lines show the 90% CL upper limits from KIMS data with quenching factors $Q_{\rm I} = Q_{\rm Cs} = 0.10$ (solid) and 0.05 (dashed). 90% CL upper limit from SIMPLE (brown), PICASSO (cyan), and SuperCDMS (dark yellow) are also drawn.

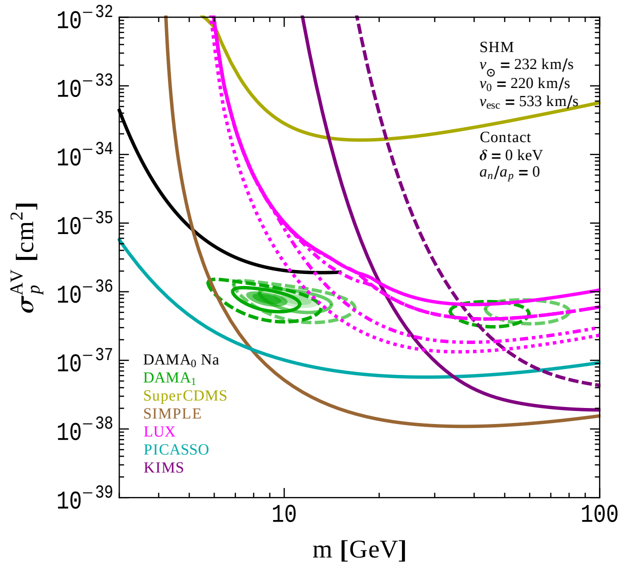

Figure 4.1. 90% CL bounds and 68% CL, 90% CL, 3σ, and 5σ allowed regions in the WIMP-proton reference cross section σ_p vs WIMP mass plane, assuming the SHM, for elastic proton-only contact AV interactions. The unmodulated DAMA rate limit (black) corresponds to a Na quenching factor of 0.40. Different line styles for the LUX bound correspond, from most to least constraining, to 0, 1, 3, 5 and 24 observed events (see text). The KIMS bound is shown for both $Q_{\rm I} = Q_{\rm Cs} = 0.10$ (solid line) and 0.05 (dashed line).

4.3.1 Elastic contact interactions

Fig. 4.1 shows our results for elastic proton-only contact AV interactions. The most stringent bounds come from two bubble chamber experiments, SIMPLE and PICASSO. Both of these limits exclude all the regions favored by the DAMA modulation signal.

Fig. 4.2 is the same as Fig. 4.1, but for PS interactions with flavor-universal coupling $a_n/a_p = -1/16.4$ (left panel), and with proton-only coupling $a_n = 0$ (right panel). As expected, the only limits that change from one case to the other are those of LUX and SuperCDMS, due to their enhanced sensitivity to DM-neutron couplings. The DAMA regions for WIMP scattering off Na are entirely excluded by SIMPLE and PICASSO, and the regions for scattering off I are excluded by KIMS when assuming similar values for the I quenching factor in both experiments. This result is different from what was found in [57], where some

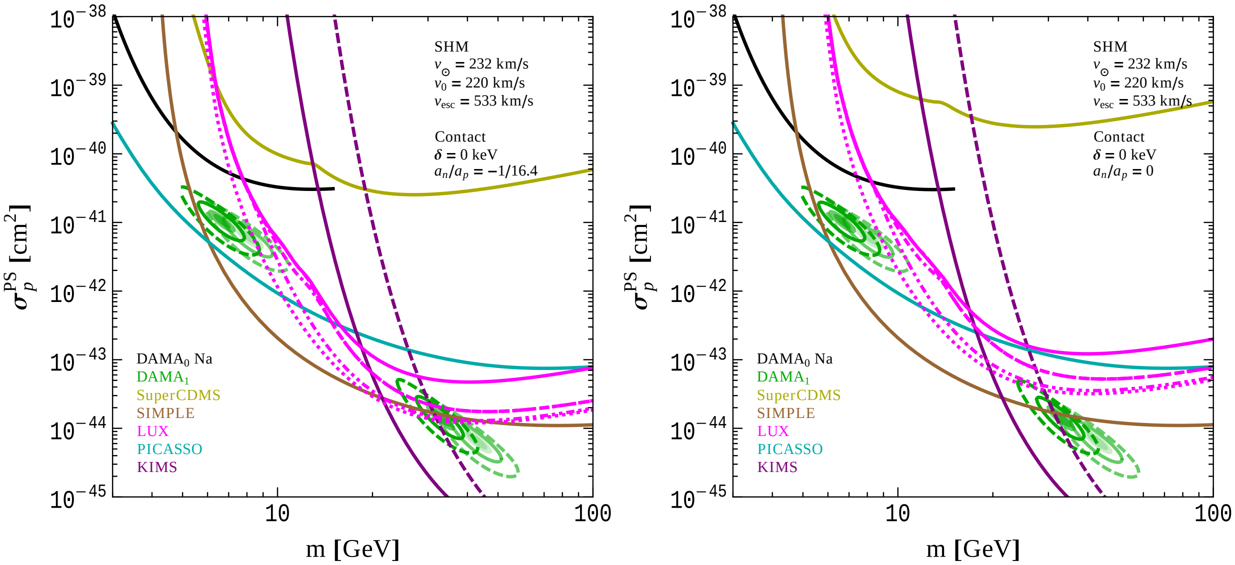

Figure 4.2. Same as Fig. 4.1 but for flavor-universal (left) and proton-only (right) PS interactions.

portion of the Na and I DAMA regions are compatible with all null experiments for the PS flavor-universal coupling.

[57] uses Bayesian statistics to infer 99% credible level exclusion limits, and 90% and 99% credible regions for DAMA, marginalizing over the SHM parameters using Gaussian priors (taking central values for the velocities $\overline{v_0} = 230$ km/s and $\overline{v_{\rm esc}} = 544$ km/s, and for the local WIMP density $\bar{\rho} = 0.3$ GeV/cm^3, with standard deviations $\Delta v_0 = 24.4$ km/s, $\Delta v_{\rm esc} = 39$ km/s and $\Delta\rho = 0.13$ GeV/cm^3). As a result, regions and limits at a specific point in parameter space do not necessarily correspond to a fixed set of values for the SHM parameters. In our analysis instead we assumed the same set of SHM parameter values across all experimental results. We found that the regions and limits move approximately in the same manner in the parameter space as we vary the DM velocities, and the DAMA regions fail to escape the upper bounds at the 90% CL. This can be seen in Fig. 4.3 (left panel), which shows the results for elastic PS interactions with flavor-universal coupling where both $v_{\rm esc}$ and v_0 are taken 3σ below their central values in [57] (however, we keep $v^{\rm ref} = 220$ km/s to plot σ_p). Our choice for the SHM velocities roughly matches the low mass SIMPLE limit in Fig. 1 of [57]. The right panel of Fig. 4.3 shows also the 99% CL upper bounds (dotted lines) for the same set of parameters. In this case, the high mass DAMA region corresponding to a quenching factor of 0.09 escapes the KIMS upper limit for quenching factor 0.05. The Na component of the DAMA region is still rejected by PICASSO at the 99% CL. In Fig. 4.4

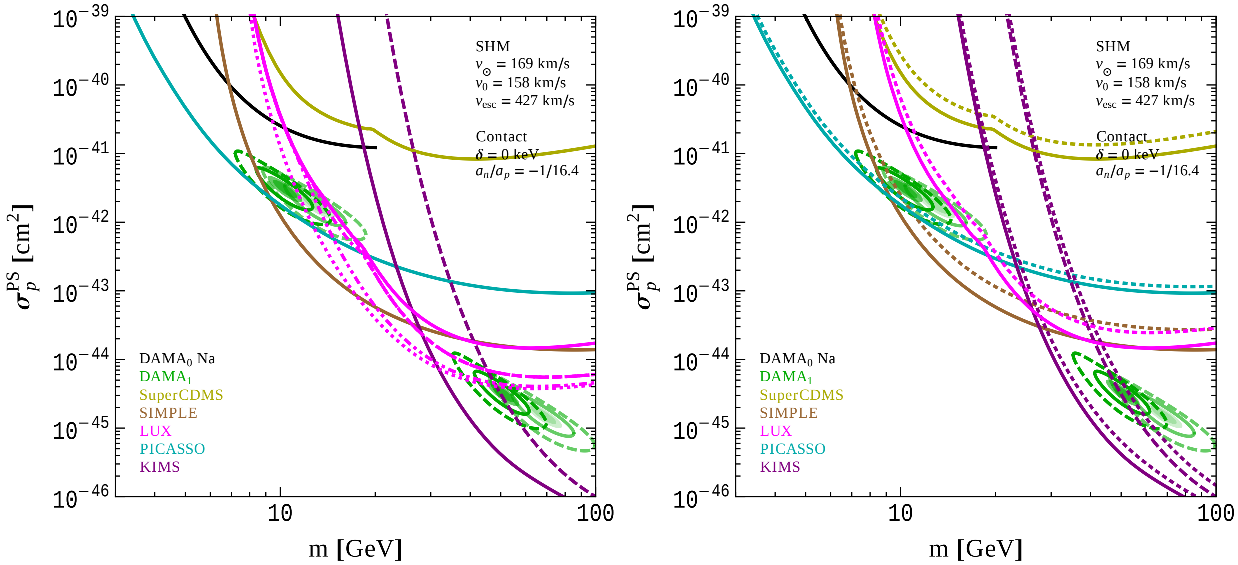

Figure 4.3. (left) Same as Fig. 4.2 but for v_0 and $v_{\rm esc}$ taken to be 3σ lower than the central values assumed in [57]. (right) Same as the left panel, but showing in addition 99% CL upper bounds (dotted lines) (only the LUX upper bound for 24 events is presented here).

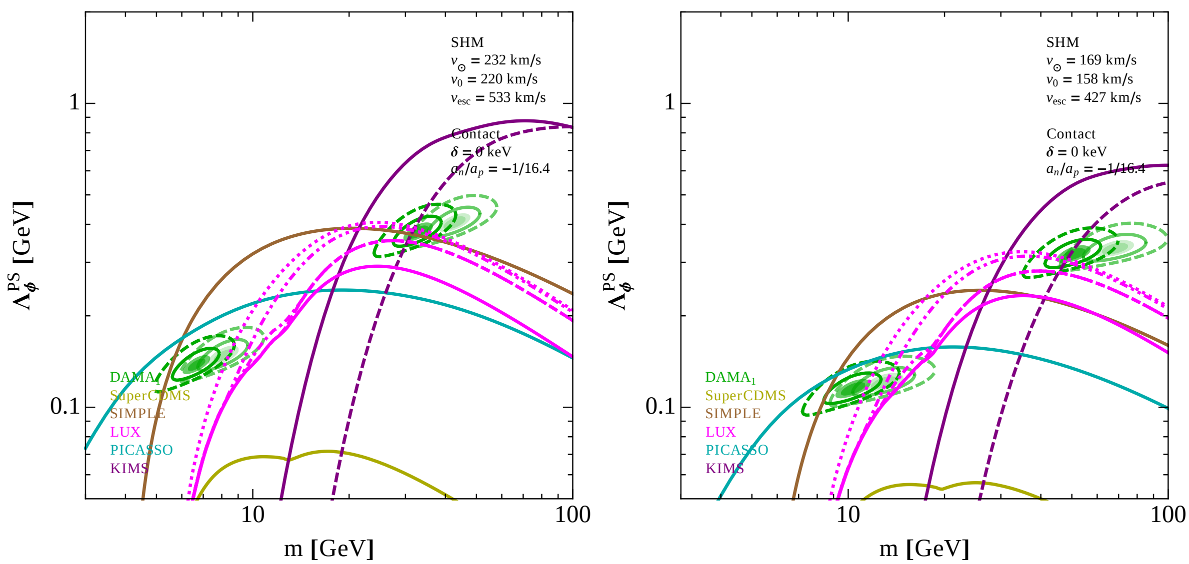

Figure 4.4. Same as the left panels in Figs. 4.2 and 4.3, but plotted in the $\Lambda_\phi \equiv m_\phi/\sqrt{g_{\rm DM} g}$ vs WIMP mass m plane as in Fig. 1 of [57].

we present our results from the left panels of Figs. 4.2 and 4.3 in the same plane as Fig. 1 of [57], namely in the m–Λ_ϕ plane, where $\Lambda_\phi \equiv m_\phi/\sqrt{g_{\rm DM} g}$. The allowed DAMA regions shown in [57] are much larger than the regions we found. We believe that this is due to their marginalization over the SHM parameters and experimental parameters including quenching factors.

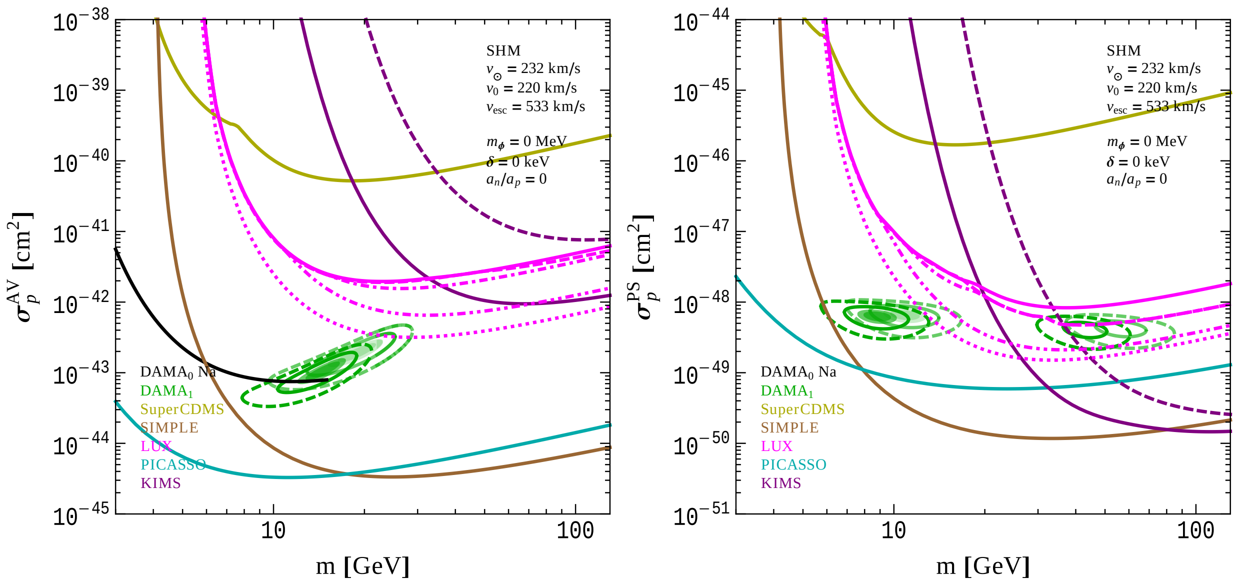

Figure 4.5. Same as Fig. 4.1 but for proton-only elastic AV (left) and PS (right) interactions via a massless mediator.

[91] found for PS interactions that the LUX bound excludes the DAMA region (see Fig. 9 in [91], where the I region in DAMA is completely excluded by LUX in both the contact and long-range limits). This is in disagreement with our conclusions, possibly because of the different analysis of the LUX data.

4.3.2 Elastic long-range interactions

Fig. 4.5 shows the regions and limits for elastic AV (left panel) and PS (right panel) interactions via a massless mediator. The results are shown in the reference cross section $\sigma_p^{\rm ref}$ vs DM mass m plane, where $\sigma_p^{\rm ref} = \sigma_p(m_\phi = m_\phi^{\rm ref})$ with $m_\phi^{\rm ref} = 1$ GeV. Note that the results for the contact AV and long-range PS interactions are very similar up to a shift in the vertical direction (compare Fig. 4.1 and the right panel of Fig. 4.5). This is expected from the E_R dependence of the differential cross sections given in (4.1.5) and (4.1.17): disregarding the form factors, the differential cross section for the long-range PS and contact AV interactions is proportional to E_R^0, for contact PS it is proportional to E_R^2, and for long-range AV it is proportional to E_R^{-2}. As it can be seen in Fig. 4.5, considering long-range elastic interactions does not help to bring compatibility between the DAMA regions and the upper limits from the experiments with null results.

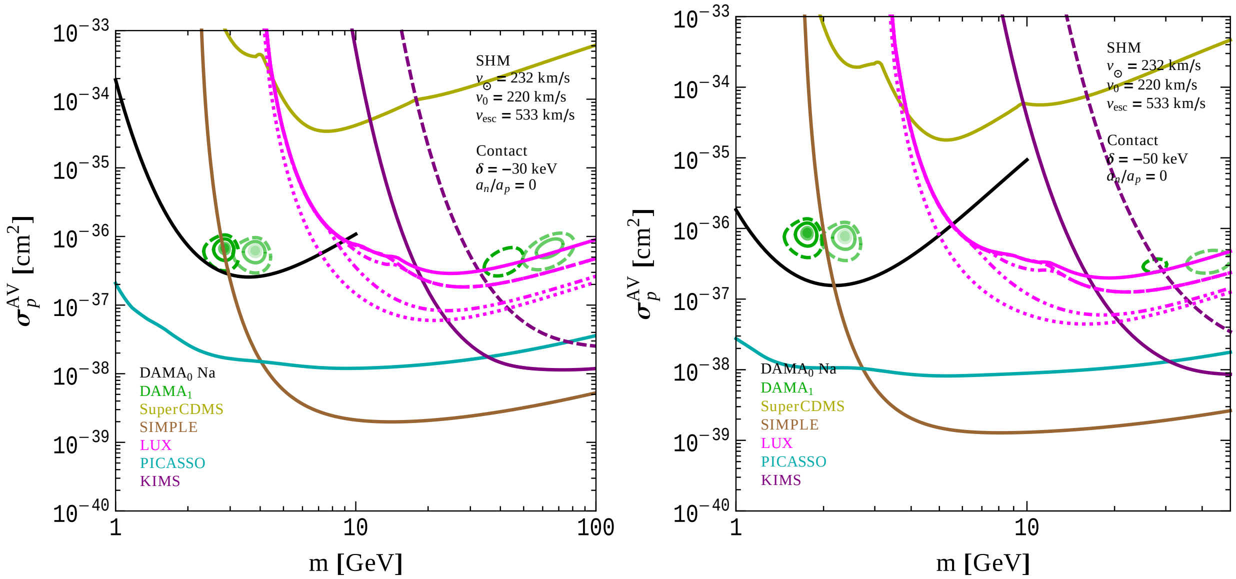

Figure 4.6. Same as Fig. 4.1 but for exothermic AV interactions with $\delta = -30$ keV (left) and $\delta = -50$ keV (right).

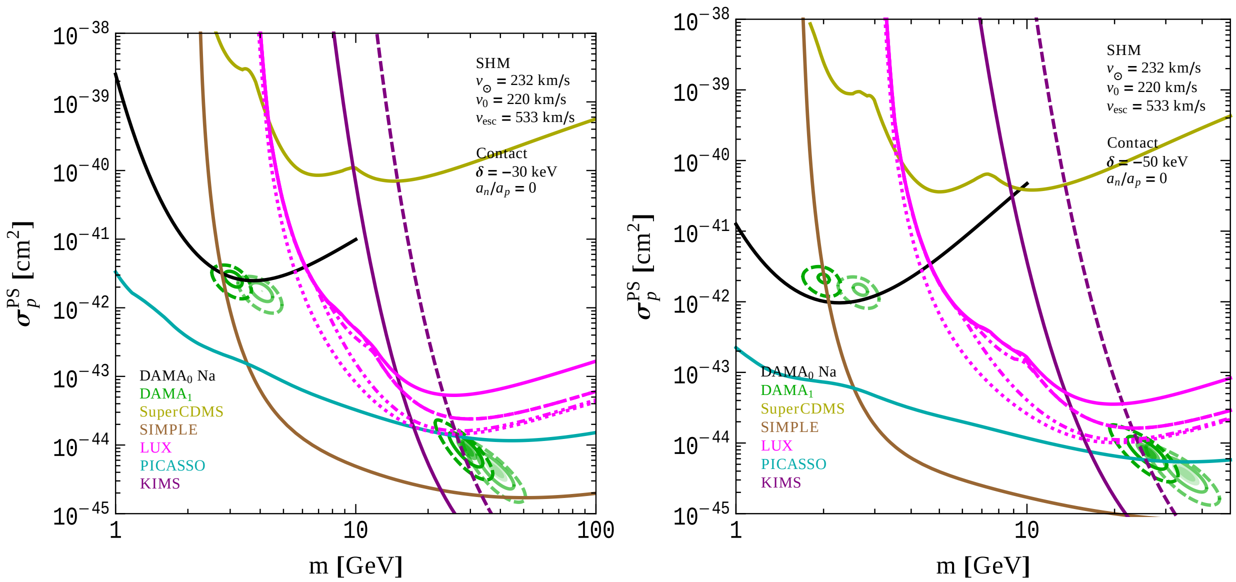

Figure 4.7. Same as Fig. 4.6 but for PS interactions.

4.3.3 Exothermic contact interactions

Figs. 4.6 and 4.7 show the results for exothermic inelastic proton-only AV and PS interactions, respectively, with $\delta = -30$ keV (left panels) and $\delta = -50$ keV (right panels). As $|\delta|$ increases, the DAMA regions move to lower masses, for the following reason.

The lowest reach in DM mass for a direct detection experiment is obtained when $E_R^{+,T}(v_{\max}) =$

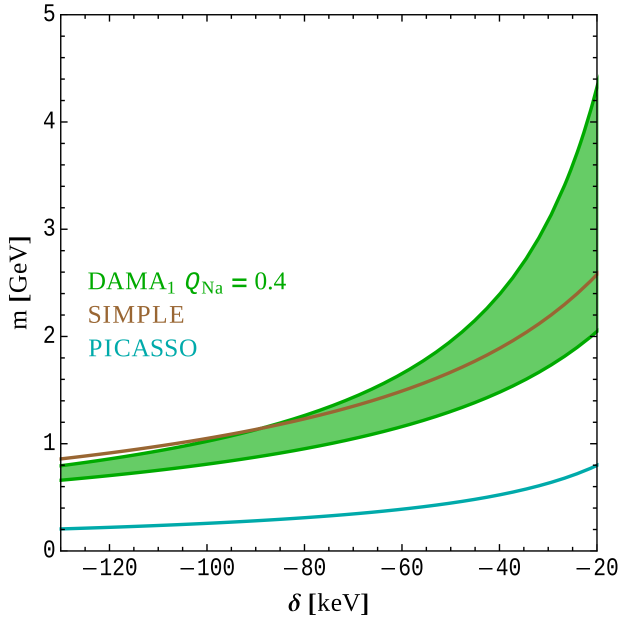

Figure 4.8. Estimated lowest reach in WIMP mass m for SIMPLE and PICASSO, and estimated mass range in which the Na component of the DAMA region with quenching factor 0.40 is found, as a function of mass splitting δ for exothermic scattering.

$E_{\rm th}$ (see Fig. 1.2), where the threshold energy $E_{\rm th}$ is the lowest detectable recoil energy. The mass reach can be found by extracting m as a function of δ and v from (1.2.2), for $E_R^{+,T}(v) = E_{\rm th}$,

$$\tilde{m}(\delta, v) = \frac{E_{\rm th} m_T}{v\sqrt{2E_{\rm th} m_T} - E_{\rm th} - \delta} \ , \tag{4.3.1}$$

and evaluating it at $v = v_{\rm max}$. The DAMA region will be therefore located at WIMP masses higher than $\tilde{m}(\delta, v_{\rm max})$, taking Na as the target element. For DAMA, $E_{\rm th} = 5$ keV for scattering off Na with quenching factor 0.40. The lowest reach of DAMA is the lower green line plotted in Fig. 4.8. Also shown in the same figure are the mass reaches of PICASSO and SIMPLE, for which we used $E_{\rm th} = 1.7$ keV and 8 keV, respectively. We only considered scattering off F in both experiments.

An estimated upper limit on the DM mass for the DAMA region comes from requiring that DM particles with speeds below 200 km/s always scatter below threshold and are therefore undetectable, because otherwise DAMA should have observed a sign change in the modulation amplitude (see Sec. 1.2). In other words, scatterings of DM particles slower than 200 km/s would yield a different phase for the modulated signal with respect to that measured by DAMA, and therefore an acceptable fit requires these scatterings to occur below threshold.

Since a fixed nuclear recoil energy can be imparted by heavier DM particles traveling at lower velocities, the condition $v_{\rm min}(E_{\rm th}) > 200$ km/s implies an upper limit on the DM mass in DAMA, given by $\tilde{m}(\delta, v = 200 \text{ km/s})$. This upper limit is the higher green line plotted in Fig. 4.8. The other possible condition to avoid scatterings of DM particles slower than 200 km/s, i.e. having a large enough $E_R^{-,T}(v = 200 \text{ km/s})$, would imply a very odd spectrum in DAMA, with more events at higher energy instead of the observed spectrum vanishing at high energy.

Since exothermic scattering decreases the value of $v_{\rm min}$ for a given recoil energy, the modulation amplitude becomes smaller with respect to the time-average rate. For large enough $|\delta|$ the DAMA modulation signal becomes inconsistent with the DAMA time-average rate. For values of δ lower than about -30 keV (for AV interactions) and -50 keV (for PS interactions), the DAMA total rate limit rules out the modulation signal in Na, as indicated by the black curve excluding the DAMA Na region in the right panels of Figs. 4.6 and 4.7.

For the values of δ allowed by the DAMA rate, the limit by PICASSO (and also the SIMPLE limit in most instances) rejects the allowed regions. For each value of δ on the horizontal axis of Fig. 4.8, the DAMA region spans a mass range enclosed within the green belt, while the SIMPLE and PICASSO lines indicate the mass value where the limits in the m–σ_p plane become vertical. From the plot it becomes clear that exothermic scattering brings compatibility between SIMPLE and DAMA for large enough $|\delta|$, as suggested by Figs. 4.6 and 4.7, however the region is rejected by the DAMA average rate measurements. While this is true for $Q_{\rm Na} = 0.40$, smaller quenching factors move the DAMA region to larger DM masses, thus potentially compromising this compatibility with SIMPLE. In any case, the DAMA region does not escape the PICASSO limit.

4.3.4 Exothermic long-range interactions

Fig. 4.9 shows the AV interaction via a massless mediator for $\delta = -30$ keV. Here as well, all the DAMA regions are rejected by the null experiments. We do not plot the results for long-range PS interactions as these are qualitatively similar to those for contact AV interactions, as commented above.

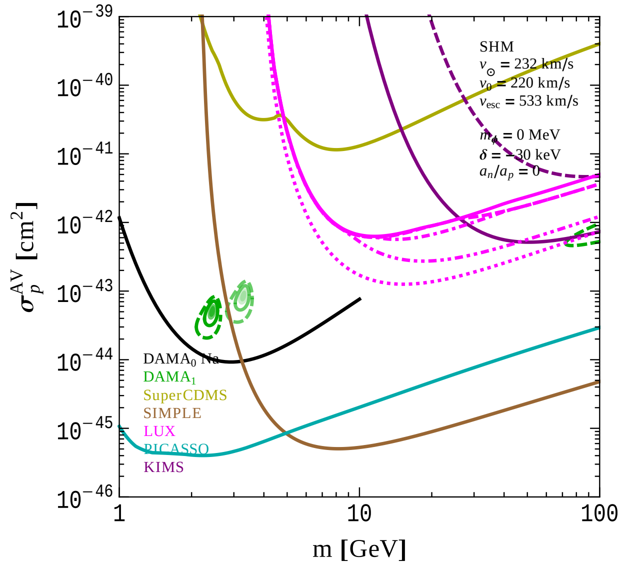

Figure 4.9. Same as Fig. 4.6 (left) but for a massless mediator.

4.3.5 Endothermic contact interactions

Figs. 4.10 and 4.11 show the result for the proton-only spin dependent endothermic scattering with AV and PS interactions, respectively, in the contact limit, with $\delta = 50$ keV (left panels) and $\delta = 100$ keV (right panels). As δ increases, scattering off light targets becomes kinematically forbidden since v_δ^T becomes larger than $v_{\rm max}$. For $\delta = 100$ keV, the only remaining limits are from KIMS and LUX. We can see that the DAMA region for I scattering moves towards the left compared to the KIMS upper bound as δ increases. For PS interactions with $\delta = 50$ keV, it is only the combination of larger quenching factor $Q_{\rm I} = 0.09$ for I in DAMA and smaller quenching factor $Q_{\rm I} = 0.05$ in KIMS that allows the DAMA signal to be compatible with all upper limits. For $\delta = 100$ keV, the I region corresponding to $Q_{\rm I} = 0.06$ barely escapes the limit with $Q_{\rm I} = 0.05$ from KIMS, and the situation remains tense for quenching factors 0.09 (DAMA) and 0.10 (KIMS). Raising δ further makes it progressively more difficult to find a region of the DAMA signal that is kinematically allowed. For AV interactions the DAMA regions are even more severely constrained: only the larger quenching factor $Q_{\rm I} = 0.09$ DAMA region is allowed by the KIMS upper bound with smaller quenching factor $Q_{\rm I} = 0.05$ for $\delta = 100$ keV.

These results are largely consistent with those of [32], where the framework of non-relativistic operators introduced in [92] was generalized to inelastic scattering and a model-

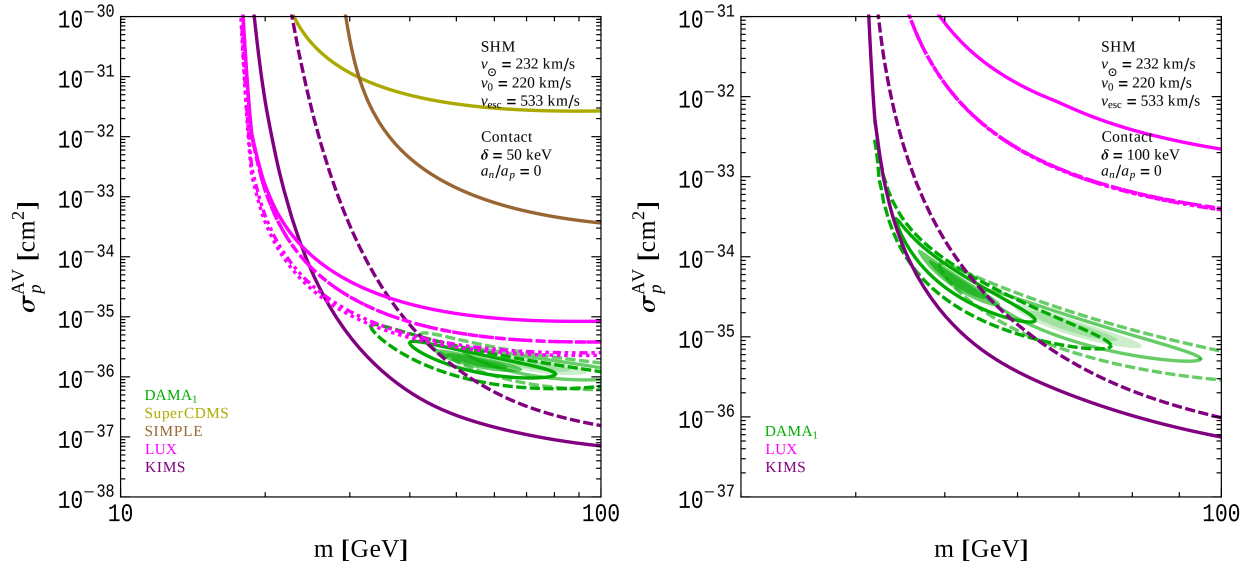

Figure 4.10. Same as Fig. 4.1 but for endothermic AV interactions with $\delta = 50$ keV (left) and $\delta = 100$ keV (right).

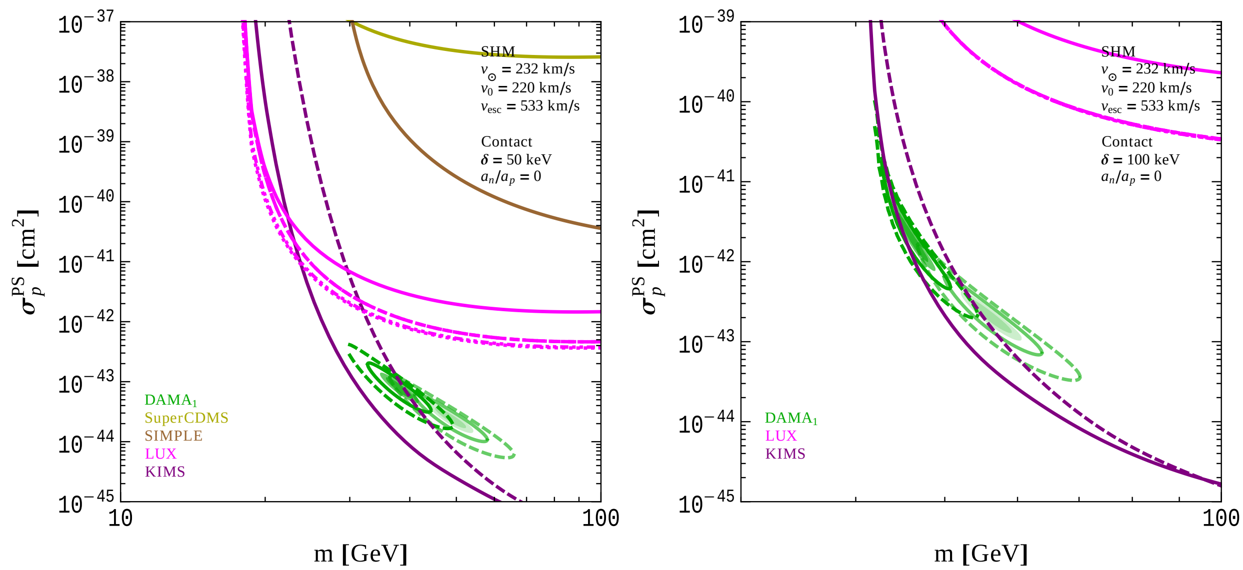

Figure 4.11. Same as Fig. 4.10 but for PS interactions.

independent analysis was performed on a series of effective operators. In Table V of [32] the AV and PS interactions correspond to fermion operators 15 and 4, respectively. For those interactions, [32] quotes best fit parameters for DAMA (corresponding to $\delta = 106$ keV for AV and $\delta = 57$ keV for PS) that are consistent with the KIMS data only for DAMA quenching factor 0.09 and KIMS quenching factor 0.05. In [32], however, scattering off Cs in KIMS was neglected due to the lack of the form factor in [92]. Since the contribution of

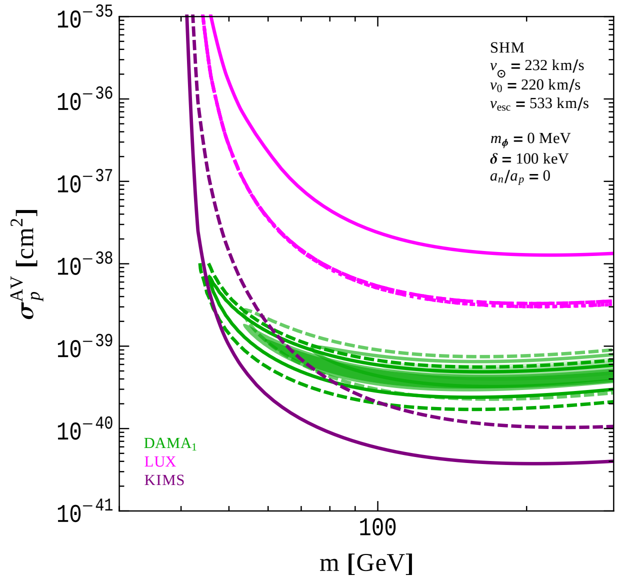

Figure 4.12. Same as Fig. 4.10 (right) but for a massless mediator.

Cs to the scattering rate is sizable for interaction with protons, we adopt an approximate form factor for Cs as discussed in Sec. 4.1.3, resulting in stronger KIMS bounds.

At this point it is important to recall the flavor physics bounds we mentioned in the introduction. Fig. 9 of [91] shows that the quark couplings needed for PS inelastic scattering on I to fit the DAMA data with a one-particle exchange process,

$$g\, g_{\rm DM} = \begin{cases} \kappa \left(\dfrac{m_\phi}{100 \text{ MeV}} \right)^2 & \text{for } m_\phi \gg 100 \text{ MeV} \\ \kappa' & \text{for } m_\phi \ll 100 \text{ MeV}, \end{cases} \tag{4.3.2}$$

where $\kappa \simeq 0.2$ and $\kappa' \simeq 0.1$ for $\delta = 50$ keV, and $\kappa \simeq 1.6$ and $\kappa' \simeq 0.7$ for $\delta = 100$ keV, is rejected [91] for any reasonable value of $g_{\rm DM}$ (unless $g_{\rm DM} > 10^5$). Note that the quark coupling used in [91] is $g/\sqrt{2}$.

4.3.6 Endothermic long-range interactions

For the AV interaction via a massless mediator shown in Fig. 4.12, only a very small portion of the I DAMA region with quenching factor 0.09 escapes the KIMS limit with quenching factor 0.05. Therefore, quite different quenching factors are needed for I in DAMA and KIMS to have the DAMA region escape the KIMS limit. Although quenching factors of a given element in different crystals can have different values in general, large differences may be questionable. Again, we do not plot the results for long-range PS interactions since these are qualitatively similar to those for contact AV interactions, as commented above.

4.4 Halo-independent analysis

So far we have assumed a particular model for the dark halo of our galaxy. It is however possible to compare direct detection data without making any assumption about the local density or velocity distribution of the dark matter particles [25, 34, 36, 43–51, 55, 70, 72, 77, 109–115] (in particular we follow the analysis of [25, 48, 50, 51]). This method was described in Sec. 1.3 and consists of extracting from the data, instead of just the (reference) WIMP-proton cross section σ_p, the function $\tilde{\eta}$ of $v_{\min}$ defined in (1.3.6) which encloses all the dependence of the rate on the DM velocity distribution. Since this function is experiment-independent, data from different experiments can be directly compared in the $v_{\min}$–$\tilde{\eta}$ plane.

In order to perform the halo-independent analysis we have to assume a value for the DM mass m, together with all the other interaction parameters such as the mass splitting δ and the neutron to proton coupling ratio a_n/a_p. We study parameter values that seem promising in our SHM analysis to make a DM interpretation of the DAMA data compatible with all other experiments when relaxing the assumption on the dark halo. Taking into account Figs. 4.2 and 4.3 we select a WIMP mass below 10 GeV, one close to 30 GeV, and one close to 50 GeV, for WIMPs with PS interactions and elastic scattering. For the couplings we take $a_n = 0$ rather than $a_n/a_p = -1/16.4$; this choice is conservative in the sense that, while results from experiments employing targets with negligible spin-dependent interactions with neutrons like DAMA, SIMPLE, PICASSO, and KIMS are not affected, the bounds from LUX and SuperCDMS are less constraining when the WIMP-neutron coupling is set to 0 (see e.g. Fig. 4.2). We do not consider inelastic exothermic scattering, as the DAMA regions are badly excluded in all cases studied in the previous section. For inelastic endothermic scattering, looking at Fig. 4.10 we select $m = 40$ GeV for $\delta = 50$ keV and $m = 52$ GeV for $\delta = 100$ keV, for WIMPs with AV interactions with $a_n = 0$. Analogously, from Fig. 4.11 we select $m = 38$ GeV for $\delta = 50$ keV and $m = 45$ GeV for $\delta = 100$ keV, for WIMPs with PS interactions with $a_n = 0$. Notice that some of these choices are similar to the best fit parameters of [32], i.e. $m = 54.3$ GeV and $\delta = 106$ keV for AV interactions and $m = 40.8$

GeV and $\delta = 57$ keV for PS interactions. Finally, from Fig. 4.12 we select $m = 80$ GeV for $\delta = 100$ keV, for long-range AV interactions with $a_n = 0$.

4.4.1 Data analysis

For LUX, SuperCDMS, and SIMPLE we follow the procedure developed and described in [25, 48, 50, 51]. For PICASSO and KIMS we cannot perform a Maximum Gap analysis as done for LUX and SuperCDMS because the data are binned. We therefore produce a limit on $\tilde{\eta}^0$ at each $v_{\rm min}$ value in the following way. We compute the rate (1.3.13) adopting a step function, $\tilde{\eta}^0(v_{\rm min}) = \tilde{\eta}^* \theta(v^*_{\rm min} - v_{\rm min})$, because it is the function that allows to draw the most conservative bound on the value $\tilde{\eta}^*$ taken by $\tilde{\eta}^0(v_{\rm min})$ at a specific $v_{\rm min}$ value $v^*_{\rm min}$ [43, 44]. For each value of $v^*_{\rm min}$ we compare this predicted rate in each single energy bin with the 90% CL limit on the rate. Imposing the computed rate not to surpass the limit in any of the bins thus fixes the maximum allowed $\tilde{\eta}^*$ at $v^*_{\rm min}$. For KIMS we use the black limit lines in Fig. 4 of [12], while for PICASSO we translate the upper end of the error bars in Fig. 5 of [6] into 90% CL upper limits assuming the data are Gaussian distributed and the uncertainty is given at the 1σ level.

The halo-independent analysis of the DAMA annual modulation data presented in [25, 48, 50, 51] and in [34] is only applicable when WIMPs can scatter off only one of the target elements, either Na or I. This happens, for instance, if the DM is so light that elastic scattering off I occurs always below threshold, assuming a reasonable maximum speed with respect to Earth, $v_{\rm max}$, for WIMPs in the galaxy. It also happens for inelastic endothermic scattering with $v_{\rm max} < v_\delta^{\rm Na} = \sqrt{2\delta/\mu_{\rm Na}}$, which makes WIMP scattering off Na kinematically forbidden. Therefore, we can straightforwardly apply the analysis of DAMA data presented in [25, 34, 48, 50, 51] to the light WIMP with $m \lesssim 10$ GeV scattering elastically and to all considered cases of endothermic scattering. The WIMPs with mass close to 30 GeV and 50 GeV scattering elastically need a special treatment, described in the following.

When both elements, Na and I, are involved in the scattering, the same value of the detected energy E' is mapped onto different $v_{\rm min}$ values because of the different target masses and quenching factors. In order to extract the value of $\tilde{\eta}$ in a $v_{\rm min}$ interval from (1.3.13), we adapt to the DAMA data the procedure that was developed for CRESST-II in Appendix A.2 of [44] and in [46]. We start by choosing the highest energy bin at high enough energy

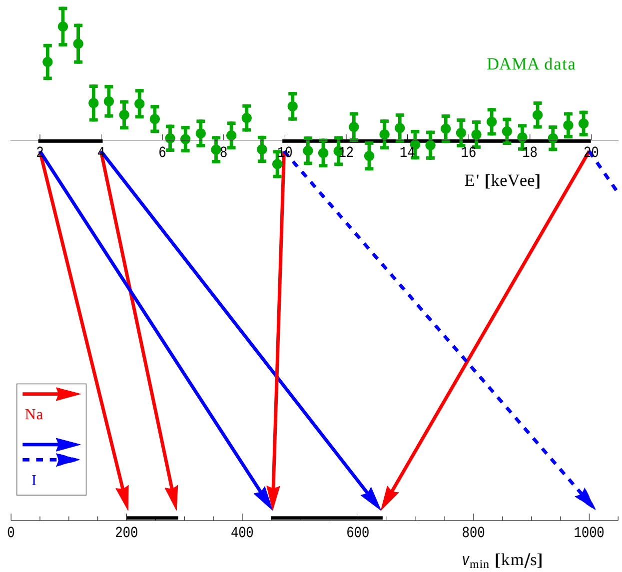

Figure 4.13. Binning scheme used for $m = 30.14$ GeV and elastic scattering. The red and blue arrows show the correspondence between average detected energies $\langle E' \rangle$, shown on the top axis, and minimum speeds $v_{\rm min}$, shown on the bottom axis, for Na and I targets, respectively. The dashed arrows show that WIMPs scattering off I could produce events in the highest energy bin only with $v_{\rm min} > v_{\rm max} = 800$ km/s. The DAMA data are overlaid in green.

so that the heaviest element (I) does not contribute to the scattering rate in it, because the necessary $v_{\rm min}$ exceeds the maximum possible speed in the halo. Starting from the highest energy bin we work our way toward the lowest energy bin as depicted in Fig. 4.13. We compute the $v_{\rm min}$ range corresponding to the highest E' bin for Na using the relation $\langle E' \rangle = Q_T E_R(v_{\rm min}, m_T)$ for T = Na (with $E_R(v_{\rm min}, m_T)$ given in (1.2.2)). From this $v_{\rm min}$ range we derive the second highest energy bin using again the same relation for T = I. The procedure can then be repeated starting from this new bin, until the lightest energy bin above the experimental threshold is built. Since we only wish to consider bins where a significant signal is observed, we require the lowest energy bin to lie within the 2.0–6.0 keVee interval, where the modulation amplitude measured by DAMA is significantly different from zero.

Notice that the DAMA modulation data span 2.0 to 20.0 keVee with an original bin size of 0.5 keVee. In rebinning the DAMA data we want to merge the original bins, and not split existing bins. Therefore, each new bin needs to have boundaries that are multiples of 0.5 keVee so as to encompass an entire number of original DAMA bins. Notice also that, if E' is the boundary of one of the chosen bins, the corresponding boundary of the next higher energy bin is rE' with $r \equiv Q_{\rm Na} E_R(v_{\rm min}, m_{\rm Na})/Q_{\rm I} E_R(v_{\rm min}, m_{\rm I}) = Q_{\rm Na}\mu_{\rm Na}^2 m_{\rm I}/Q_{\rm I}\mu_{\rm I}^2 m_{\rm Na}$. Therefore, it is necessary for r to be an integer (or a half-integer) number. For quenching factors that are constant in energy, this can be achieved for particular DM mass values. With $Q_{\rm Na} = 0.30$ and $Q_{\rm I} = 0.09$, we choose our DM particle masses to be 30.14 GeV and 47.35 GeV for which $r = 5.0$ and 3.5, respectively.

Choosing $v_{\rm max} = 800$ km/s, for $m = 30.14$ GeV the bin at highest E' must be completely above $Q_{\rm I} E_R(v_{\rm max}, m_{\rm I}) \simeq 6.3$ keVee for $Q_{\rm I} = 0.09$. Using $r = 5$ we take two bins, $[2.0, 4.0]$ keVee and $[10.0, 20.0]$ keVee. We choose bins well separated in energy and as large as possible to avoid overlapping and to minimize the effect of the tails of the corresponding response functions. The binning scheme for this candidate is shown in Fig. 4.13. Our choice of $m = 47.35$ GeV comes from a halo model in Fig. 4.3 with a low $v_{\rm max}$ value, close to $v_{\rm max} = 600$ km/s. Assuming this $v_{\rm max}$ value, scattering of I is kinematically forbidden for E' energies above $Q_I E_R(v_{\rm max}, m_{\rm I}) \simeq 6.97$ keVee for $Q_{\rm I} = 0.09$. Using $r = 3$ we choose the two bins $[3.0, 6.0]$ keVee and $[10.5, 21.0]$ keVee. Since the highest energy bin surpasses the 2.0–20.0 keVee energy range where the DAMA modulation data is available, for the two additional 0.5 keVee bins in the 20.0 to 21.0 keVee range we assume the same average and mean square error as for the nineteen 0.5 keVee bins in the 10.5–20.0 keVee range.

Once the energy bins to be used in the analysis are established, we extract information on the modulated component of the velocity integral, $\tilde{\eta}^1$, in the following way. For two bins $[E'_1, E'_2]$ and $[E'_3, E'_4]$ (the extension to a larger number of bins is trivial), (1.3.13) reads

$$\begin{aligned} R^1_{[E'_1,E'_2]} &= \int_0^\infty \mathrm{d}v_{\rm min}\, \tilde{\eta}^1(v_{\rm min}) \left[\mathcal{R}^{\rm Na}_{[E'_1,E'_2]}(v_{\rm min}) + \mathcal{R}^{\rm I}_{[E'_1,E'_2]}(v_{\rm min})\right] \\ &= \mathcal{A}^{\rm Na}_{[E'_1,E'_2]} \overline{\tilde{\eta}^{1,\,\rm Na}_{[E'_1,E'_2]}} + \mathcal{A}^{\rm I}_{[E'_1,E'_2]} \overline{\tilde{\eta}^{1,\,\rm I}_{[E'_1,E'_2]}}(v_{\rm min}) \end{aligned} \tag{4.4.1}$$

and

$$R^1_{[E'_3,E'_4]} = \int_0^\infty \mathrm{d}v_{\rm min}\, \tilde{\eta}^1(v_{\rm min}) \left[\mathcal{R}^{\rm Na}_{[E'_3,E'_4]}(v_{\rm min}) + \mathcal{R}^{\rm I}_{[E'_3,E'_4]}(v_{\rm min})\right] \simeq \mathcal{A}^{\rm Na}_{[E'_3,E'_4]} \overline{\tilde{\eta}^{1,\,\rm Na}_{[E'_3,E'_4]}}\ , \tag{4.4.2}$$

where scattering off I does not contribute to the rate in the highest energy bin by construction. Here we defined the target-specific average of $\tilde{\eta}^1_{[E'_1,E'_2]}$ as

$$\overline{\tilde{\eta}^{1,T}_{[E'_1,E'_2]}} \equiv \frac{\int_0^\infty \mathrm{d}v_{\min}\, \tilde{\eta}(v_{\min}) \mathcal{R}^T_{[E'_1,E'_2]}(v_{\min})}{\mathcal{A}^T_{[E'_1,E'_2]}} \,, \tag{4.4.3}$$

with

$$\mathcal{A}^T_{[E'_1,E'_2]} \equiv \int_0^\infty \mathrm{d}v_{\min}\, \mathcal{R}^T_{[E'_1,E'_2]}(v_{\min}) \,, \tag{4.4.4}$$

and analogous definitions for $[E'_3, E'_4]$. Since the two energy bins are chosen so that scattering off I in $[E'_1, E'_2]$ probes the same $v_{\min}$ range as scattering off Na in $[E'_3, E'_4]$, we expect that

$$\overline{\tilde{\eta}^{1,\,\mathrm{Na}}_{[E'_3,E'_4]}} \simeq \overline{\tilde{\eta}^{1,\,\mathrm{I}}_{[E'_1,E'_2]}} \,, \tag{4.4.5}$$

and thus that $\mathcal{R}^{\mathrm{Na}}_{[E'_3,E'_4]}(v_{\min})/\mathcal{A}^{\mathrm{Na}}_{[E'_3,E'_4]} \simeq \mathcal{R}^{\mathrm{I}}_{[E'_1,E'_2]}(v_{\min})/\mathcal{A}^{\mathrm{I}}_{[E'_1,E'_2]}$. Fig. 4.14 shows the comparison between these quantities for WIMPs with PS interactions and elastic scattering, and gives an idea of the extent to which the assumption in (4.4.5) is correct. In Fig. 4.14 we can see that the $v_{\min}$ range associated with a certain detected energy bin through the average relation $\langle E' \rangle = Q_T E_R(v_{\min}, m_T)$ determines only approximately the $v_{\min}$ range in which the corresponding response functions $\mathcal{R}^T(v_{\min})$ are significantly different from zero. The difference between the response functions of Na and I shown in Fig. 4.14 is due to the width of the energy resolution function, which depends on energy, and the $v_{\min}$ (or alternatively the E_R) dependence of the scattering cross section.

Finally, using (4.4.1), (4.4.2) and (4.4.5) we get the system of equations

$$\begin{cases} R^1_{[E'_1,E'_2]} = \mathcal{A}^{\mathrm{Na}}_{[E'_1,E'_2]} \overline{\tilde{\eta}^{1,\,\mathrm{Na}}_{[E'_1,E'_2]}} + \mathcal{A}^{\mathrm{I}}_{[E'_1,E'_2]} \overline{\tilde{\eta}^{1,\,\mathrm{I}}_{[E'_1,E'_2]}} \,, \\ R^1_{[E'_3,E'_4]} \simeq \mathcal{A}^{\mathrm{Na}}_{[E'_3,E'_4]} \overline{\tilde{\eta}^{1,\,\mathrm{Na}}_{[E'_3,E'_4]}} \simeq \mathcal{A}^{\mathrm{Na}}_{[E'_3,E'_4]} \overline{\tilde{\eta}^{1,\,\mathrm{I}}_{[E'_1,E'_2]}} \,, \end{cases} \tag{4.4.6}$$

which can be solved for $\overline{\tilde{\eta}^{1,\,\mathrm{Na}}_{[E'_1,E'_2]}}$ and $\overline{\tilde{\eta}^{1,\,\mathrm{I}}_{[E'_1,E'_2]}}$. We compute the 68% CL error on these quantities by propagating the 1σ uncertainty of the DAMA data.

Same as for the SHM analysis, the implementation of the halo-independent analysis can be found in the CoddsDM software [53].

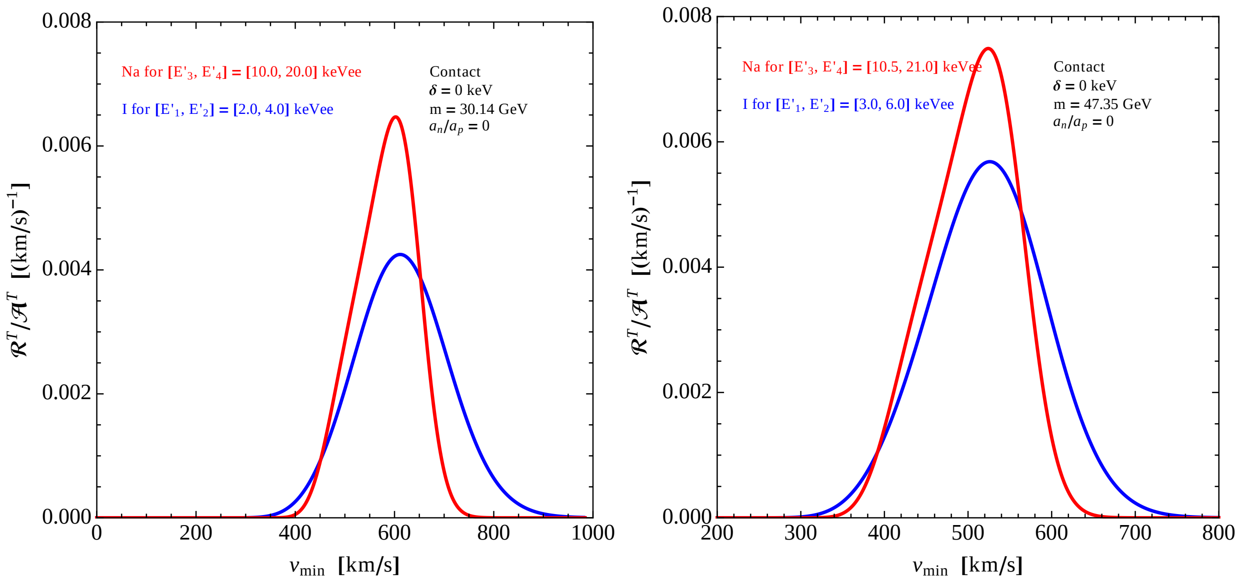

Figure 4.14. Normalized response functions $\mathcal{R}^T(v_{\min})/\mathcal{A}^T$ for WIMPs with PS interactions and elastic scattering, for DM mass $m = 30.14$ GeV (left) and $m = 47.35$ GeV (right). $\mathcal{R}^{\mathrm{Na}}_{[E'_3,E'_4]}(v_{\min})/\mathcal{A}^{\mathrm{Na}}_{[E'_3,E'_4]}$ is shown in red and $\mathcal{R}^{\mathrm{I}}_{[E'_1,E'_2]}(v_{\min})/\mathcal{A}^{\mathrm{I}}_{[E'_1,E'_2]}$ in blue.

4.5 Results of the halo-independent data comparison

The plots in Figs. 4.15–4.18 show 90% CL upper bounds on $\tilde{\eta}^0(v_{\min})$ from LUX, SuperCDMS, SIMPLE, PICASSO, and KIMS with $Q_{\mathrm{I}} = Q_{\mathrm{Cs}} = 0.10$ (solid purple line) and 0.05 (dashed purple line). The DAMA measurements of the annual modulation amplitude $\tilde{\eta}^1(v_{\min})$ are shown as crosses, where the vertical bars show the 68% CL uncertainty and are located at the position of the maximum of the relevant response functions $\mathcal{R}^T(v_{\min})$. The horizontal bar of each cross indicates the $v_{\min}$ interval where 90% of the integral of $\mathcal{R}^T(v_{\min})$ about the peak is included. When both Na and I contribute to a cross we choose the response function extended over the larger $v_{\min}$ interval, which is $\mathcal{R}^{\mathrm{I}}(v_{\min})$ (see Fig. 4.14). We assume the most commonly adopted values of the quenching factors, $Q_{\mathrm{Na}} = 0.30$ and $Q_{\mathrm{I}} = 0.09$.

For WIMPs with PS interactions and elastic scattering (see Fig. 4.15), we selected three masses from the DAMA regions shown in Figs. 4.2 and 4.3. We show results for $a_n = 0$, as explained above. Only scattering off Na is kinematically accessible in DAMA for $m = 7$ GeV (top panel of Fig. 4.15), since $E' > 2$ keVee would require $v_{\min} > 1644$ km/s for I

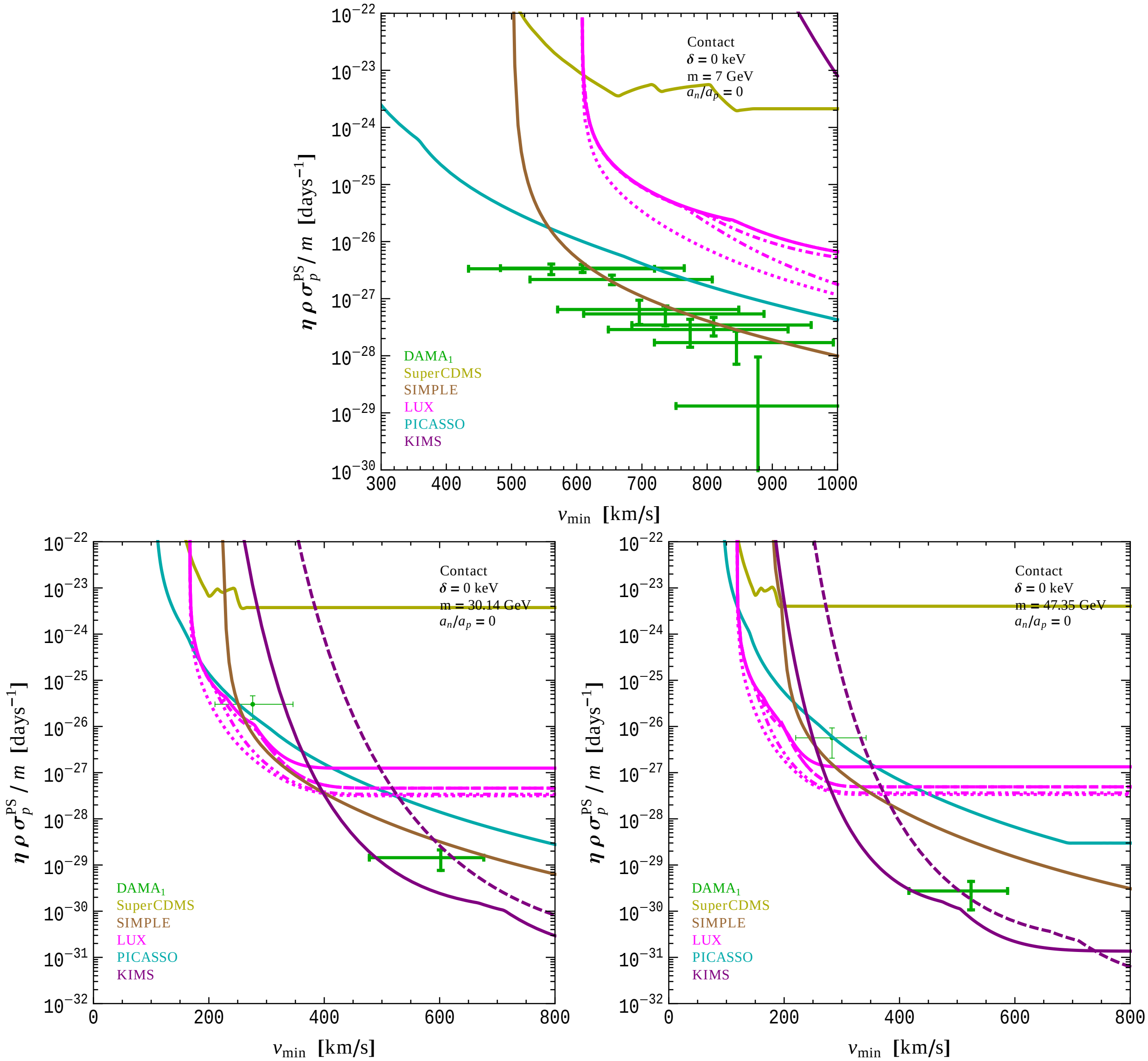

Figure 4.15. 90% CL upper bounds on $\tilde{\eta}^0(v_{\rm min})$ from LUX, SuperCDMS, SIMPLE, PICASSO, and KIMS, and measurements of $\tilde{\eta}^1(v_{\rm min})$ with 68% CL vertical error bars for DAMA with $Q_{\rm Na} = 0.30$, $Q_{\rm I} = 0.09$, for a WIMP with mass $m = 7$ GeV (top), $m = 30.14$ GeV (bottom left) and 47.35 GeV (bottom right), contact PS interactions and elastic scattering. Different line styles for the LUX bound correspond, from most constraining to least constraining, to 0, 1, 3, 5 and 24 observed events (see Section 4.2). The KIMS bound is shown for both $Q_{\rm I} = Q_{\rm Cs} = 0.10$ (solid line) and 0.05 (dashed line). The thin DAMA crosses show the absolute value of $\overline{\tilde{\eta}^1}$ when this is negative.

recoils. In this case the limits of PICASSO and SIMPLE cut across the DAMA points (each corresponding to the DAMA bins of width 0.5 keVee from 2.0 to 6.5 keVee), except for the highest energy bin. This shows incompatibility between the DAMA and the PICASSO and SIMPLE data, unless the modulation amplitude $|\tilde{\eta}^1(v_{\rm min})|$ can be as large as the time-average $\tilde{\eta}^0(v_{\rm min})$, which is not possible in the whole $v_{\rm min}$ range.

For the bottom panels of Fig. 4.15, where $m = 30.14$ GeV and 47.35 GeV, both I and

Na contribute (see above). Although these masses were chosen within the DAMA regions in our SHM analysis, the $\overline{\tilde{\eta}^1}$ crosses shown in the two panels correspond to a halo that significantly differs from the SHM. We obtained negative $\overline{\tilde{\eta}^1}$ values in the lowest $v_{\rm min}$ ranges in both cases, both of them above $v_{\rm min} = 200$ km/s, while in the SHM $\tilde{\eta}^1$ is negative only below the $v_{\rm min} = 200$ km/s value. The absolute value of the crosses with negative $\overline{\tilde{\eta}^1}$ values are shown in Fig. 4.15 with thinner lines than those with positive $\overline{\tilde{\eta}^1}$ values. In both cases the combination of KIMS, PICASSO, SIMPLE and LUX bounds reject the DAMA crosses, showing strong incompatibility between the DAMA result and the just mentioned limits.

Our results are similar to those of [114], although the halo-independent analysis done in this reference is different. In [114] the "minimal" $\tilde{\eta}^1(v_{\rm min})$ compatible with the 1σ DAMA error bars is identified with the piecewise continuous function touching the lower end of these error bars. Only the four 0.5 keVee experimental bins in the 2.0 to 4.0 keVee energy interval are considered. $\tilde{\eta}^1(v_{\rm min})$ is set to zero outside the $v_{\rm min}$ range corresponding to this E' range. This amounts to a choice of very low (m-dependent) $v_{\rm max}$. With this choice, the contribution of I can be neglected for $m \lesssim 60$ GeV. Besides, $\tilde{\eta}^0(v_{\rm min})$ is assumed to be equal to the "minimal" $\tilde{\eta}^1(v_{\rm min})$ in almost all the considered $v_{\rm min}$ bins. This implies the dark halo leading to this velocity integral is quite different from the SHM, as we also find. However, while our results seem similar to those of [114], we partially draw different conclusions. The authors of [114] conservatively conclude that their choice of $\tilde{\eta}^1$ and $\tilde{\eta}^0$ for DAMA can be compatible with the limits from other experiments for PS interactions with $m = 7$ and $m = 30$ GeV (while being rejected for AV interactions). This is because they allow $\tilde{\eta}^1(v_{\rm min})$ to be equal to $\tilde{\eta}^0(v_{\rm min})$ in almost the whole 2.0–4.0 keVee energy range. Assuming instead that $|\tilde{\eta}^1(v_{\rm min})|$ is much smaller than $\tilde{\eta}^0(v_{\rm min})$, as it happens in most halo models, the DM interpretation of the DAMA data is in strong tension with the limits.

Fig. 4.16 shows the result of our halo-independent analysis for WIMPs with AV interactions and inelastic endothermic scattering. The left panel is for $m = 40$ GeV and $\delta = 50$ keV, for which $v_\delta^{\rm Na} = 802.7$ km/s, and the right panel is for $m = 52$ GeV and $\delta = 100$ keV, for which $v_\delta^{\rm Na} = 1135.2$ km/s. Therefore, only scattering off I is kinematically allowed for $v_{\rm max} = 800$ km/s. The DAMA data seems in disagreement with the KIMS bound for $Q_{\rm I} = Q_{\rm Cs} = 0.10$, but not if $Q_{\rm I} = Q_{\rm Cs} = 0.05$ in KIMS (however, this last value is much smaller than the $Q_{\rm I} = 0.09$ taken for DAMA).

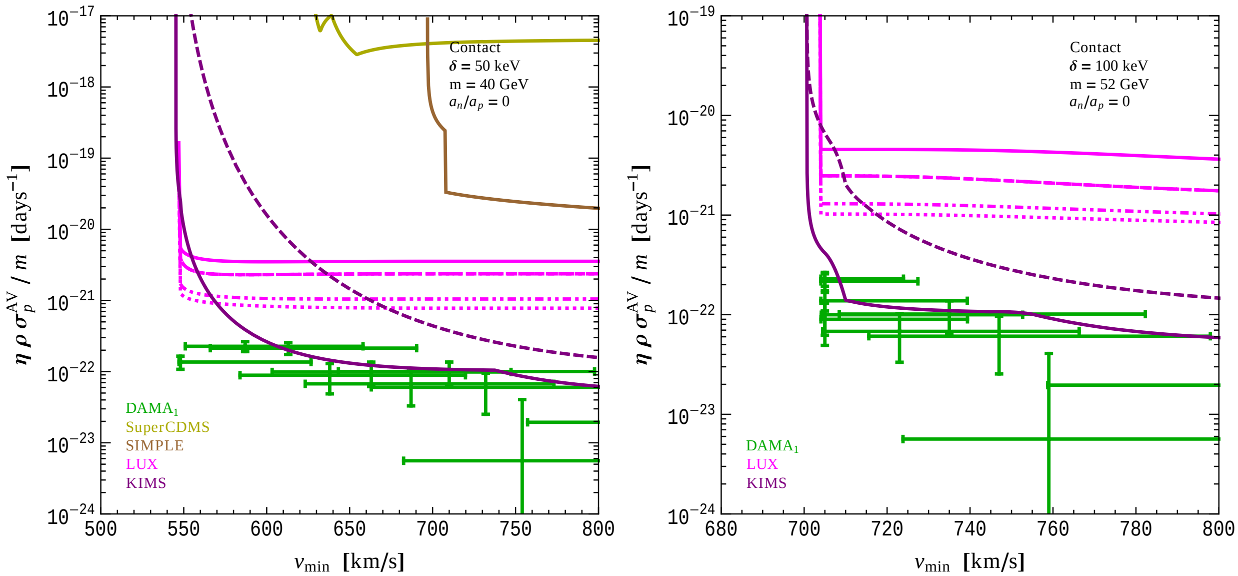

Figure 4.16. Same as Fig. 4.15 but for WIMPs with inelastic endothermic contact AV interactions and $m = 58$ GeV, $\delta = 50$ keV (left), and $m = 52$ GeV, $\delta = 100$ keV (right).

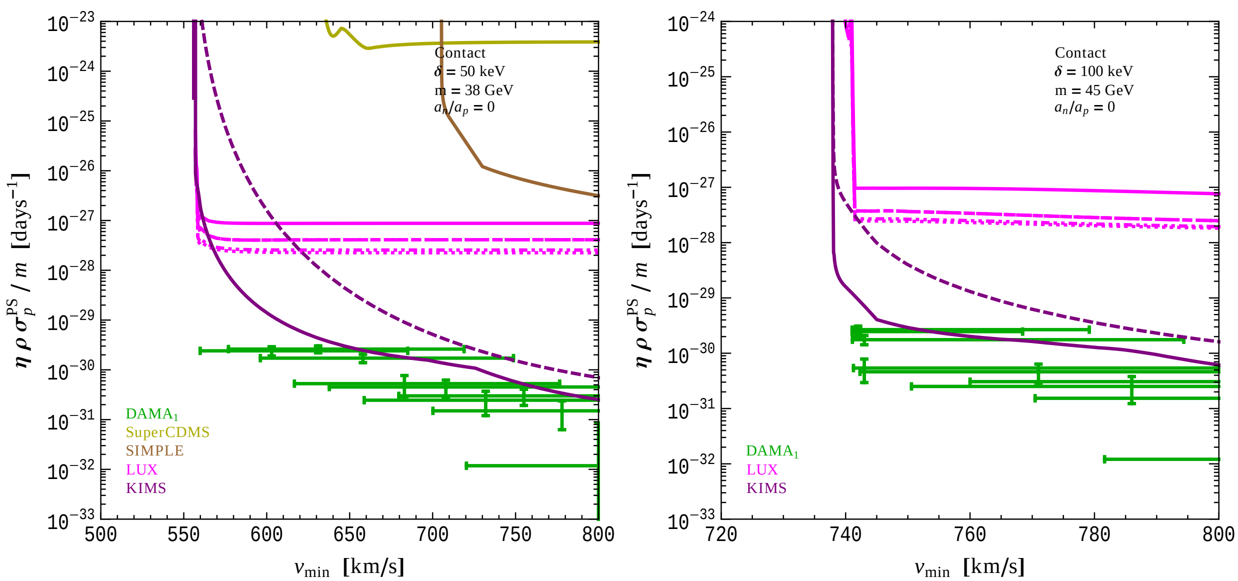

Figure 4.17. Same as Fig. 4.16 but for WIMPs with inelastic endothermic contact PS interactions and $m = 38$ GeV, $\delta = 50$ keV (left), and $m = 45$ GeV, $\delta = 100$ keV (right).

Fig. 4.17 shows the result of our halo-independent analysis for WIMPs with PS interactions and inelastic endothermic scattering, for $m = 38$ GeV and $\delta = 50$ keV in the left panel, resulting in $v_\delta^{\rm Na} = 810.1$ km/s, and $m = 45$ GeV and $\delta = 100$ keV in the right panel, resulting in $v_\delta^{\rm Na} = 1113.0$ km/s. WIMPs scattering off Na are again kinematically forbidden for $v_{\rm max} = 800$ km/s. The DAMA data are in disagreement with the KIMS bound, unless $Q_{\rm I} = Q_{\rm Cs} = 0.05$ and $|\tilde{\eta}^1(v_{\rm min})| \simeq \tilde{\eta}^0(v_{\rm min})$.

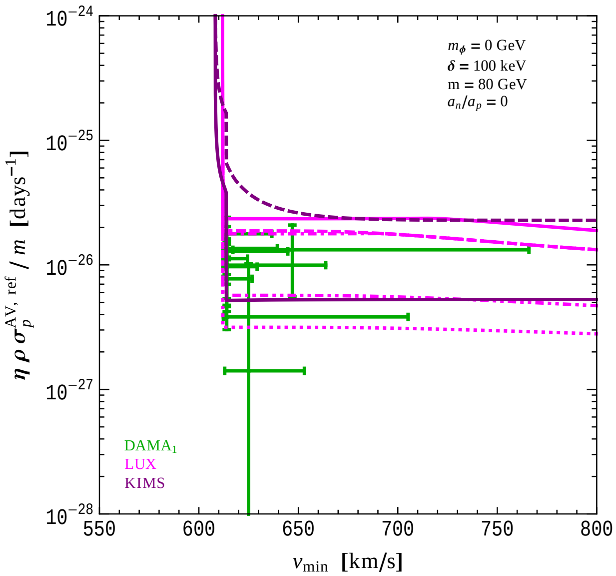

Figure 4.18. Same as Fig. 4.16 but for WIMPs with inelastic endothermic AV long-range interactions and $m = 80$ GeV, $\delta = 100$ keV.

Fig. 4.18 shows our results for a WIMP with AV interactions and long-range inelastic endothermic scattering. Here $m = 80$ GeV and $\delta = 100$ keV, thus $v_\delta^{\rm Na} = 1031.5$ km/s. The DAMA data are excluded by our most stringent KIMS ($Q_{\rm I} = Q_{\rm Cs} = 0.10$) and LUX bounds, but they remain in strong tension with the null results even when the less stringent KIMS and LUX bounds are considered.

4.6 Conclusions for Chapter 4

We investigated the possibility of interpreting the annual modulation signal observed in the DAMA experiment as due to WIMPs with spin-dependent coupling mostly to protons. We considered both an axial-vector (AV) interaction, which is what is usually referred to as 'spin-dependent interaction', and a pseudo-scalar (PS) interaction, proposed in [57] to reconcile DAMA with the null experiments. We also extended our analysis to inelastic scattering, and considered both contact and long-range interactions. Due to the similar E_R dependence of the differential cross sections, we find for the long-range PS interaction the same results as for contact AV interactions, up to a shift in σ_p. We analyzed the data both assuming the Standard Halo Model (SHM) and in a halo-independent manner.

Spin-dependent WIMP couplings mostly to protons effectively weaken the bounds from experiments using Xe and Ge as target elements, whose spin is due mostly to neutrons. However, the bounds from experiments with F and I targets, such as PICASSO, SIMPLE and KIMS, remain relevant since their spin is due mostly to protons.

Assuming the SHM, for elastic scattering (see Figs. 4.1 to 4.5) we found that, in all the cases investigated here, the DAMA regions for Na are entirely excluded by SIMPLE and PICASSO, while the regions for I are excluded by KIMS.

For exothermic scattering (see Figs. 4.6, 4.7 and 4.9), the DAMA regions move progressively to smaller WIMP masses with respect to the upper limits as $|\delta|$ increases, because the modulation phase observed by DAMA forces $v_{\rm min} > 200$ km/s, and this is possible only for progressively lighter WIMPs (see Fig. 4.8). Thus, exothermic scattering brings compatibility between the DAMA region for Na and the upper bounds from SIMPLE. However, it does not suppress the PICASSO limit which continues to rule out the DAMA region. Furthermore, exothermic scattering reduces the modulation amplitude with respect to the time-average rate. Thus, the upper limit derived from the DAMA average rate measurement rejects the interpretation of the signal as due to scattering off Na for values of $\delta < -30$ keV. The DAMA region for scattering off I is excluded by the SIMPLE and KIMS upper bounds.

For endothermic scattering (see Figs. 4.10 to 4.12), only KIMS provides relevant bounds. Scattering in all detectors besides KIMS and LUX becomes kinematically forbidden for large enough δ. We showed results for $\delta = 50$ and 100 keV, because as δ increases further, scattering off I becomes kinematically forbidden as well. For $\delta = 50$ keV, only assuming a larger quenching factor $Q_{\rm I} = 0.09$ for I in DAMA, and a smaller quenching factor $Q_{\rm I} = Q_{\rm Cs} = 0.05$ in KIMS, the allowed DAMA region is compatible with all present limits for PS couplings. However, the possibility that the same nuclide has such different quenching factors in different crystals may be questionable. The same holds for contact and long-range AV and long-range PS interactions for $\delta = 100$ keV. For contact PS interactions and $\delta = 100$ keV, a small sleeve of the 90% CL DAMA region for scattering off I escapes the 90% CL KIMS limit with similar $Q_{\rm I}$ for both experiments. These results are largely consistent with the results of [32]. However, for PS interactions the DAMA regions are rejected by flavor physics bounds on the PS coupling to quarks [91] (unless $g_{\rm DM}$ can be very large $g_{\rm DM} > 10^5$). In our analysis we assumed that the scattering process can be approximated by one-particle exchange. The inclusion of multi-particle exchange processes may change the form of the WIMP-nucleus scattering cross section, and therefore all bounds shall be reconsidered.

For WIMP mass values within the DAMA regions derived assuming the SHM and close to the upper limits rejecting them, we performed also a halo-independent analysis. This is presented in Fig. 4.15 for elastic scattering with contact PS interactions and in Figs. 4.16–4.18 for inelastic endothermic scattering with contact AV, contact PS, and long-range AV interactions. We again find strong tension between the DAMA data and upper bounds, except for contact AV and PS interactions with inelastic endothermic scattering if $Q_{\rm I}$ in KIMS is much smaller ($Q_{\rm I} = 0.05$) than the $Q_{\rm I} = 0.09$ assumed for DAMA, although this choice of different $Q_{\rm I}$ values for both experiments may be questionable.

CHAPTER 5

Conclusions and Present Status of Potential DM Signals

We have explored the compatibility between the potential signals of CDMS-II-Si and DAMA with the null results from the other direct dark matter (DM) detection experiments, for different types of DM candidates, both assuming the Standard Halo Model (SHM) and in a halo-independent manner, and we have presented new or extended halo-independent data analysis methods.

First, we presented comparisons of direct DM detection data for light WIMPs with inelastic exothermic scattering. We found that the CDMS-II-Si signal region can still be compatible with all present upper bounds for exothermic scattering and spin-independent (SI) isospin-violating interactions. Exothermic scattering favors light targets and weakens the Xe-based limits, the most restrictive of which is at present the LUX limit. We found that the CDMS-II-Si region becomes allowed by LUX, but is rejected by the SuperCDMS limit for isospin-conserving interactions. Considering in addition an isospin-violating coupling, in particular one with a neutron to proton coupling ratio of -0.8 (Ge-phobic) which maximally reduces the WIMP-Ge coupling, allows the CDMS-II-Si regions to become compatible with all upper bounds.

Next, we have expanded and corrected a recently proposed extended maximum halo-independent (EHI) method to analyze unbinned direct DM detection data. An earlier version of this method was introduced in [55], which used the recoil energy E_R as an independent variable. Instead, we use $v_{\min}$, the minimum speed a DM particle must have in order to impart a given recoil energy E_R to the nucleus, which allows us to apply the method to any type of target composition and interaction, including general momentum and velocity dependence, and elastic and inelastic scattering. We have proved the method and rigorously defined a two-sided pointwise confidence band with a clear statistical meaning, which allows to quantitatively assess the compatibility of the unbinned data with upper limits of other experiments, at given confidence levels.

We applied this method to the three candidate events found by CDMS-II-Si for SI interactions with either elastic or inelastic exothermic scattering, and with different neutron to proton coupling ratios f_n/f_p. We found that the WIMP interpretation of the CDMS-II-Si signal is compatible with all upper bounds for elastic scattering and $f_n/f_p = -0.7$ (Xe-phobic), as well as for inelastic exothermic scattering (for mass differences $\delta = -50$ and -200 keV) and $f_n/f_p = -0.8$ (Ge-Phobic).

Finally, we examined the interpretation of the annual modulation signal observed in the DAMA experiment as due to WIMPs with spin-dependent coupling mostly to protons. We considered both an axial-vector (AV) interaction, which what is usually referred to as "spin-dependent interaction", and a pseudo-scalar (PS) interaction. The PS interaction had previously been proposed in [57], who employed a Bayesian analysis, and claimed that for contact interactions and elastic scattering, the DAMA data is reconciled with the null results of other experiments at the 99% credible level. We considered both elastic and inelastic scattering, and contact and long-range interactions. Spin-dependent coupling mostly to protons weakens the upper bounds from experiments using target elements whose spin is mostly due to neutrons, such as Xe and Ge. However, experiments such as PICASSO, SIMPLE, and KIMS remain relevant, since they contain F, I and Cs which have an unpaired proton. For elastic and exothermic scattering, we found that in all cases the DAMA regions are excluded by a combination of the SIMPLE, PICASSO, and KIMS upper bounds.

Endothermic scattering favors heavier targets, enhancing scattering off I in DAMA compared to lighter targets such as Ge in SuperCDMS, and in addition it enhances the annual modulation amplitude. Scattering in all detectors besides KIMS and LUX becomes kinematically forbidden for large enough mass split δ. We found that for exothermic scattering the DAMA regions for I are in strong tension with the KIMS upper bounds, and the allowed DAMA regions are compatible only assuming a larger quenching factor for I in the NaI crystal (used in DAMA) and a smaller quenching factor for I in the CsI crystal (used in KIMS). However, the possibility that the same nuclide has such different quenching factors in different crystals may be questionable.

We also performed a halo-independent analysis. For elastic scattering, we extended the halo-independent method to analyze the DAMA data when both target elements, Na and I, are involved in the scattering. For endothermic scattering, we only included scattering of I (since for the values considered here, scattering of Na is kinematically forbidden). We again found strong tension between the DAMA data and the upper bounds, except for endothermic scattering and contact AV or PS interactions with a larger quenching factor for I in DAMA and a smaller quenching factor for I in KIMS, although this choice of quenching factors may be questionable.

References

[1] J. Angle *et al.* [XENON10 Collaboration], *A search for light dark matter in XENON10 data,* Phys. Rev. Lett. **107** (2011) 051301 [arXiv:1104.3088 [astro-ph.CO]].

[2] E. Aprile *et al.* [XENON100 Collaboration], *Dark Matter Results from 100 Live Days of XENON100 Data,* Phys. Rev. Lett. **107** (2011) 131302. [arXiv:1104.2549 [astro-ph.CO]].

[3] E. Aprile *et al.* [XENON100 Collaboration], *Dark Matter Results from 225 Live Days of XENON100 Data,* Phys. Rev. Lett. **109** (2012) 181301 [arXiv:1207.5988 [astro-ph.CO]].

[4] Z. Ahmed *et al.* [CDMS-II Collaboration], *Results from a Low-Energy Analysis of the CDMS II Germanium Data,* Phys. Rev. Lett. **106**, (2011) 131302 [arXiv:1011.2482 [astro-ph.CO]].

[5] M. Felizardo *et al.* [SIMPLE-II Collaboration], *Final Analysis and Results of the Phase II SIMPLE Dark Matter Search,* Phys. Rev. Lett. **108** (2012) 201302 [arXiv:1106.3014 [astro-ph.CO]].

[6] S. Archambault *et al.* [PICASSO Collaboration], *Constraints on Low-Mass WIMP Interactions on ^{19}F from PICASSO,* Phys. Lett. B **711** (2012) 153 [arXiv:1202.1240 [hep-ex]].

[7] E. Behnke *et al.* [COUPP Collaboration], *First Dark Matter Search Results from a 4-kg CF_3I Bubble Chamber Operated in a Deep Underground Site,* Phys. Rev. D **86** (2012) 052001 [arXiv:1204.3094 [astro-ph.CO]].

[8] Z. Ahmed *et al.* [CDMS Collaboration], *Search for annual modulation in low-energy CDMS-II data,* arXiv:1203.1309 [astro-ph.CO].

[9] R. Agnese *et al.*, *CDMSlite: A Search for Low-Mass WIMPs using Voltage-Assisted Calorimetric Ionization Detection in the SuperCDMS Experiment,* arXiv:1309.3259 [physics.ins-det].

[10] D. S. Akerib *et al.* [LUX Collaboration], *First results from the LUX dark matter experiment at the Sanford Underground Research Facility,* arXiv:1310.8214 [astro-ph.CO].

[11] R. Agnese *et al.* [SuperCDMS Collaboration], *Search for Low-Mass WIMPs with SuperCDMS,* Phys. Rev. Lett. **112** (2014) 241302 [arXiv:1402.7137 [hep-ex]].

[12] S. C. Kim *et al.*, *New Limits on Interactions between Weakly Interacting Massive Particles and Nucleons Obtained with CsI(Tl) Crystal Detectors,* Phys. Rev. Lett. **108** (2012) 181301 [arXiv:1204.2646 [astro-ph.CO]].

[13] R. Bernabei *et al.* [DAMA Collaboration], *Dark matter search,* Riv. Nuovo Cim. **26N1** (2003) 1 [arXiv:astro-ph/0307403].

[14] R. Bernabei *et al.* [DAMA Collaboration], *First results from DAMA/LIBRA and the combined results with DAMA/NaI,* Eur. Phys. J. C **56** (2008) 333 [arXiv:0804.2741 [astro-ph]].

[15] R. Bernabei *et al.* [DAMA and LIBRA Collaborations], *New results from DAMA/LIBRA,* Eur. Phys. J. C **67** (2010) 39 [arXiv:1002.1028 [astro-ph.GA]].

[16] R. Bernabei *et al.*, *Final model independent result of DAMA/LIBRA-phase1,* Eur. Phys. J. C **73** (2013) 12, 2648 [arXiv:1308.5109 [astro-ph.GA]].

[17] C. E. Aalseth *et al.* [CoGeNT Collaboration], *Results from a Search for Light-Mass Dark Matter with a P-type Point Contact Germanium Detector,* Phys. Rev. Lett. **106** (2011) 131301 [arXiv:1002.4703 [astro-ph.CO]].

[18] C. E. Aalseth *et al.* [CoGeNT Collaboration], *Search for an Annual Modulation in a P-type Point Contact Germanium Dark Matter Detector,* Phys. Rev. Lett. **107** (2011) 141301 [arXiv:1106.0650 [astro-ph.CO]].

[19] C. E. Aalseth *et al.* [CoGeNT Collaboration], *CoGeNT: A Search for Low-Mass Dark Matter using p-type Point Contact Germanium Detectors,* Phys. Rev. D **88** (2013) 012002 [arXiv:1208.5737 [astro-ph.CO]].

[20] C. E. Aalseth *et al.* [CoGeNT Collaboration], *Search for An Annual Modulation in Three Years of CoGeNT Dark Matter Detector Data,* arXiv:1401.3295 [astro-ph.CO].

[21] C. E. Aalseth *et al.* [CoGeNT Collaboration], *Maximum Likelihood Signal Extraction Method Applied to 3.4 years of CoGeNT Data,* arXiv:1401.6234 [astro-ph.CO].

[22] R. Agnese *et al.* [CDMS Collaboration], *Dark Matter Search Results Using the Silicon Detectors of CDMS II,* [arXiv:1304.4279 [hep-ex]].

[23] G. Angloher *et al.* [CRESST-II Collaboration], *Results on low mass WIMPs using an upgraded CRESST-II detector,* Eur. Phys. J. C **74** (2014) 12, 3184 [arXiv:1407.3146 [astro-ph.CO]].

[24] G. Angloher *et al.*, *Results from 730 kg days of the CRESST-II Dark Matter Search,* Eur. Phys. J. C **72** (2012) 1971 [arXiv:1109.0702 [astro-ph.CO]].

[25] E. Del Nobile, G. B. Gelmini, P. Gondolo and J. H. Huh, *Update on the Halo-Independent Comparison of Direct Dark Matter Detection Data,* Phys. Procedia **61** (2015) 45 [arXiv:1405.5582 [hep-ph]].

[26] D. Tucker-Smith and N. Weiner, *Inelastic dark matter,* Phys. Rev. D **64** (2001) 043502 [hep-ph/0101138].

[27] D. Tucker-Smith and N. Weiner, *The Status of inelastic dark matter,* Phys. Rev. D **72** (2005) 063509 [hep-ph/0402065].

[28] S. Chang, G. D. Kribs, D. Tucker-Smith and N. Weiner, *Inelastic Dark Matter in Light of DAMA/LIBRA,* Phys. Rev. D **79** (2009) 043513 [arXiv:0807.2250 [hep-ph]].

[29] J. March-Russell, C. McCabe and M. McCullough, *Inelastic Dark Matter, Non-Standard Halos and the DAMA/LIBRA Results,* JHEP **0905** (2009) 071 [arXiv:0812.1931 [astro-ph]].

[30] Y. Cui, D. E. Morrissey, D. Poland and L. Randall, *Candidates for Inelastic Dark Matter,* JHEP **0905** (2009) 076 [arXiv:0901.0557 [hep-ph]].

[31] S. Chang, N. Weiner and I. Yavin, *Magnetic Inelastic Dark Matter,* Phys. Rev. D **82** (2010) 125011 [arXiv:1007.4200 [hep-ph]].

[32] G. Barello, S. Chang and C. A. Newby, *A Model Independent Approach to Inelastic Dark Matter Scattering,* Phys. Rev. D **90** (2014) 9, 094027 [arXiv:1409.0536 [hep-ph]].

[33] P. W. Graham, R. Harnik, S. Rajendran and P. Saraswat, *Exothermic Dark Matter,* Phys. Rev. D **82** (2010) 063512 [arXiv:1004.0937 [hep-ph]].

[34] G. B. Gelmini, A. Georgescu and J. H. Huh, *Direct detection of light "Ge-phobic" exothermic dark matter,* JCAP **1407** (2014) 028 [arXiv:1404.7484 [hep-ph]].

[35] B. Batell, M. Pospelov and A. Ritz, *Direct Detection of Multi-component Secluded WIMPs,* Phys. Rev. D **79** (2009) 115019 [arXiv:0903.3396 [hep-ph]].

[36] M. T. Frandsen, F. Kahlhoefer, C. McCabe, S. Sarkar and K. Schmidt-Hoberg, *The unbearable lightness of being: CDMS versus XENON,* JCAP **1307** (2013) 023 [arXiv:1304.6066 [hep-ph]].

[37] M. McCullough and L. Randall, *Exothermic Double-Disk Dark Matter,* JCAP **1310**, 058 (2013) [arXiv:1307.4095 [hep-ph]].

[38] P. J. Fox, G. Jung, P. Sorensen and N. Weiner, *Dark Matter in Light of LUX,* arXiv:1401.0216 [hep-ph].

[39] M. T. Frandsen and I. M. Shoemaker, *The Up-Shot of Inelastic Down-Scattering at CDMS-Si,* arXiv:1401.0624 [hep-ph].

[40] D. P. Finkbeiner and N. Weiner, *Exciting Dark Matter and the INTEGRAL/SPI 511 keV signal,* Phys. Rev. D **76** (2007) 083519 [astro-ph/0702587].

[41] N. Arkani-Hamed, D. P. Finkbeiner, T. R. Slatyer and N. Weiner, *A Theory of Dark Matter,* Phys. Rev. D **79**, 015014 (2009) [arXiv:0810.0713 [hep-ph]].

[42] R. Essig, J. Kaplan, P. Schuster and N. Toro, *On the Origin of Light Dark Matter Species,* [arXiv:1004.0691 [hep-ph]].

[43] P. J. Fox, J. Liu and N. Weiner, *Integrating Out Astrophysical Uncertainties,* Phys. Rev. D **83** (2011) 103514. [arXiv:1011.1915 [hep-ph]].

[44] M. T. Frandsen *et al.*, *Resolving astrophysical uncertainties in dark matter direct detection,* JCAP **1201** (2012) 024 [arXiv:1111.0292 [hep-ph]].

[45] J. Herrero-Garcia, T. Schwetz and J. Zupan, *On the annual modulation signal in dark matter direct detection,* JCAP **1203** (2012) 005 [arXiv:1112.1627 [hep-ph]].

[46] P. Gondolo and G. B. Gelmini, *Halo independent comparison of direct dark matter detection data,* JCAP **1212**, (2012) 015 [arXiv:1202.6359 [hep-ph]].

[47] J. Herrero-Garcia, T. Schwetz and J. Zupan, *Astrophysics independent bounds on the annual modulation of dark matter signals,* Phys. Rev. Lett. **109** (2012) 141301 [arXiv:1205.0134 [hep-ph]].

[48] E. Del Nobile, G. B. Gelmini, P. Gondolo and J. -H. Huh, *Halo-independent analysis of direct detection data for light WIMPs,* arXiv:1304.6183 [hep-ph].

[49] N. Bozorgnia, J. Herrero-Garcia, T. Schwetz and J. Zupan, *Halo-independent methods for inelastic dark matter scattering,* JCAP **1307** (2013) 049 [arXiv:1305.3575 [hep-ph]].

[50] E. Del Nobile, G. Gelmini, P. Gondolo and J. -H. Huh, *Generalized Halo Independent Comparison of Direct Dark Matter Detection Data,* JCAP **1310** (2013) 048 [arXiv:1306.5273 [hep-ph]].

[51] E. Del Nobile, G. B. Gelmini, P. Gondolo and J. H. Huh, *Update on Light WIMP Limits: LUX, lite and Light,* JCAP **1403** (2014) 014 [arXiv:1311.4247 [hep-ph]].

[52] E. Del Nobile, G. B. Gelmini, P. Gondolo and J. H. Huh, *Direct detection of Light Anapole and Magnetic Dipole DM,* JCAP **1406** (2014) 002 [arXiv:1401.4508 [hep-ph]].

[53] A. Georgescu, *CoddsDM: Comparing data from direct searches for Dark Matter,* GitHub repository (2015), https://github.com/Andreea-G/Codds_DarkMatter

[54] G. B. Gelmini, A. Georgescu, P. Gondolo and J. H. Huh, *Extended Maximum Likelihood Halo-independent Analysis of Dark Matter Direct Detection Data,* JCAP **1511**, no. 11, 038 (2015) [arXiv:1507.03902 [hep-ph]].

[55] P. J. Fox, Y. Kahn and M. McCullough, *Taking Halo-Independent Dark Matter Methods Out of the Bin,* JCAP **1410**, no. 10, 076 (2014) [arXiv:1403.6830 [hep-ph]].

[56] E. Del Nobile, G. B. Gelmini, A. Georgescu and J. H. Huh, *Reevaluation of spin-dependent WIMP-proton interactions as an explanation of the DAMA data,* JCAP **1508**, no. 08, 046 (2015) [arXiv:1502.07682 [hep-ph]].

[57] C. Arina, E. Del Nobile and P. Panci, *Dark Matter with Pseudoscalar-Mediated Interactions Explains the DAMA Signal and the Galactic Center Excess,* Phys. Rev. Lett. **114** (2015) 011301 [arXiv:1406.5542 [hep-ph]].

[58] R. H. Helm, *Inelastic and Elastic Scattering of 187-Mev Electrons from Selected Even-Even Nuclei,* Phys. Rev. **104** (1956) 1466.

[59] T. Piffl *et al.*, *The RAVE survey: the Galactic escape speed and the mass of the Milky Way,* Astron. Astrophys. **562** (2014) A91 [arXiv:1309.4293 [astro-ph.GA]].

[60] R. Schoenrich, J. Binney and W. Dehnen, *Local Kinematics and the Local Standard of Rest,* Mon. Not. Roy. Astron. Soc. **403** (2010) 1829 [arXiv:0912.3693 [astro-ph.GA]].

[61] R. Bernabei *et al.*, *Dark Matter investigation by DAMA at Gran Sasso,* Int. J. Mod. Phys. A **28**, 1330022 (2013) [arXiv:1306.1411 [astro-ph.GA]].

[62] G. Gelmini and P. Gondolo, *DAMA dark matter detection compatible with other searches,* arXiv:hep-ph/0405278; P. Gondolo and G. Gelmini, *Compatibility of DAMA dark matter detection with other searches,* Phys. Rev. D **71** (2005) 123520 [arXiv:hep-ph/0504010].

[63] C. Savage, G. Gelmini, P. Gondolo and K. Freese, *Compatibility of DAMA/LIBRA dark matter detection with other searches,* JCAP **0904** (2009) 010 [arXiv:0808.3607 [astro-ph]].

[64] R. Agnese *et al.* [SuperCDMSSoudan Collaboration], *CDMSlite: A Search for Low-Mass WIMPs using Voltage-Assisted Calorimetric Ionization Detection in the SuperCDMS Experiment,* Phys. Rev. Lett. **112** (2014) 041302 [arXiv:1309.3259 [physics.ins-det]].

[65] A. Kurylov and M. Kamionkowski, Phys. Rev. D **69** (2004) 063503 [hep-ph/0307185].

[66] J. L. Feng, J. Kumar, D. Marfatia and D. Sanford, Phys. Lett. B **703** (2011) 124 [arXiv:1102.4331 [hep-ph]].

[67] R. J. Barlow, *Extended maximum likelihood,* Nucl. Instrum. Meth. A **297** (1990) 496.

[68] S. Yellin, *Finding an upper limit in the presence of unknown background,* Phys. Rev. D **66** (2002) 032005 [physics/0203002].

[69] G. J. Feldman and R. D. Cousins, *A Unified approach to the classical statistical analysis of small signals,* Phys. Rev. D **57** (1998) 3873 [physics/9711021 [physics.data-an]].

[70] B. Feldstein and F. Kahlhoefer, *Quantifying (dis)agreement between direct detection experiments in a halo-independent way,* JCAP **1412** (2014) 12, 052 [arXiv:1409.5446 [hep-ph]].

[71] M. Maltoni and T. Schwetz, *Testing the statistical compatibility of independent data sets,* Phys. Rev. D **68** (2003) 033020 [hep-ph/0304176].

[72] B. Feldstein and F. Kahlhoefer, *A new halo-independent approach to dark matter direct detection analysis,* JCAP **1408** (2014) 065 [arXiv:1403.4606 [hep-ph]].

[73] N. Bozorgnia and T. Schwetz, *What is the probability that direct detection experiments have observed Dark Matter?,* JCAP **1412** (2014) 12, 015 [arXiv:1410.6160 [astro-ph.CO]].

[74] W. Karush, *Minima of functions of several variables with inequalities as side constraints,* Masters thesis, University of Chicago, 1939.

[75] H. Kuhn and A. Tucker, *Nonlinear programming, in Proceedings of 2nd Berekely Symposium,* (U. of California Press, ed.), vol. MR 47303, pp. 481-492, 1951.

[76] S. Chang, J. Liu, A. Pierce, N. Weiner and I. Yavin, JCAP **1008** (2010) 018 [arXiv:1004.0697 [hep-ph]].

[77] S. Scopel and K. Yoon, *A systematic halo-independent analysis of direct detection data within the framework of Inelastic Dark Matter,* JCAP **1408** (2014) 060 [arXiv:1405.0364 [astro-ph.CO]].

[78] M. Burger, *Infinite-Dimensional Optimization and Optimal Design,* Available at: `ftp://ftp.math.ucla.edu/pub/camreport/cam04-11.pdf`

[79] A. Ya. Dubovitskii, A. A. Milyutin, USSR Comp. Math. Math. Phys. 5(3), 1 (1965) [Zh. Vychisl. Mat. Mat. Fiz. 5(3) 395 (1965)]

[80] R. B. Holmes, *A Course on Optimization and Best Approximation* (Springer, Berlin, 1972)

[81] K. A. Olive *et al.* [Particle Data Group Collaboration], *Review of Particle Physics,* Chin. Phys. C **38**, 090001 (2014).

[82] S. S. Wilks, *The Large-Sample Distribution of the Likelihood Ratio for Testing Composite Hypotheses,* Annals Math. Statist. **9** (1938) 1, 60.

[83] S. A. Murphy, A. W. van der Vaart, *On Profile Likelihood,* Journal of the American Statistical Association, Vol. 95, No. 450. (Jun., 2000), pp. 449-465

[84] R. Agnese *et al.* [SuperCDMS Collaboration], *Maximum Likelihood Analysis of Low Energy CDMS II Germanium Data,* Phys. Rev. D [Phys. Rev. D **91**, 052021 (2015)] [arXiv:1410.1003 [astro-ph.CO]].

[85] R. Agnese *et al.* [SuperCDMS Collaboration], *Improved WIMP-search reach of the CDMS II germanium data,* [arXiv:1504.05871 [hep-ex]].

[86] E. Del Nobile, C. Kouvaris, P. Panci, F. Sannino and J. Virkajarvi, *Light Magnetic Dark Matter in Direct Detection Searches,* JCAP **1208** (2012) 010 [arXiv:1203.6652 [hep-ph]].

[87] P. Ullio, M. Kamionkowski and P. Vogel, *Spin dependent WIMPs in DAMA?,* JHEP **0107** (2001) 044 [hep-ph/0010036].

[88] J. Kopp, T. Schwetz and J. Zupan, *Global interpretation of direct Dark Matter searches after CDMS-II results,* JCAP **1002** (2010) 014 [arXiv:0912.4264 [hep-ph]].

[89] G. Hiller, *B physics signals of the lightest CP odd Higgs in the NMSSM at large tan beta,* Phys. Rev. D **70**, 034018 (2004) [hep-ph/0404220].

[90] S. Andreas, O. Lebedev, S. Ramos-Sanchez and A. Ringwald, *Constraints on a very light CP-odd Higgs of the NMSSM and other axion-like particles,* JHEP **1008**, 003 (2010) [arXiv:1005.3978 [hep-ph]].

[91] M. J. Dolan, C. McCabe, F. Kahlhoefer and K. Schmidt-Hoberg, *A taste of dark matter: Flavour constraints on pseudoscalar mediators,* arXiv:1412.5174 [hep-ph].

[92] A. L. Fitzpatrick, W. Haxton, E. Katz, N. Lubbers and Y. Xu, *The Effective Field Theory of Dark Matter Direct Detection,* JCAP **1302** (2013) 004 [arXiv:1203.3542 [hep-ph]].

[93] M. Cirelli, E. Del Nobile and P. Panci, *Tools for model-independent bounds in direct dark matter searches,* JCAP **1310** (2013) 019 [arXiv:1307.5955 [hep-ph]].

[94] C. Boehm, M. J. Dolan, C. McCabe, M. Spannowsky and C. J. Wallace, *Extended gamma-ray emission from Coy Dark Matter,* JCAP **1405** (2014) 009 [arXiv:1401.6458 [hep-ph]].

[95] M. Freytsis and Z. Ligeti, *On dark matter models with uniquely spin-dependent detection possibilities,* Phys. Rev. D **83** (2011) 115009 [arXiv:1012.5317 [hep-ph]].

[96] H. Y. Cheng and C. W. Chiang, *Revisiting Scalar and Pseudoscalar Couplings with Nucleons,* JHEP **1207** (2012) 009 [arXiv:1202.1292 [hep-ph]].

[97] J. Engel, S. Pittel and P. Vogel, *Nuclear physics of dark matter detection,* Int. J. Mod. Phys. E **1** (1992) 1.

[98] M. T. Ressell, M. B. Aufderheide, S. D. Bloom, K. Griest, G. J. Mathews and D. A. Resler, *Nuclear shell model calculations of neutralino - nucleus cross-sections for Si-29 and Ge-73,* Phys. Rev. D **48** (1993) 5519.

[99] G. Belanger, F. Boudjema, A. Pukhov and A. Semenov, *Dark matter direct detection rate in a generic model with micrOMEGAs 2.2,* Comput. Phys. Commun. **180** (2009) 747 [arXiv:0803.2360 [hep-ph]].

[100] F. Iachello, L. M. Krauss and G. Maino, *Spin Dependent Scattering of Weakly Interacting Massive Particles in Heavy Nuclei,* Phys. Lett. B **254** (1991) 220.

[101] H. S. Lee *et al.* [KIMS Collaboration], *Limits on WIMP-nucleon cross section with CsI(Tl) crystal detectors,* Phys. Rev. Lett. **99** (2007) 091301 [arXiv:0704.0423 [astro-ph]].

[102] J. Engel and P. Vogel, *Spin dependent cross-sections of weakly interacting massive particles on nuclei,* Phys. Rev. D **40** (1989) 3132.

[103] E. Aprile *et al.* [XENON100 Collaboration], *Limits on spin-dependent WIMP-nucleon cross sections from 225 live days of XENON100 data,* Phys. Rev. Lett. **111** (2013) 2, 021301 [arXiv:1301.6620 [astro-ph.CO]].

[104] V. A. Bednyakov and F. Simkovic, *Nuclear spin structure in dark matter search: The Zero momentum transfer limit,* Phys. Part. Nucl. **36** (2005) 131 [Fiz. Elem. Chast. Atom. Yadra **36** (2005) 257] [hep-ph/0406218].

[105] R. Bernabei, P. Belli, V. Landoni, F. Montecchia, W. Di Nicolantonio, A. Incicchitti, D. Prosperi and C. Bacci *et al.*, *New limits on WIMP search with large-mass low-radioactivity NaI(Tl) set-up at Gran Sasso,* Phys. Lett. B **389** (1996) 757.

[106] J. I. Collar, *Quenching and channeling of nuclear recoils in NaI(Tl): Implications for dark-matter searches,* Phys. Rev. C **88** (2013) 3, 035806 [arXiv:1302.0796 [physics.ins-det]].

[107] S. K. Kim *et al.*, *Scintillator-based detectors for dark matter searches I,* 2010 New J. Phys. 12 075003.

[108] J. I. Collar, N. E. Fields, M. Hai, T. W. Hossbach, J. L. Orrell, C. T. Overman, G. Perumpilly and B. Scholz, *Coherent neutrino-nucleus scattering detection with a CsI[Na] scintillator at the SNS spallation source,* Nucl. Instrum. Meth. A **773** (2014) 56 [arXiv:1407.7524 [physics.ins-det]].

[109] P. J. Fox, G. D. Kribs and T. M. P. Tait, *Interpreting Dark Matter Direct Detection Independently of the Local Velocity and Density Distribution,* Phys. Rev. D **83** (2011) 034007 [arXiv:1011.1910 [hep-ph]].

[110] C. McCabe, *DAMA and CoGeNT without astrophysical uncertainties,* Phys. Rev. D **84** (2011) 043525 [arXiv:1107.0741 [hep-ph]].

[111] J. F. Cherry, M. T. Frandsen and I. M. Shoemaker, *Halo Independent Direct Detection of Momentum-Dependent Dark Matter,* JCAP **1410** (2014) 10, 022 [arXiv:1405.1420 [hep-ph]].

[112] J. Herrero-Garcia, *Halo-independent tests of dark matter annual modulation signals,* arXiv:1506.03503 [hep-ph].

[113] A. J. Anderson, P. J. Fox, Y. Kahn and M. McCullough, *Halo-Independent Direct Detection Analyses Without Mass Assumptions,* arXiv:1504.03333 [hep-ph].

[114] S. Scopel, J. H. Yoon and K. Yoon, *Generalized spin-dependent WIMP-nucleus interactions and the DAMA modulation effect,* arXiv:1505.01926 [astro-ph.CO].

[115] F. Ferrer, A. Ibarra and S. Wild, *A novel approach to derive halo-independent limits on dark matter properties,* arXiv:1506.03386 [hep-ph].